COMPUTATIONAL FLUID DYNAMICS SIMULATION OF GREEN WATER AROUND A TWO-DIMENSIONAL PLATFORM

A Thesis

by

YUCHENG ZHAO

Submitted to the Office of Graduate Studies of
Texas A&M University
in partial fulfillment of the requirements for the degree of

MASTER OF SCIENCE

December 2009

Major Subject: Ocean Engineering

COMPUTATIONAL FLUID DYNAMICS SIMULATION OF GREEN WATER AROUND A TWO-DIMENSIONAL PLATFORM

A Thesis

by

YUCHENG ZHAO

Submitted to the Office of Graduate Studies of
Texas A&M University
in partial fulfillment of the requirements for the degree of

MASTER OF SCIENCE

Approved by:

Chair of Committee,	Hamn-Ching Chen
Committee Members,	Scott A. Socolofsky
	Andrew T. Duggleby
Head of Department,	John Niedzwecki

December 2009

Major Subject: Ocean Engineering

ABSTRACT

Computational Fluid Dynamics Simulation of Green Water
Around a Two-Dimensional Platform. (December 2009)
Yucheng Zhao, B.S., Shanghai Jiao Tong University
Chair of Advisory Committee: Dr. Hamn-Ching Chen

An interface-preserving level set method is incorporated into the Reynolds-Averaged Navier-Stokes (RANS) numerical method to simulate the application of the green water phenomena around a platform and the breaking wave above the deck. In the present study, this method is used to evaluate the laminar in two dimension plane with fixed orthogonal grids.

In this method, it is assumed that the free surface is modeled as immiscible two-phase flow (air and water). A level set function can present the individual fluids, and the interface between two-phase is represented by the zero level set. In addition, the level set evolution equation is coupled with the conservation equations for mass and momentum, which will be solved in the transformed plane. For different purposes, there are several block domains in the application grid. Chimera domain decomposition technique is employed to handle such embedding, overlapping, or matching grids.

Several simple test cases were performed to demonstrate the feasibility of this method. The comparisons between the ENO scheme and the WENO scheme will be illustrated in the Zalesak's disk case and will further prove that the WENO scheme is

superior to the ENO scheme. The propagation of continuous wave case will validate some properties of wave and determine the importance of some parameters in code. Moreover, the method will be applied in simulation of green water around a two dimensional platform. By configuring different deck heights, some distinct phenomena can be represented. Lastly, it is crucial to observe the green water phenomena around the platform deck by applying the velocity-extrapolation routine.

To my parents

ACKNOWLEDGEMENTS

I would like to express my deepest gratitude to my advisor and chair, Dr. Hamn-Ching Chen, for his instruction, patience and support during my master study. Without his guidance, I would never step into CFD research field.

I would like to extend my gratefulness to my committee, Dr. Socolofsky, Dr. Duggleby, for their valuable time, suggestions and personal encouragement.

I would also like to thank my parents for their boundless love and support.

TABLE OF CONTENTS

Page

ABSTRACT iii

DEDICATION v

ACKNOWLEDGEMENTS vi

TABLE OF CONTENTS vii

LIST OF FIGURES ix

CHAPTER

I INTRODUCTION 1

1.1. Background 1
1.2. Literature Review 2
1.2.1. Surface Tracking 3
1.2.2. Surface Capturing 4

II GOVERNING EQUATIONS 9

2.1. Introduction 9
2.2. Level Set Method 9
2.3. RANS Equations 11
2.4. Velocity Extrapolation 15

III NUMERICAL METHOD 17

3.1. Introduction 17
3.2. Level Set Equation 17
3.2.1. Spatial Derivatives 18
3.2.2. Temporal Derivatives 21
3.3. RANS Equations 22
3.4. Assumptions and Justifications 23

IV RESULTS AND DISCUSSIONS 25

4.1. Zalesak's Problem 25

CHAPTER Page

4.2. Analysis of Several Parameters 28
4.2.1. Convergence Plot 33
4.2.2. Reynolds Number 34
4.2.3. The Order in Time 38
4.2.4. Global Iteration within Each Time Step 40
4.2.5. Time Increment 43
4.3. Analysis of Velocity-Extrapolation 45
4.4. Simulations of Green Water 48
4.4.1. Position I 51
4.4.2. Position II 56
4.4.3. Position III 61
4.4.4. Position IV 79
4.4.5. Position V 85

V CONCLUSIONS 94

REFERENCES 95

VITA 100

LIST OF FIGURES

FIGURE		Page
1.1	Green water incident at the side of Selkirk Settler	2
4.1	The grid for Zalesak's disk problem	27
4.2	Comparison about predicted surface of WENO and ENO method	28
4.3	Grid for continuous wave propagation	29
4.4	The convergence test	34
4.5	Reynolds Numbers at some gage positions	36
4.6	The comparison of different orders in time	38
4.7	The comparison of different global iteration within each time step	41
4.8	The comparison of different time increments	43
4.9	The comparison of results with and without velocity-extrapolation	46
4.10	The grid for simulation of green water around platform	50
4.11	Evolution of wave and dynamics contour in position I	52
4.12	Velocity field induced by the wave in position I	54
4.13	Evolution of wave and dynamics contour in position II	56
4.14	Velocity field induced by the wave in position II	59
4.15	Velocity field induced by the wave with and without velocity-extrapolation routine in position II	62
4.16	Evolution of wave and dynamics contour in position III	77
4.17	Evolution of wave and dynamics contour in position IV	80
4.18	Velocity field induced by the wave in position IV	81

FIGURE Page

4.19 Evolution of wave and dynamics contour in position V 86

4.20 Velocity field induced by the wave in position V..... 88

4.21 The series of dynamic pressure contour in the five positions at the same time step..... 91

4.22 The series of velocity field in the five positions at the same time step..... 92

CHAPTER I

INTRODUCTION

1.1. Background

Breaking free-surface water waves are a well known feature along many coasts (shallow water breaking) and in the offshore ocean (deep water breaking like in figure 1.1). And it is a critical issue to study breaking wave for the design and maintenance of coastal and ocean structures. In coastal areas, some steps should be put in practice to protect harbors, inlets and beach against wave attack. The effective step is to set break water, which can reduce the transmitted wave energy by reflecting the waves and dissipating the incident wave energy by breaking up the waves. In deep sea zone, the phenomena of water overtopping an offshore structure would be potential dangerous to platforms due to the high pressure and huge dynamic loads when the wave crests inundate the structure far above the waterline where not designed to withstand such wave impact.

The goal of present study is to introduce and apply an effective, accurate and robust numerical method to predict and simulate the free surface motion, even in the breaking wave situation. In this study, we consider issues on the immiscible fluids flow.

This thesis follows the style of *IEEE Transactions on Very Large Scale Integration (VLIS) Systems.*

Figure 1.1: Green water incident at the side of Selkirk Settler

(Photographed by Captain G.A. Ianiev)

1.2. Literature Review

For the green water and breaking wave, both of them are involved in tracking the air-water surface. There are numerous numerical methods proposed to predict the interface between two different fluids. In general, they could be classified into two different categories: the interface-tracking methods and the interface-capturing methods [1]. The interface-tracking methods follow the free surface motions and use boundary-fitted grids which are readjusted in each time step whenever the free surface moves. The

interface-capturing methods do not define a sharp free surface boundary. Instead, the computation is performed on a fixed grid, which is extended beyond the free surface. The geometry of the free surface is determined by a certain numerical variable, which is one of the numerical solutions. A variety of methods in this interface-capturing from this category, Marker and Cell (MAC) scheme, volume of fluid (VOF) scheme and level set method are summarized in the following section [2]-[4].

1.2.1. Surface Tracking

The surface tracking methods are expressed in Lagrangian view point which describes fluid motions as we follow a fluid particle along its trajectory. The surface tracking methods are characterized by an explicit representation of the surface. The Lagrangian method treats the free surface as a sharp interface whose motion is exactly followed. This is normally done by adapting boundary-fitted grids to the free surface and updating at each time step to track the new location of the free surface by using a height function to describe the vertical height of the surface location.

Chen, Liu, Chang and Huang used a Chimera Reynolds-Averaged Navier-Stokes method, which is a kind of Lagrangian approach, for time domain simulation of turbulent flows around a rectangular barge under large amplitude waves [5]. A flexible chimera grid system was developed to handle partial hull submergence with green water on the barge deck. The grid is adjusted every time step to follow the free surface motion. The same method was applied in Chen, Liu and Huang [6]. The surface tracking methods were also found in time-domain simulation of floating pier and multiple-vessel interactions, Chen and Huang [7].

1.2.2. Surface Capturing

The surface capturing methods use a different approach so-called Eulerian view point which describes the fluid motion at a fixed point. The computation is performed on a fixed grid, which extends beyond the free surface. Instead of being defined as a sharp boundary, the free surface is determined only after the solutions in the whole domain are finished. A number of schemes are available, and all of them use an implicit representation of the interface which is then captured as part of the solution. The most common schemes for surface capturing are the Marker-And-Cell method (MAC) which is proposed first by Harlow and Welch in 1965, the Volume-Of-Fluid method (VOF) which is originally developed by Hirt and Nichols in 1981 and the Level-Set method which is first studied by Osher and Sethian in 1988 [2]-[4]. For the last two schemes, the shape of the free surface is determined by computing the fraction of each near-interface cell that is partially filled. The details about these schemes are discussed in the following part.

In the MAC scheme, the free surface is captured by introducing massless particles at the free surface at the initial time and following their motion. These markers capture the detail of interface motions on scales much smaller than the grid spacing. The free surface geometry is then achieved by all the segments which are connections between adjacent marker.

MAC methods have been used extensively by many groups. Chan and Street introduced the Stanford University Modified MAC (SUMMAC) code which was shown to be a valid tool for analyzing incompressible flows with a free surface under transit

conditions [8]. Miyata group developed TUMMAC method (Tokyo University Modified Marker and Cell Method) for particular engineering problems related to water wave dynamics [9]. A modified MAC method (SIMAC; semi-implicit marker and cell) is proposed by Armenio which accurately treats unsteady high-Reynolds free surface problems [10]. The MAC methods are favored because they can treat complex free surface phenomena, including wave breaking. The higher degree of accuracy may be achieved by representing the interface through higher order interpolation polynomials. However, intensive computational effect is needed for these methods especially in three-dimensional problems with violent free surface motions. In addition to solving the equations governing the fluid flow, one has to follow the motion of a large number of particles. This leads to high computation time and cost.

The VOF method introduces a scalar, which is usually named the volume fraction or color function, which defines the filling degree of each cell. A cell with a volume fraction of 0 is empty, and a volume fraction value of 1 means a full cell. For those partially filled cells, F is the volume fraction of the fluid in the cell. Here, in addition to the conservation equations for mass and momentum, one has to introduce and solve an equation for the filled fraction of each control volume.

$$\frac{\partial f}{\partial t} + \vec{V} \cdot \nabla f = 0 \tag{1.1}$$

The VOF method has been known for several decades and has been developed and improved continuously by many research groups. Kothe and Rider and Scardovelli and Zaleski gave good reviews for the development of the VOF method in past decades [11], [12]. Now the VOF method has been proven as a popular, useful and robust tool for

interface tracking. There are many commercial codes which use this method to represent interfaces, SOLA-VOF, NASA-VOF3D (Torrey et al., 1987), RIPPLE (Kothe and Mjolsness, 1992) and FLOW3D (Hirt and Nichols, 1988) [13]-[16]. The widespread applications of VOF method is based on its essential advantages. The algorithm is based on a discrete representation of the conservation law. For this reason, the VOF method preserves mass in a natural way and it conserves mass well in calculations. Another advantage is the VOF method can be relatively simply extended from two-dimensional domain to three-dimensional domain. However, there is an obvious shortcoming for the VOF method. It must locate the interface in order to advect volume fraction. Low order reconstruction scheme may cause lots of errors in simulation. A lot of work had been done to develop different interface reconstruction procedures. The most typical schemes are known as simple line interface calculation (SLIC) and piecewise linear interface construction (PLIC). The SLIC is used widely in 80s' and early 90s' in the last century [13]. This is the first order approach, O(h), which forces the reconstruction to align with one of the mesh coordinates. PLIC is much more accurate to fit the interface through piecewise linear segments. The VOF scheme is widely used to simulate breaking wave, vigorous sloshing in tanks, and flows around ships and submerged bodies [17], [18]. Nevertheless, most of them have problems building an accurate and smooth free surface for complex three-dimensional free surface problems.

Another class of interface capturing methods is based on the level set function which is introduced by Osher and Sethian [4]. The level set function which is defined in the whole domain is typically initialized as the signed distance from the interface i.e. its

value at any point is the physical distance from the nearest point on the interface and its sign is positive on one side and negative on the other side. The interface is located at the one on which a level-set function while other values of this function have no significance. The level set function varies smoothly across the interface and is advected by the local velocity field using the advection equation.

$$\frac{\partial \phi}{\partial t} + \vec{V} \cdot \nabla \phi = 0 \tag{1.2}$$

As a solution of calculation, the interface can be captured at any time by locating the zero level set. In general, the computed ϕ may not remain the sign distance from the interface due to accumulated numerical errors and needs to be reinitialized for every time step. Sussman et al. proposed that this can be done by solving the following equation until the steady state is reached [19].

$$\frac{\partial \phi}{\partial \tau} = sign(\phi_0) \cdot (1 - |\nabla \phi|) \tag{1.3}$$

Sethian and Smereka (2003) provided an overview of the level set method for computing the solution to fluid-interface problems [20]. Osher and Fedkiw discussed not only recent variants and extensions of the level set method but also a user's guide to the level set dictionary and technology [21]. Compared to VOF methods the level set method seems to be an extremely promising method. Because it is not necessary to do the reconstruction procedure, the level set method handles the complex interface geometries in a simple way. And surface tension effects can be incorporated easily in this method. The biggest concern of the level set method is mass loss issue. In order to improve mass conservation, many research groups expanded the original level set

method. Sussman et al. first introduced a new constraint term in the redistancing scheme to improve accuracy and efficiency [22]. A coupled level set and VOF method is developed recently by Sussman and Puckett [23]. It seems to conserve mass as well as VOF methods. A similar method, which is known as the mass conserving level set method (MCLS), is presented by Van der Pijl et al, [24]. Takahira et al. improved the reinitialization procedure of the level set function by adding a multiplier of the order of one to the constraint term in order to recover the mass [25]. Enright et al. proposed a new numerical method to improve the mass conservation by using Lagrangian marker particles to rebuild the level set function in regions which are under-resolved [26]. The particle level set method has been proved to be an effective way in handling topological merging, breaking and even self-intersecting of interfaces problems. Predictable improvement in mass conservation is also obtained. The level set method is widely used in many areas other than incompressible fluid flows. Gibou et al. presented a level set approach for the modeling of dendritic solidification [27]. Pitsch and Lageneste employed the level set formulation to treat the instantaneous flams front as an interface [28]. Sethian and Adalsteinsson (1996) used the level set method for etching, deposition, lithography development [29]. More details of the level set method can found in Sethian [30].

CHAPTER II

GOVERNING EQUATIONS

2.1. Introduction

In this chapter, the Navier-Stokes equations are solved in conjunction with the level set equation for wave-current-body interaction problems involving violent free surface motions. Both of level set equation and RANS equation will be presented in physical plane and transformed plane.

2.2. Level Set Method

The level set method is a numerical technique to treat the evolution of interfaces and shapes. The advantage of level set method is that one can perform numerical computations involving curves and surfaces on an Eulerian approach (with a fixed Cartesian grid). Also, the level set method can make it easy to follow shapes with change topology, e.g. when a shape splits in two, develops holes, or the reverse of these operations.

Most of my study cases are water-air phase issues in two dimension plane. Thus, we can represent the particular interface by the zero level set function ϕ:

$$\Gamma = \{\vec{x} \mid \phi(\vec{x}, t) = 0\} \tag{2.1}$$

Furthermore, we can define the region of water and air over the domain:

$$\begin{cases} \phi(\vec{x},t) > 0, \ for \vec{x} \in water \\ \phi(\vec{x},t) = 0, \ for \vec{x} \in \Gamma \\ \phi(\vec{x},t) < 0, \ for \vec{x} \in air \end{cases} \tag{2.2}$$

The motion of the interface is determined by a velocity field $\vec{u}$ which is externally computed by RANS equation in present study. During the time evolution, the advection equation about ϕ is as follows:

$$\frac{\partial \phi}{\partial t} + \vec{V} \cdot \nabla \phi = 0 \tag{2.3}$$

Recall that ∇ is the gradient operator, so that $\vec{V} \cdot \nabla \phi = u\phi_x + v\phi_y + w\phi_z$.

In order to avoid the solution divergence due to jumping value of fluid properties between air and water, we set a transition zone nearby the zero level set. The transition zone is defined by $|\phi| < \varepsilon$, which is the half thickness of the interface. In the transition zone, some fluid properties should be smoothed by Heaviside function $H(\phi)$:

$$H(\phi) = \begin{cases} 0 & if \ \phi < -\varepsilon \\ \frac{1}{2}[1 + \frac{\phi}{\varepsilon} + \frac{1}{\pi}\sin(\frac{\pi\phi}{\varepsilon})] & if \ -\varepsilon \le \phi \le \varepsilon \\ 1 & if \ \phi > \varepsilon \end{cases} \tag{2.4}$$

Thus, some fluid properties including density and viscosity will be smoothed in this way:

$$\begin{cases} \rho(\phi) = \rho_a + (\rho_w - \rho_a) \cdot H(\phi) \\ \mu(\phi) = \mu_a + (\mu_w - \mu_a) \cdot H(\phi) \end{cases} \tag{2.5}$$

In addition, it is convenient to make ϕ equal to the signed distance to the interface after every time step. However, as the interface is moving, ϕ cannot continue to

satisfy the signed distance. To keep this good quality, we introduce a process called reinitialization to reconstruct ϕ. Reinitialization algorithms maintain the signed distance property by solving to steady state the equation:

$$\phi_\tau + \mathrm{sgn}(\phi_0)(|\nabla\phi| - 1) = 0 \tag{2.6}$$

where $\mathrm{sgn}(\phi_0)$ is a one-dimensional smeared out signum function approximated numerically as

$$\mathrm{sgn}(\phi_0) = \frac{\phi_0}{\sqrt{\phi_0^{\,2} + (\Delta x)^2}} \tag{2.7}$$

2.3. RANS Equations

The Navier-Stokes equations are rewritten in the level set formulation. Both the density and viscosity at air-water interfaces depend on the level set function being a distance function. The fluid properties are assumed to vary smoothly across a narrow transition zone around the free surface. This enables us to obtain accurate and stable numerical results for violent free surface motions encountered in the simulation of green water on offshore platforms.

It is assumed that both water and air are governed by the incompressible Navier-Stokes equations:

$$\begin{cases} \rho_w\left(\dfrac{\partial \overrightarrow{V'}}{\partial t'} + \overrightarrow{V'}\cdot\nabla\overrightarrow{V'}\right) = \rho_w \vec{g} + \mu_w \nabla^2 \overrightarrow{V'} - \nabla p' \\ \rho_a\left(\dfrac{\partial \overrightarrow{V'}}{\partial t'} + \overrightarrow{V'}\cdot\nabla\overrightarrow{V'}\right) = \rho_a \vec{g} + \mu_a \nabla^2 \overrightarrow{V'} - \nabla p' \end{cases} \tag{2.8}$$

The above equations are normalized using the following three dimensionless variables:

$$\vec{V} = \frac{\vec{V'}}{U_0}, t = \frac{t'}{t_0} = \frac{U_0}{L} t', p = \frac{p'}{\rho_w {U_0}^2}$$

In addition, the non-dimensional density $\rho(\phi)$ and non-dimensional viscosity $\nu(\phi) = \mu(\phi) / \rho(\phi)$ can be represented as below:

$$\begin{cases} \rho(\phi) = \dfrac{\rho}{\rho_w} + (1 - \dfrac{\rho}{\rho_w}) \cdot H(\phi) \\ \mu(\phi) = \dfrac{\mu}{\mu_w} + (1 - \dfrac{\mu}{\mu_w}) \cdot H(\phi) \end{cases} \tag{2.9}$$

After dividing by $\rho_w {U_0}^2 / L$ and combine those two equations together, the general Navier-Stokes equations will be:

$$\frac{\partial \vec{V}}{\partial t} + \vec{V} \cdot \nabla \vec{V} = -\frac{\delta_{i,3}}{Fr^2} + \frac{\nu(\phi)}{\mathrm{Re}} \nabla^2 \vec{V} - \frac{1}{\rho(\phi)} \nabla p$$

where Froude number $Fr^2 = \dfrac{{U_0}^2}{gL}$ and Reynolds number $\mathrm{Re} = \dfrac{\rho_w U_0 L}{\mu_w}$.

In the transform plane, which is curvilinear coordinate, the continuity and momentum equations will be:

$$\begin{cases} \displaystyle\sum_{i=1}^{3} \frac{\partial U_i}{\partial x^i} = 0 \\ \dfrac{\partial U_i}{\partial t} + \displaystyle\sum_{j=1}^{3} (U_j \frac{\partial U_i}{\partial x^j} + \frac{\partial \overline{u_i u_j}}{\partial x^j}) + \frac{1}{\rho(\phi)} \frac{\partial p}{\partial x^i} - \frac{\nu(\phi)}{\mathrm{Re}} \nabla^2 U_i + \frac{\delta_{i,3}}{Fr^2} = 0 \end{cases} \tag{2.10}$$

with $\nabla^2 = \displaystyle\sum_{i=1}^{3} \frac{\partial^2}{\partial x^j \partial x^j}$.

The Reynolds stress $\overline{u_i u_j}$ are related to the corresponding mean rate of strain through an isotropic eddy viscosity ν_t:

$$-\overline{u_i u_j} = \nu_t(\frac{\partial U_i}{\partial x^j} + \frac{\partial U_j}{\partial x^i}) - \frac{2}{3}\delta_{ij}k \tag{2.11}$$

where $k = (\overline{uu} + \overline{vv} + \overline{ww})/2$ is he turbulent kinetic energy and δ_{ij} is the Kronecker delta. The substitution of Reynolds stress into the momentum equations yields:

$$\frac{\partial U_i}{\partial t} + \sum_{j=1}^{3}[(U_i - \frac{\partial \nu_t}{\partial x^j})\frac{\partial U_i}{\partial x^j} - \frac{\partial \nu_t}{\partial x^j}\frac{\partial U_j}{\partial x^i}] = -\frac{\delta_{i,3}}{Fr^2} + (\frac{\nu(\phi)}{\mathrm{Re}} + \nu_t)\nabla^2 U_i - (\frac{1}{\rho(\phi)}\frac{\partial p}{\partial x^i} + \frac{\partial(\frac{2}{3}k)}{\partial x^i}) \tag{2.12}$$

Let $\varphi = U_i$ and rearrange the momentum equations as follows:

$$\nabla^2\varphi = R_\varphi \cdot [\sum_{j=1}^{3}(U_j - \frac{\partial \nu_t}{\partial x^j})\frac{\partial \varphi}{\partial x^j} + \frac{\partial \varphi}{\partial t}] + s_\varphi \tag{2.13}$$

where the effective viscosity is $R_\varphi = (\frac{\nu(\phi)}{\mathrm{Re}} + \nu_t)^{-1}$ and the source terms are given by:

$$s_\varphi = R_\varphi[\frac{1}{\rho(\phi)}\frac{\partial p}{\partial x^i} + \frac{\partial(\frac{2}{3}k)}{\partial x^i} - \sum_{i=1}^{3}\frac{\partial \nu_t}{\partial x^j}\frac{\partial U_j}{\partial x^i} + \frac{\delta_{i,3}}{Fr^2}] \tag{2.14}$$

In curvilinear coordinate system, those terms can be rewritten in the transformed plane as follows:

$$\begin{cases} \nabla^2\varphi = \sum_i \sum_j g^{ij} \dfrac{\partial^2 \varphi}{\partial \xi^i \partial \xi^j} + \sum_j f^j \dfrac{\partial \varphi}{\partial \xi^j} \\ \dfrac{\partial \varphi}{\partial t} = \dfrac{\partial \varphi}{\partial \tau} - \dfrac{1}{J} \sum_i \sum_j b_i{}^j \dfrac{\partial x^i}{\partial \tau} \dfrac{\partial \varphi}{\partial \xi^j} \\ \sum_j U_j \dfrac{\partial \varphi}{\partial x^j} = \sum_i U_i \left(\dfrac{1}{J} \sum_j b_i{}^j \dfrac{\partial \varphi}{\partial \xi_j}\right) \\ -\dfrac{\partial \nu_t}{\partial x^j} \dfrac{\partial \varphi}{\partial x^j} = -\sum_n \left[\dfrac{1}{J} \sum_m b_n{}^m \dfrac{\partial \nu_t}{\partial \xi^m} \cdot \dfrac{1}{J} \sum_j b_n{}^j \dfrac{\partial \varphi}{\partial \xi^j}\right] \end{cases} \tag{2.15}$$

Here, $b_i{}^j, g^{ij}, f^j$ and the Jacobian J are geometric coefficients in curvilinear coordinate system whose values can be readily evaluated in the transformed plane. Plug these terms into equation (2.13), we can get:

$$\sum_i \sum_j g^{ij} \frac{\partial^2 \varphi}{\partial \xi^i \partial \xi^j} - \sum_j 2a_\varphi{}^j \frac{\partial \varphi}{\partial \xi^j} = R_\varphi \frac{\partial \varphi}{\partial \tau} + s_\varphi \tag{2.16}$$

where, $2a_\varphi{}^j = \dfrac{R_\varphi}{J} \sum_n b_n{}^j [U_n - \dfrac{\partial x_i}{\partial \tau} - \sum_m \dfrac{1}{J} b_n{}^m \dfrac{\partial \nu_t}{\partial \xi^m}] - f^i$

note that:

$$\sum_i \sum_j g^{ij} \frac{\partial^2 \varphi}{\partial \xi^i \partial \xi^j} = g^{11} \frac{\partial^2 \varphi}{\partial \xi^1 \partial \xi^1} + g^{22} \frac{\partial^2 \varphi}{\partial \xi^2 \partial \xi^2} + g^{33} \frac{\partial^2 \varphi}{\partial \xi^3 \partial \xi^3} + 2(g^{12} \frac{\partial^2 \varphi}{\partial \xi^1 \partial \xi^2} + g^{23} \frac{\partial^2 \varphi}{\partial \xi^2 \partial \xi^3} + g^{31} \frac{\partial^2 \varphi}{\partial \xi^3 \partial \xi^1})$$

Plugging it into equation (2.16), we will get:

$$\sum_j (g^{jj} \frac{\partial^2 \varphi}{\partial \xi^j \partial \xi^j} - 2a_\varphi{}^j \frac{\partial \varphi}{\partial \xi^j}) = R_\varphi \frac{\partial \varphi}{\partial \tau} + S_\varphi \tag{2.17}$$

$$S_\varphi = s_\varphi - 2(g^{12} \frac{\partial^2 \varphi}{\partial \xi^1 \partial \xi^2} + g^{23} \frac{\partial^2 \varphi}{\partial \xi^2 \partial \xi^3} + g^{31} \frac{\partial^2 \varphi}{\partial \xi^3 \partial \xi^1}) \tag{2.18}$$

The momentum equation and the continuity equation are the Reynolds-Averaged Navier-Stokes (RANS) equation for unsteady, three-dimensional turbulent flows.

2.4. Velocity Extrapolation

The velocity field off the interface will help us to compute the solution of level set equation. The function of velocity extrapolation is to extrapolate the velocity field from water to air region. In fact, the velocity of air is greater than that in water area. When it comes to tracking the over-turning wave or breaking wave, it will be hard to present those delicate shapes for the reason that the numerical solution will diverge if the neighboring values have huge difference. It is simple and efficient way to simulation over-turning wave by resorting to extrapolation.

The velocity extrapolation equation is simply like reinitialization equation:

$$\frac{\partial \overrightarrow{U_{ext}}}{\partial \tau} + \vec{N} \cdot \nabla \overrightarrow{U_{ext}} = 0 \tag{2.19}$$

$$\vec{N} = \frac{\nabla \phi}{|\nabla \phi|} \tag{2.20}$$

where $\nabla \phi = \phi_{,i} \vec{a}^{i} = \frac{\partial \phi}{\partial \xi} \vec{a}^{1} + \frac{\partial \phi}{\partial \eta} \vec{a}^{2} + \frac{\partial \phi}{\partial \varsigma} \vec{a}^{3} = \phi_{\xi} \vec{a}^{1} + \phi_{\eta} \vec{a}^{2} + \phi_{\varsigma} \vec{a}^{3}$

$$|\nabla \phi| = \sqrt{\nabla \phi \cdot \nabla \phi} = \sqrt{\phi_{,i} \phi_{,j} \vec{a}^{i} \vec{a}^{j}} = \sqrt{g^{ij} \phi_{,i} \phi_{,j}}$$

Thus,

$$\vec{N} = \frac{\phi_{\xi}}{|\phi|} \vec{a}^{1} + \frac{\phi_{\eta}}{|\phi|} \vec{a}^{2} + \frac{\phi_{\zeta}}{|\phi|} \vec{a}^{3} = N_i \vec{a}^{i}, N_i = \frac{\phi_{,i}}{|\nabla \phi|} \tag{2.21}$$

$$\frac{\partial \overrightarrow{U_{ext}}}{\partial \tau} + \vec{N} \cdot \nabla \overrightarrow{U_{ext}} = \frac{\partial \overrightarrow{U_{ext}}}{\partial \tau} + \frac{g^{ij}\phi_{,i}U_{ext,j}}{g^{mn}\phi_{,m}\phi_{,n}} = 0 \tag{2.22}$$

This extrapolation is limited to a narrow band on the air side of the interface.

CHAPTER III

NUMERICAL METHOD

3.1. Introduction

This chapter presents the finite difference scheme for both level set equation and RANS equations. For RANS equations, we apply the finite analytic solution. For level set equation, the fifth order weighted essentially non-oscillatory (WENO) scheme and total variation diminishing (TVD) Runge-Kutta scheme are introduced to discretize the level set equation and re-distance equation.

3.2. Level Set Equation

We further introduce the contravariant velocity components [31],

$$U^i = JV^i = \sum_{j=1}^{3} b^i{}_j U_j \tag{3. 1}$$

The level set evolution equation is written in the transformed coordinates (ξ^i, τ)

$$\frac{\partial \phi}{\partial \tau} + \sum_{i=1}^{3} \frac{\partial (U^i \phi)}{\partial \xi^i} = 0 \tag{3. 2}$$

As we mention that the velocity field is externally computed before computing the level set equation, the level set equation can be simplified as follows:

$$\frac{\partial \phi}{\partial \tau} + \sum_{i=1}^{3} U^i \cdot \frac{\partial \phi}{\partial \xi^i} = 0 \tag{3. 3}$$

where U^i are velocities at every grid points of transformed plane.

However, the plane transformation only changes the scalar at every grid points not vectors. That means U^i also denotes the velocities at every grid points of physical plane.

3.2.1. Spatial Derivatives

We begin to address the evaluation of the $u^n\phi^n{}_x$ term first. The techniques used to approximate this term can then be applied independently to the other two spatial terms.

Considering the properties of upwind differencing, we address this spatial term in this way [32]:

$$\text{If } u_i < 0, \text{ we define } (\phi_x)_i = D^-\phi = \frac{\phi_i - \phi_{i-1}}{\Delta x} \tag{3. 4}$$

$$\text{If } u_i > 0, \text{ we define } (\phi_x)_i = D^+\phi = \frac{\phi_{i+1} - \phi_i}{\Delta x} \tag{3. 5}$$

$$\text{If } u_i = 0, \text{ this term vanishes} \tag{3. 6}$$

where $(\phi_x)_i$ denoted the spatial derivative of ϕ at the point x_i.

This is a first-order accurate discretization of the spatial operator. This scheme can be improved upon by using a more accurate approximation for $\phi_x^- or \phi_x^+$. The velocity u is still used to decide whether ϕ_x^- or ϕ_x^+ is used, but the approximations for $\phi_x^- or \phi_x^+$ can be improved significantly. We use the smoothest possible polynomial interpolation to find ϕ and then differentiate to get ϕ_x. Here we extend the upwind scheme to ENO scheme:

The zero divided difference of ϕ are defined at the grid nodes and defined by

$$D^0{}_i\phi = \phi_i \tag{3. 7}$$

The first divided difference of ϕ are defined midway between grid nodes as

$$D^1{}_{i+1/2}\phi = \frac{D^0{}_{i+1}\phi - D^0{}_i\phi}{\Delta x} \tag{3. 8}$$

The second divided difference of ϕ are defined at the grid nodes and defined by

$$D^2{}_i\phi = \frac{D^1{}_{i+1/2}\phi - D^1{}_{i-1/2}\phi}{2\Delta x} \tag{3. 9}$$

Lastly, the third divided difference of ϕ are defined midway between grid nodes as

$$D^3{}_{i+1/2}\phi = \frac{D^2{}_{i+1}\phi - D^2{}_i\phi}{3\Delta x} \tag{3. 10}$$

Then, we write $\phi_x = \frac{dQ}{dx} = \frac{dQ_1}{dx} + \frac{dQ_2}{dx} + \frac{dQ_3}{dx}$. The algorithm is as follows,

1. To find $\phi_x{}^-$, start with k=i-1, and to find $\phi_x{}^+$, start with k=i.

2. Define $\frac{dQ_1}{dx}(x_i) = D^1{}_{k+1/2}\phi$.

3. a)If $|D^2{}_k\phi| < |D^2{}_{k+1}\phi|$, set $c = D^2{}_k\phi$ and $k^* = k-1$;

   b) Else set $c = D^2{}_{k+1}\phi$ and $k^* = k$;

   c) Define $\frac{dQ_2}{dx}(x_i) = c(2(i-k)-1)\Delta x$.

4. a)If $|D^3{}_{k^*+1/2}\phi| < |D^3{}_{k^*+3/2}\phi|$, set $c^* = D^3{}_{k^*+1/2}\phi$;

   b) Else set $c^* = D^3{}_{k^*+3/2}\phi$;

c) Define $\frac{dQ_3}{dx}(x_i) = c^*(3(i-k^*)^2 - 6(i-k^*) + 2)\Delta x^2$.

It is the same thing with the other terms.

Furthermore, a weighted ENO (WENO) method takes a convex combination of the three ENO approximations [33]-[35]. Since it reduces the errors by more than an order of magnitude over the third-order accurate ENO scheme, WENO scheme turns out to be very useful for solving level set equation.

Firstly, we define three possible ENO approximates to $(\phi_x^-)_i$. Defining ,

$$v_1 = D^-\phi_{i-2}, v_2 = D^-\phi_{i-1}, v_3 = D^-\phi_i, v_4 = D^-\phi_{i+1}, v_5 = D^-\phi_{i+2}.$$

We have these three approximations below,

$$\begin{aligned} \phi^1{}_x &= \frac{v_1}{3} - \frac{7v_2}{6} + \frac{11v_3}{6} \\ \phi^2{}_x &= -\frac{v_2}{6} + \frac{5v_3}{6} + \frac{v_4}{3} \\ \phi^3{}_x &= \frac{v_3}{3} + \frac{5v_4}{6} - \frac{v_5}{6} \end{aligned} \tag{3. 11}$$

The WENO approximation is a convex combination of the approximations given by,

$$\phi_x = \omega_1\phi_x{}^1 + \omega_2\phi_x{}^2 + \omega_3\phi_x{}^3 \tag{3. 12}$$

where $0 \le w_k \le 1$, $\omega_1 + \omega_3 + \omega_3 = 1$.

In smooth region, these three weight coefficients are equally significant. To the contrary, in non-smooth region, we have to determinate the weight coefficient values. In order to define the weights, we estimate the smoothness of the stencils as,

$$
\begin{aligned}
S_1 &= \frac{13}{12}(v_1 - 2v_2 + v_3)^2 + \frac{1}{4}(v_1 - 4v_2 + 3v_3)^2 \\
S_2 &= \frac{13}{12}(v_2 - 2v_3 + v_4)^2 + \frac{1}{4}(v_2 - 4v_4)^2 \\
S_3 &= \frac{13}{12}(v_3 - 2v_4 + v_5)^2 + \frac{1}{4}(3v_3 - 4v_4 + v_5)^2
\end{aligned}
\tag{3. 13}
$$

Using these smoothness estimates, we define

$$
\begin{aligned}
\alpha_1 &= \frac{0.1}{(S_1 + \varepsilon)^2} \\
\alpha_2 &= \frac{0.6}{(S_2 + \varepsilon)^2} \\
\alpha_3 &= \frac{0.3}{(S_3 + \varepsilon)^2}
\end{aligned}
\tag{3. 14}
$$

with $\varepsilon = 10^{-6}$. Finally, the weights would be as follows,

$$
\begin{aligned}
\omega_1 &= \frac{\alpha_1}{\alpha_1 + \alpha_2 + \alpha_3} \\
\omega_2 &= \frac{\alpha_2}{\alpha_1 + \alpha_2 + \alpha_3} \\
\omega_3 &= \frac{\alpha_3}{\alpha_1 + \alpha_2 + \alpha_3}
\end{aligned}
\tag{3. 15}
$$

Thus, we can compute the (ϕ_x^-) throughout the domain.

The function (ϕ_x^+) is constructed with a subset of $\{\phi_{i-2}, \phi_{i-1}, \phi_i, \phi_{i+1}, \phi_{i+2}, \phi_{i+3}\}$.

Defining $v_1 = D^+\phi_{i+2}, v_2 = D^+\phi_{i+1}, v_3 = D^+\phi_i, v_4 = D^+\phi_{i-1}, v_5 = D^+\phi_{i-2}$

3.2.2. Temporal Derivatives

There are times when a higher-order temporal discretization is necessary in order to obtain accurate numerical solutions. In present study, the equation is advanced using

3rd order TVD Runge-Kutta scheme which is total variation stable,

$$\begin{cases} \phi^{(1)} = \phi^{(n)} - \Delta\tau \cdot R(\phi^{(n)}) \\ \phi^{(2)} = \frac{3}{4}\phi^{(n)} + \frac{1}{4}\phi^{(1)} - \frac{\Delta\tau}{4} \cdot R(\phi^{(1)}) \\ \phi^{(3)} = \frac{1}{3}\phi^{(n)} + \frac{2}{3}\phi^{(2)} - \frac{2\Delta\tau}{3} \cdot R(\phi^{(2)}) \end{cases} \quad (3.\ 16)$$

where $R(\phi) = U^i \cdot \frac{\partial \phi}{\partial \xi^i}$ and it can be addressed by the previous spatial discretization.

3.3. RANS Equations

The momentum equations are solved by the 12-point finite analytic scheme of Chen ,et al. [31]. In the finite analytic approach, equation (2.17) is locally linearized in each rectangular numerical element. After that, a 12-point finite analytic formula for unsteady, three-dimensional, elliptic equations can be obtained in the form:

$$\varphi_P = \frac{1}{1 + C_P(C_U + C_D + \frac{R}{\Delta\tau})} \cdot [\sum_1^8 C_{nb}\varphi_{nb} + C_P(C_U\varphi_U + C_D\varphi_D + \frac{R}{\Delta\tau}\varphi_P{}^{n-1}) - C_P(S_\varphi)_P] \quad (3.\ 17)$$

The subscript ‘U’ and ‘D’ represent points in the stencil, upstream and downstream of ‘P’ and the subscript ‘nb’ denotes neighboring nodes. The finite-analytic coefficients (C_P, C_U, C_D, C_{nb}) can be found in Chen et al. [31].

The velocity U_i in equations was solved by the PISO/SIMPLER algorithm. The velocities and pressure are defined at the grid nodes while the contravariant pseudo velocities are at staggered locations. The velocities U_i were decomposed into a pseudo

velocities field U_i plus the pressure-gradient terms contained in the source function and can be found as follows:

$$U_{i,P} = U_i - \frac{\frac{1}{J}C_P R}{1 + C_P(C_U + C_D + \frac{R}{\Delta\tau})} \frac{1}{\rho(\phi)} \sum_j b_i^{\,j} \frac{\partial p}{\partial \xi^j} \tag{3. 18}$$

where the pseudo-velocities are defined by:

$$U_i = \frac{1}{1 + C_P(C_U + C_D + \frac{R}{\Delta\tau})} \cdot [\sum_1^8 C_{nb} U_{i,nb} + C_P(C_U U_{i,u} + C_D U_{i,D} + \frac{R}{\Delta\tau} U_{i,p}{}^{n-1}) - C_P R(S_{U_i} + \frac{1}{Fr^2})]$$

A resulting equation for pressure is derived by requiring the contravariant velocity filed U_i to satisfy the equation of continuity.

$$(E_d^{\,11} + E_u^{\,11} + E_n^{\,22} + E_s^{\,22} + E_e^{\,33} + E_w^{\,33}) p_P = E_d^{\,11} p_D + E_u^{\,11} p_U + E_n^{\,22} p_{NC} + E_s^{\,22} p_{SC} + E_e^{\,33} p_{EC} + E_w^{\,33} p_{WC} - D \tag{3. 19}$$

where,

$$\tilde{D} = \tilde{D}_d^{\,1} - \tilde{D}_u^{\,1} + D_n^{\,2} - D_s^{\,2} + D_e^{\,3} - D_w^{\,3} = \frac{1}{2}(D_D^{\,1} - D_U^{\,1} + D_{NC}^{\,2} - D_S^{\,2} + D_{EC}^{\,3} - D_{WC}^{\,3})$$

3.4. Assumptions and Justifications

In my study, I solve the level set equation incorporated RANS equations to handle the laminar problem in two dimension plane such as green water around the two-dimensional platform. Thus, I did not introduce the turbulence model considering that the effect of viscosity in the fluid is only apparent near restraining boundaries such as a wall or bottom boundary. Furthermore, if present, they can be assumed to be relevant only in a thin layer near the boundary (the boundary layer). We can therefore more or

less assume that the fluid is without turbulence. And it will greatly save lots of CPU time because we can use relative coarse grid near boundary if we do not need to take care of turbulence.

For velocity extrapolation routine, we can only apply it in the domain where we need to construct the breaking wave, because this kind of routine can keep the mass conservation well and then simulate the breaking wave phenomena. For the normal wave, it is not necessary to apply this routine because the normal wave shape is not complicated and it can keep mass conservation well without the velocity extrapolation. In addition, we do not need to worry about the change of air velocity will affect the water filed. In fact, the density of air is so less than that of water, thus the adjustment of air velocity will not modify the water motion.

CHAPTER IV

RESULTS AND DISCUSSIONS

4.1. Zalesak's Problem

The Zalesak's problem of a rotating slotted disk is a benchmark case for testing an advection scheme. The details are as following: the slotted disk interface has a radius of 15 and a slot width of 6. It is initially located at (50, 75) in the domain of size (100, 100). The gird is uniform grid with each grid size 1*1. The grid dimension is 3*101*101 in x, y, z axis respectively. The details about grid can be observed in figure 4.1.

The angular velocity is set to 0.01 so that the disk returns to its original position at every 200π time units. If the particles in the domain move around the center of domain with angular velocity $\omega = 0.01$, we can obtain the velocity filed all over the domain, which is $V = (u, v) = (-\omega(y - 50), \omega(x - 50))$.

For the prescribed velocity filed, it is relatively easy to solve the level set equation. In present case, we introduce the fifth order WENO scheme and the third order ENO scheme respectively and compare the results each other. After the disk rotates, the interface will become distorted more or less. Thus, it is the excellent method which can maintain the final disk interface closest to the initial dish surface after one or several periods.

Figure 4.2 shows that the comparisons of initial geometry of disk and final results with the third-order ENO scheme and the fifth-order WENO scheme respectively. By the evolution of one circle rotation anticlockwise, we can observe the process of interface shift. Figure 4.2 illustrates the rotation process at $t = 0, 40, 79, 119, 158$. All in all, it is hard to keep the interface like initial shape precisely and the distortion is more serious when the rotation time is longer. Furthermore, we can notice that the fifth order WENO scheme is better than the third-order ENO scheme for the reason that the result with WENO scheme is closer to the original shape at every time step showed in figure 4.2. This test proves that it is necessary to introduce a better algorithm to address the level set equation for high solution. Thus, in following cases, we adopt the fifth order WENO scheme instead of the third order ENO scheme.

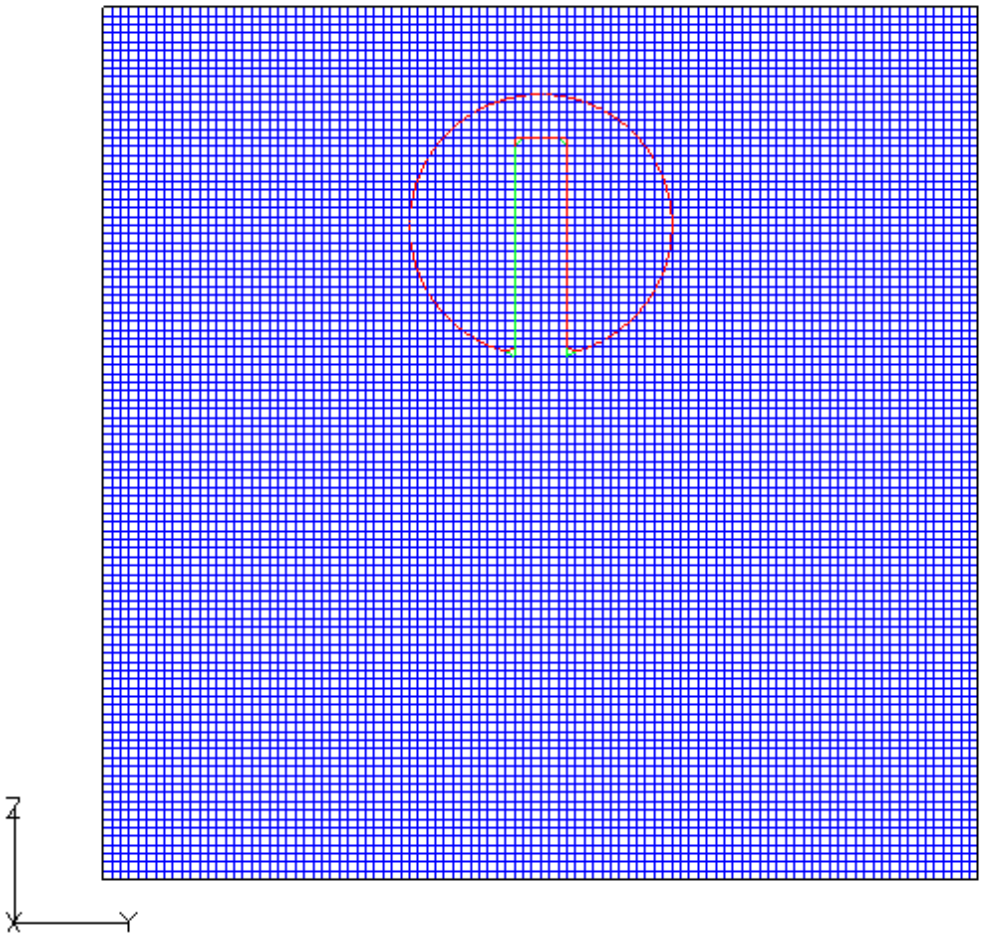

Figure 4.1: The grid for Zalesak's disk problem

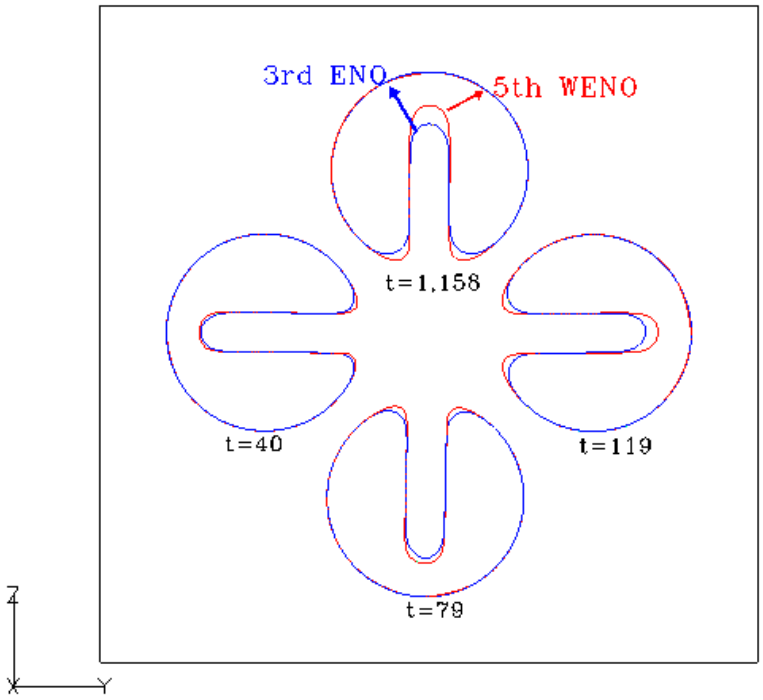

Figure 4.2: Comparison about predicted surface of WENO and ENO method

Moreover, we can test the similar case in the clockwise direction velocity field with goal of testing the scheme's recovery ability.

4.2. Analysis of Several Parameters

The propagation of continuous wave is the basic case to generate the regular wave along the domain within some periods. By observing how much the decay is, we

can modify some parameter values to choose the best result to fit for our simulations and determine the importance of these parameters [36].

First of all, the tank consists of three blocks which can be shown in figure 4.3. The first domain is to generate the linear wave; the second one is to compute the wave propagation using level set RANS method. The last one is to damp the wave amplitude and make sure that the wave reflection effect is as small as possible. The grid dimension is: tank 1 is 3*101*121 in x, y, z axis respectively; tank 2 is 3*501*121 in x, y, z axis respectively; tank 3 is 3*41*121 in x, y, z axis respectively. The interface is approximately distributed along the middle of domain which is the most important region over the domain. Thus, in the whole domain, the horizontal size is uniform with the spacing 0.04 except the tank 3, and the vertical size will become finer gradually in the middle of domain with the finest spacing less than 0.01. In the tank 3, the horizontal spacing becomes coarser with the distance further away from tank 2.

(a) Overview of the grid

Figure 4.3: Grid for continuous wave propagation

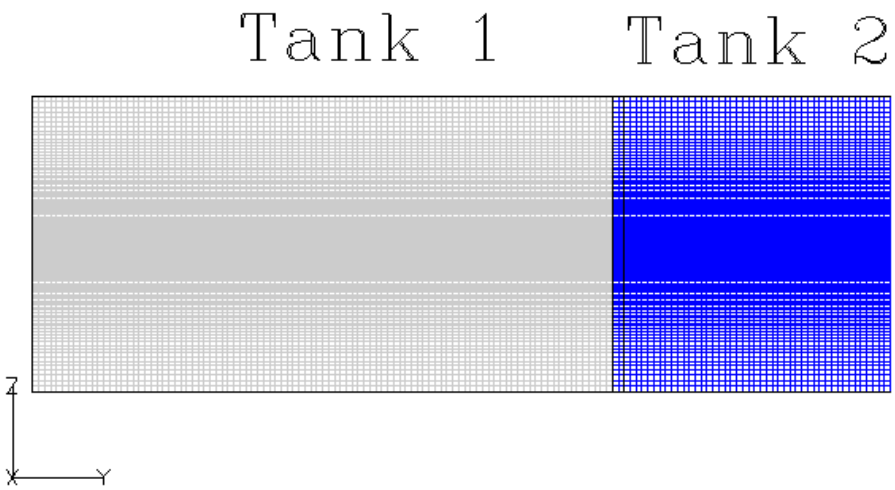

(b) Overlapping part between tank 1 and tank 2

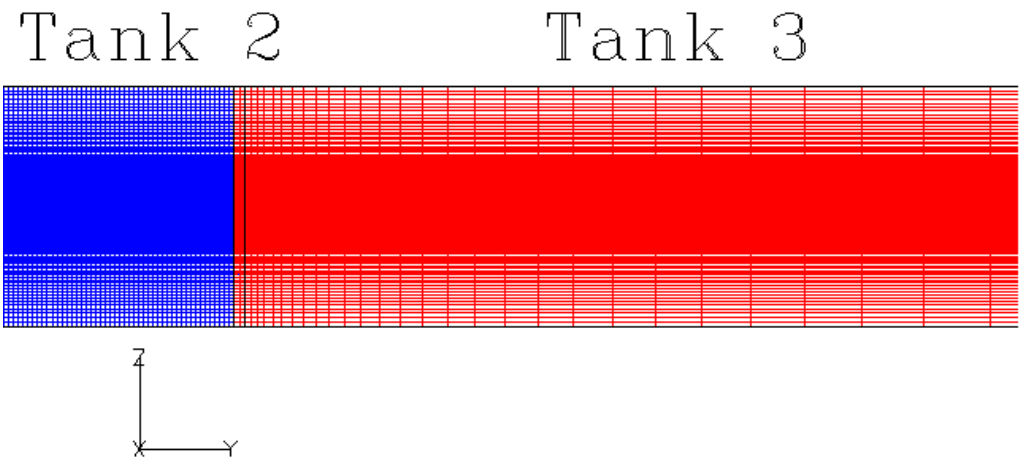

(c) Overlapping part between tank 2 and tank 3

Figure 4.3: (Continued)

In the tank 1, we can prescribe the wave properties as the linear wave theory and assume the deep water condition:

Wave profile $\eta = A\cos(kx - \omega t)$

$$\text{Horizontal velocity } v = \frac{Ak}{\omega} \cdot \frac{\cosh k(h+z)}{\cosh kh} \cdot \cos(kx - \omega t)$$

$$\text{Vertical velocity } w = \frac{Ak}{\omega} \cdot \frac{\cosh k(h+z)}{\cosh kh} \cdot \sin(kx - \omega t)$$

$$\text{Pressure } p = (-z + A \cdot \frac{\cosh k(h+z)}{\cosh kh} \cdot \cos(kx - \omega t)) \cdot \rho$$

$$\text{Linear dispersion relation } \sigma^2 = k$$

Note that all of the wave properties are dimensionless scales.

The wave properties including wavelength, wave height and so on are based on dimensionless scales:

The characteristic length is defined as the water depth $D / L = 1$

where, D means water depth and L means characteristic length.

The characteristic time is defined as $T = \sqrt{\frac{L}{g}}$.

The characteristic velocity is $U = \sqrt{gL}$.

By choosing dimensionless scales for wave properties, we can incorporate these parameters into RANS equations because the variables in RANS equations are all dimensionless variables.

In present case, we adopt the wave properties as following:

Wave height is $A = 0.15$.

Wavelength is $\lambda = 3$.

Water depth is $h = 1$

To make sure the wave is linear wave, the steepness should be less than 0.01 which means $\tan\theta = \frac{2A}{L} \le 0.01$. The above wave properties satisfy this condition. Furthermore, linear wave theory defines the wave properties under the mean water level. Thus, these equations cannot be used in the zone above the mean water level. We need to introduce Wheeler's Stretching Technique:

$$\text{Horizontal velocity } v = \frac{Ak}{\omega} \cdot \frac{\cosh\{k(h+z)/(1+\eta/h)\}}{\cosh kh} \cdot \cos(kx - \omega t)$$

$$\text{Vertical velocity } w = \frac{Ak}{\omega} \cdot \frac{\cosh\{k(h+z)/(1+\eta/h)\}}{\cosh kh} \cdot \sin(kx - \omega t)$$

where, $\eta = A\cos(kx - \omega t)$

Wheeler's Stretching Technique is to stretch the velocity profile from the sea bottom to free surface and make the profile precise.

When the wavelength is defined as 3, we can simply calculate that the second tank is about more than six wavelengths. Through recording the wave amplitude along the second tank, it is straightforward to know how much the decay is and how good the result is.

In the tank 3, the artificial damping function is applied to reduce the wave effect and thus make sure decrease the reflection wave effect. The damping function is defined as:

$$damp = \frac{1}{2}(1 - \cos\pi\theta)$$

$$\theta = \frac{s_x - s_1}{s_2 - s_1}$$

where s denotes the horizontal distance from the beginning of tank 2 to certain point in tank 2. s_1 is the distance to start of damping beach; s_2 is the distance to end of damping beach; s_x is the distance to any point in the damping beach. In present case, the total length of damping beach is defined as double wavelengths. Thus,

$$when\theta = 0, damp = 0;\ when\theta = \pi, damp = 1.$$

Lastly, the wave properties are damped by following equations:

$$u'(x, y, t) = (1 - damp) \cdot u(x, y, t)$$

$$v'(x, y, t) = (1 - damp) \cdot v(x, y, t)$$

$$pr_d'(x, y, t) = (1 - damp) \cdot pr_d(x, y, t)$$

Alternatively, another damping method is applied to make sure the damping effect. This way is to generate the gird of tank 2 and make sure that the further away from the beginning of tank the grid is, the coarser the grid is. If the grid size is coarse, the solution error will be amplified and the solution will decrease. In numerical sense, if the truncation error is $O(\Delta x^n)$, the truncation error is larger with the grid size is larger. Thus, the solution will be divergent into less value.

4.2.1 Convergence Plot

For the second domain, I will apply three different grids to take the convergence test. The dimensions of these three grids are as following:

The coarse grid: 3*101*121 with the horizontal spacing 0.08;

The intermediate grid: 3*201*121 with the horizontal spacing 0.04;

The fine grid: 3*401*121 with the horizontal spacing 0.02.

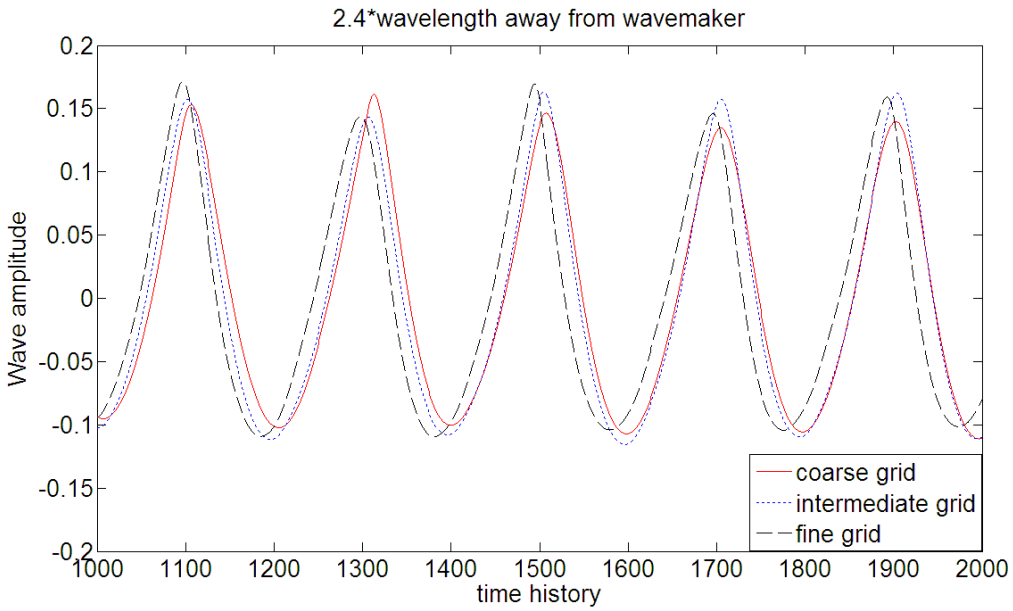

Figure 4.4: The convergence test

From the figure 4.4, we can find that if we use the finer grid, we will get more accurate and more stable solution. In the coarse grid, the wave decay is clearly to see within 1000 time steps. If we use intermediate grid and fine grid, both of them can keep the wave shape well and there exists little wave decay. In addition, in intermediate grid, the wave height seems to keep stable after 1500 time steps; in fine grid, the wave shows some nonlinear characteristic due to some wave height oscillating. In present study, I will use the intermediate grid to simulate the wave propagation.

4.2.2 Reynolds Number

Reynolds number is a dimensional number that gives a measure of the ratio of inertia forces to viscous forces and consequently quantifies the relative importance of these two types of forces for given flow conditions. It also can characterize different

flow regimes, such as laminar or turbulent flow. As we all know, laminar flow occurs at low Reynolds numbers, where viscous forces are dominant, and is characterized by smooth, constant fluid motion, while turbulent flow occurs at high Reynolds numbers and is dominated by inertial forces, which tend to produce random eddies, vortices and other flow instabilities.

In this case, we choose two different Reynolds numbers: 30,000 and 3,000,000 respectively. In each situation, there are a variety of gages which measure the wave amplitude locally between the wave maker and the damping beach. The details can be studied in figure 4.5. We can find that there is no big difference between the results in these two situations. The reason is: we assume that this method is used to evaluate the laminar in two dimension plane with fixed orthogonal grids. We do not introduce the turbulence model in present study. In other words, Reynolds number does not affect the result much and it will not become our concern. In following case, we prefer to choose Reynolds number as 30,000.

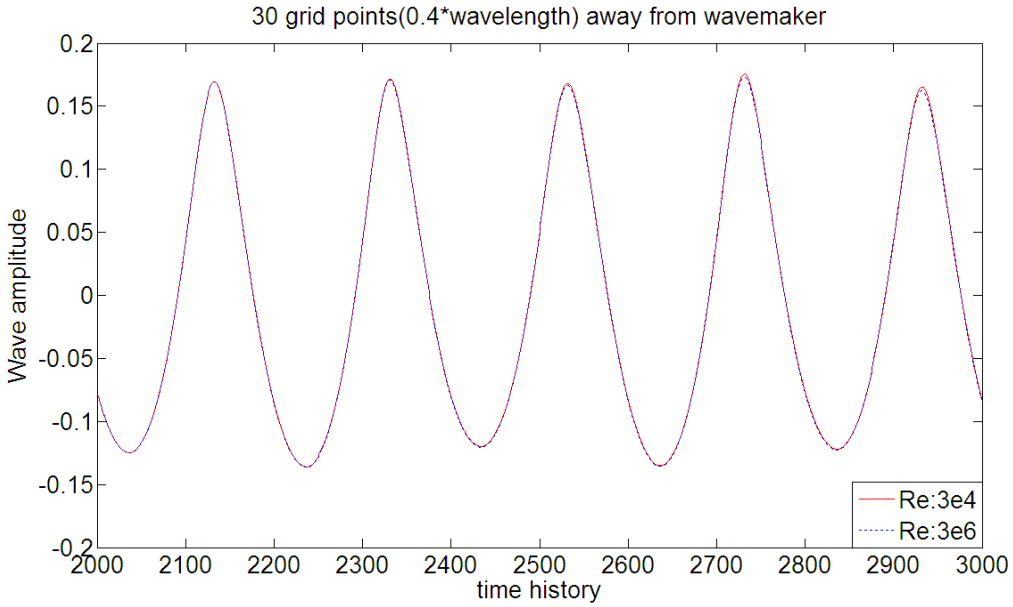

(a) gage located at 0.4λ away from wave maker

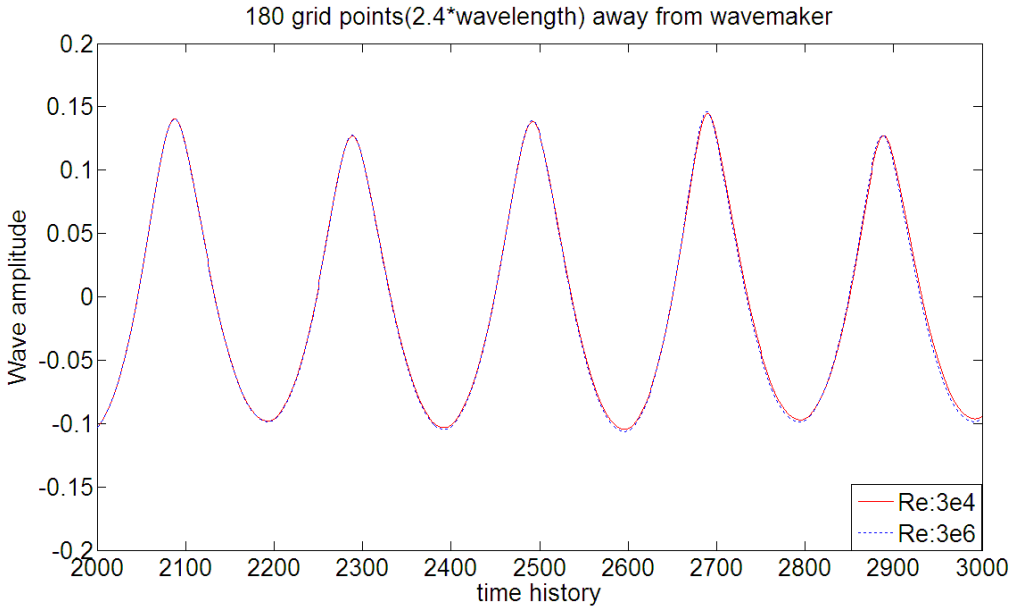

(b) gage located at 2.4λ away from wave maker

Figure 4.5: Reynolds Numbers at some gage positions

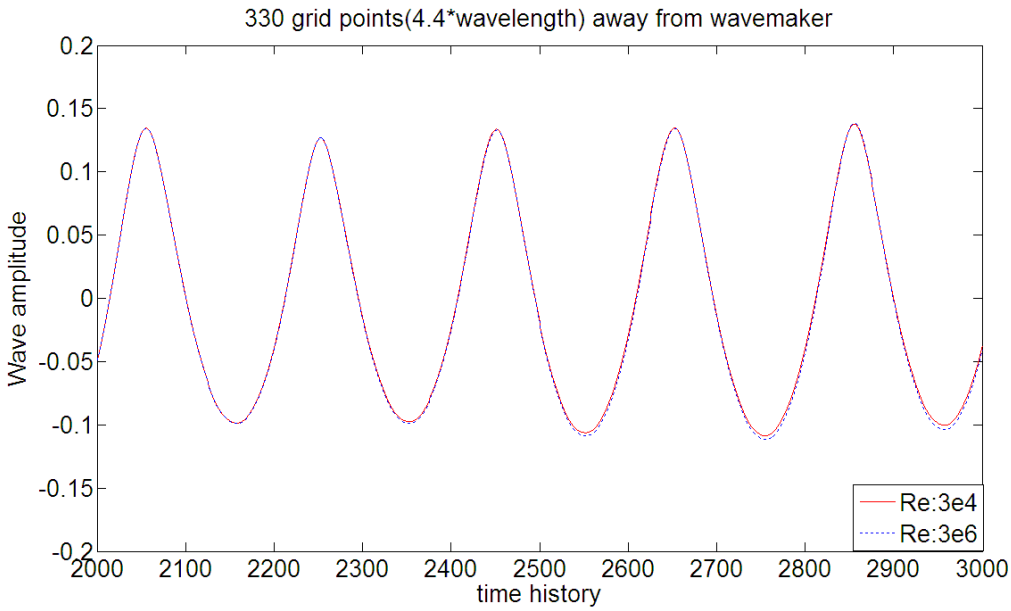

(c) gage located at 4.4λ away from wave maker

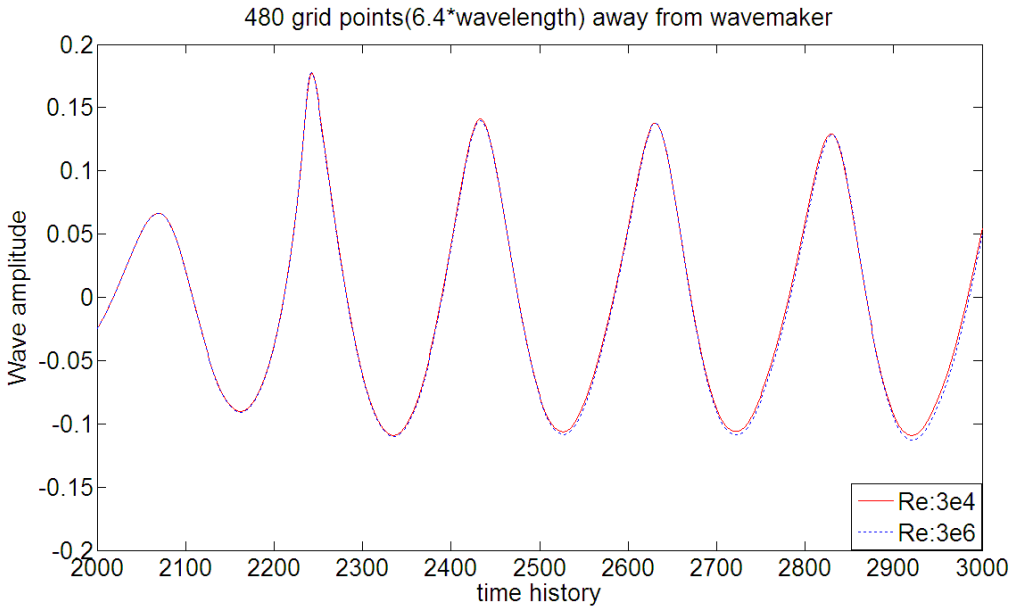

(d) gage located at 6.4λ away from wave maker

Figure 4.5: (Continued)

4.2.3 The Order in Time

To solve the RANS equations, we introduce method with different orders in time. In numerical sense, the higher order in time will obviously keep more accuracy and have better solutions. From figure 4.6, we find that the results with second order in time are better to keep the constant wave height compared with that with first order in time. Thus, the second order in time parameter can make the results reasonable.

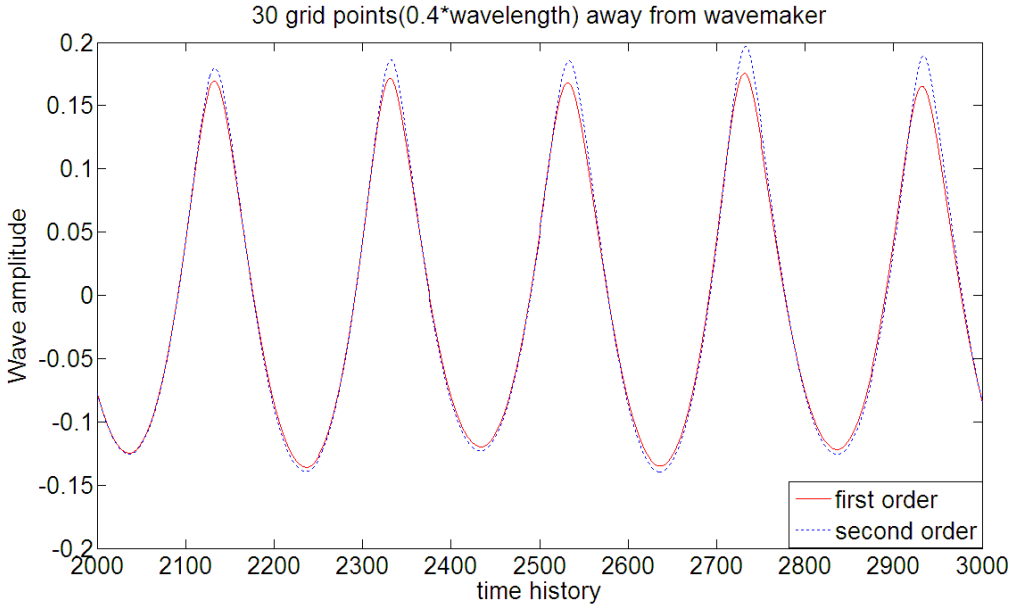

(a) gage located at 0.4λ away from wave maker

Figure 4.6: The comparison of different orders in time

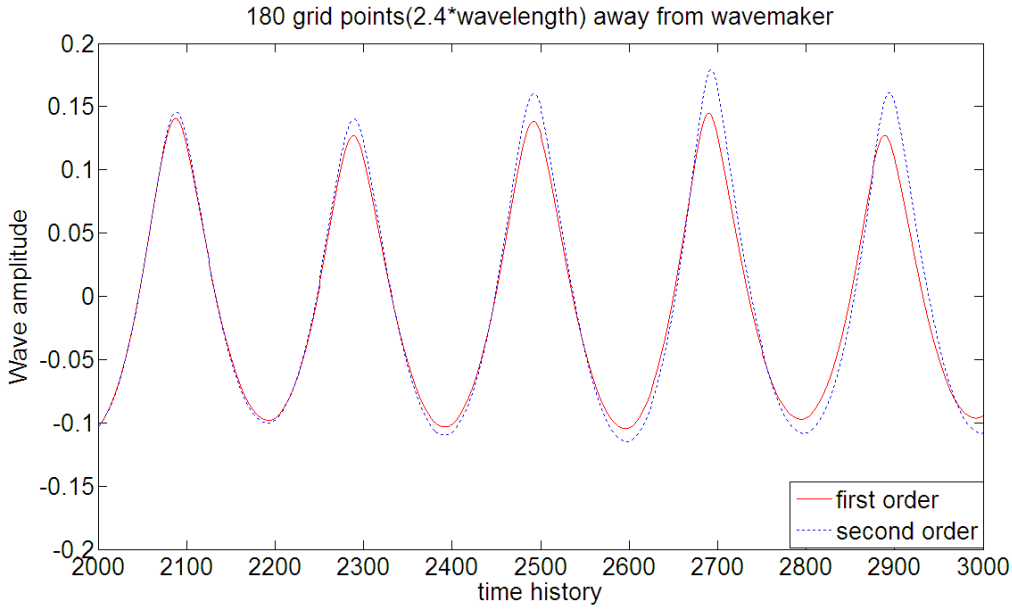

(b) gage located at 2.4λ away from wave maker

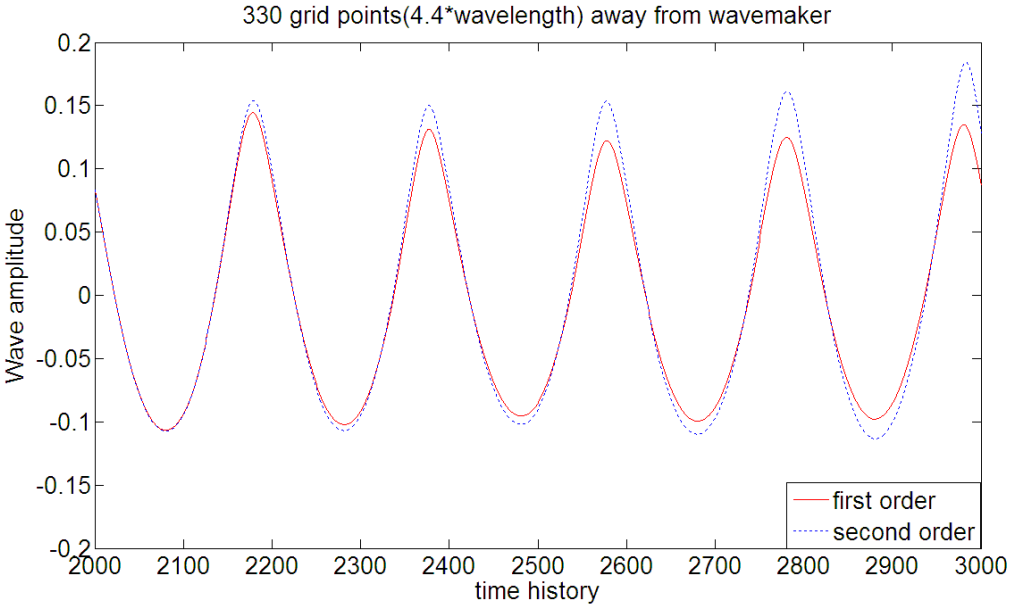

(c) gage located at 4.4λ away from wave maker

Figure 4.6: (Continued)

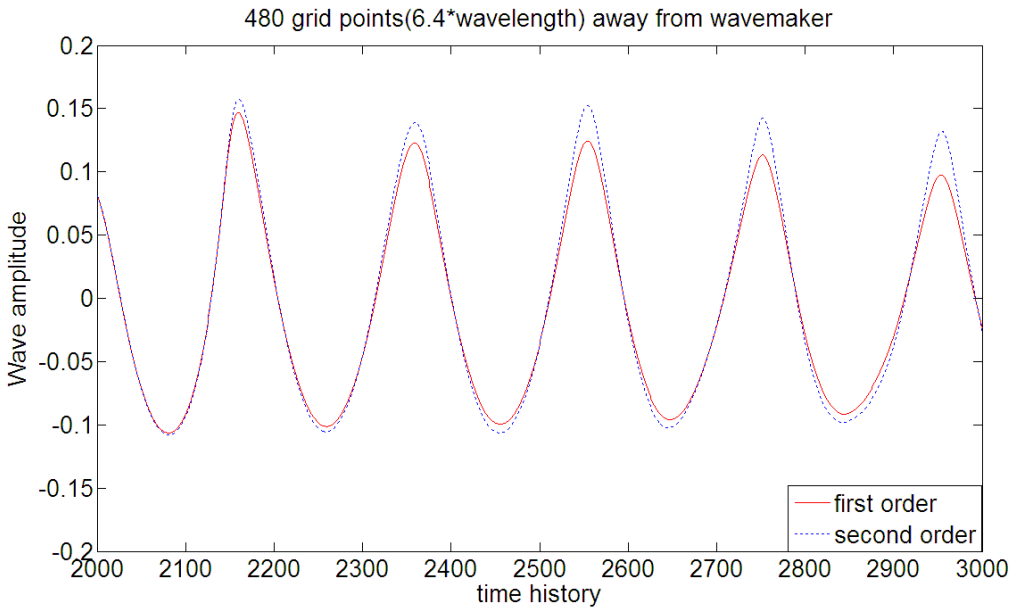

(d) gage located at 6.4λ away from wave maker

Figure 4.6: (Continued)

4.2.4 Global Iteration within Each Time Step

Global iteration within each time step means to divide the duration of one time step into more small sub-time steps in the momentum equation resolution. In other words, it decreases the time increment when the code computes the momentum equation. From figure 4.7, it proves that the relatively large global iteration within each time step will enhance the results accuracy especially in the region far away from the wave maker.

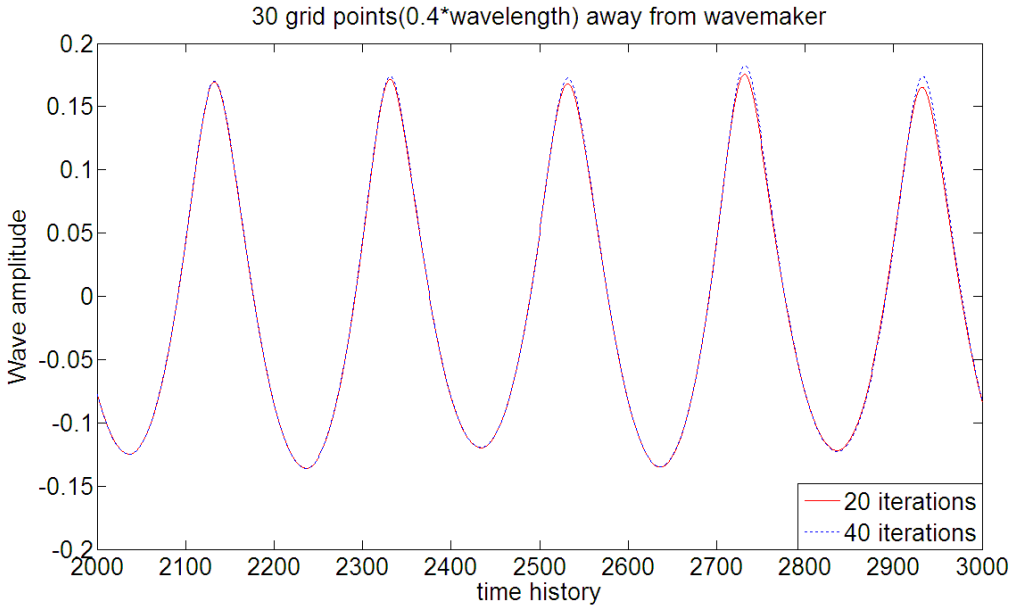

(a) gage located at 0.4λ away from wave maker

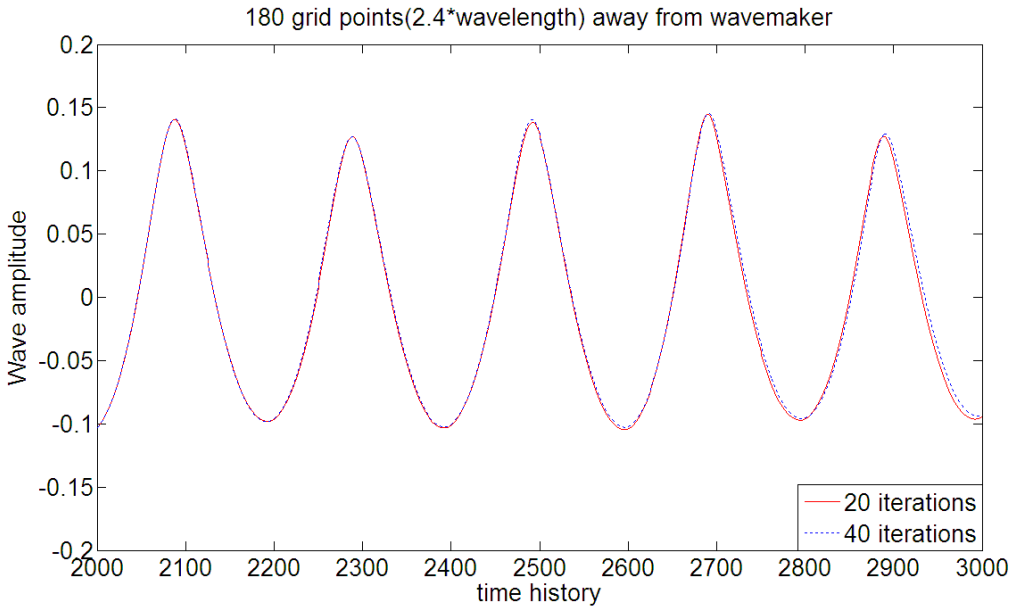

(b) gage located at 2.4λ away from wave maker

Figure 4.7: The comparison of different global iteration within each time step

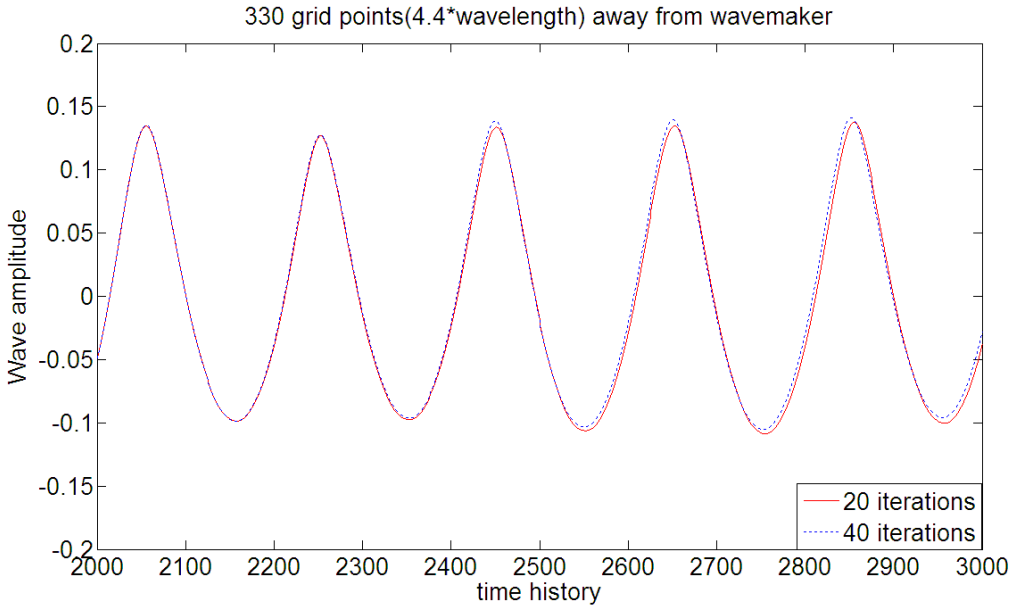

(c) gage located at 4.4λ away from wave maker

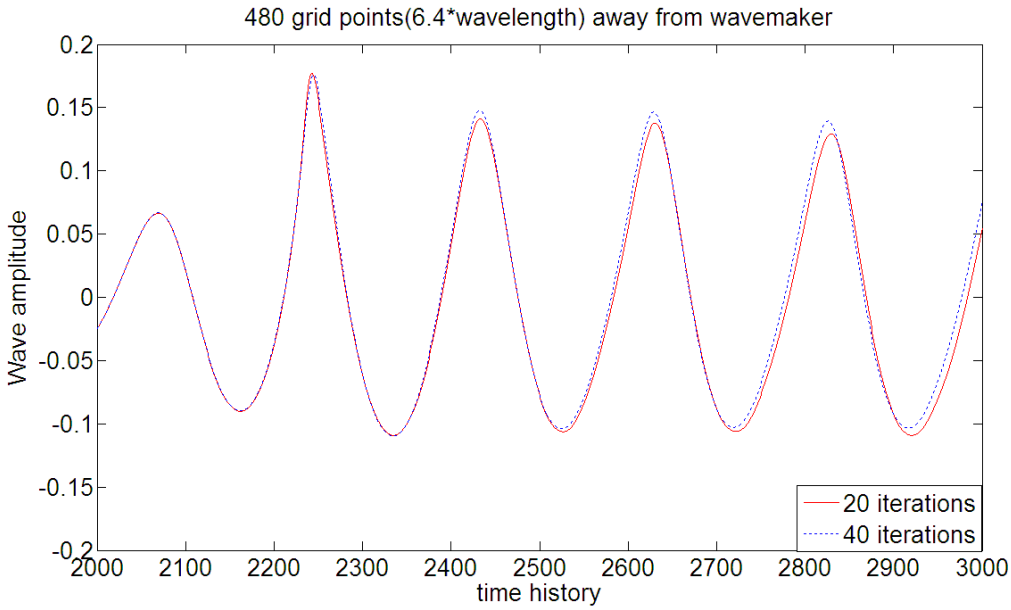

(d) gage located at 6.4λ away from wave maker

Figure 4.7: (Continued)

4.2.5 Time Increment

Time increment is similar with the global iteration within each time step. The difference is that time increment will modify the global time scale not only in moment equation but also in level set equation. Thus, figure 4.8 shows that the less time increment is used, the better the solution is obtained. Additionally, the time increment affects the results rather more than does the global iteration for the reason that the former one shortens the time increment in both RANS equations and level set equation. In plot (d), we can observe that the wave amplitude in time series will stick to stable with the less time increment more than six wavelengths far away from wave maker; contrarily, with the larger time increment the results at that furthest gage is becoming unstable.

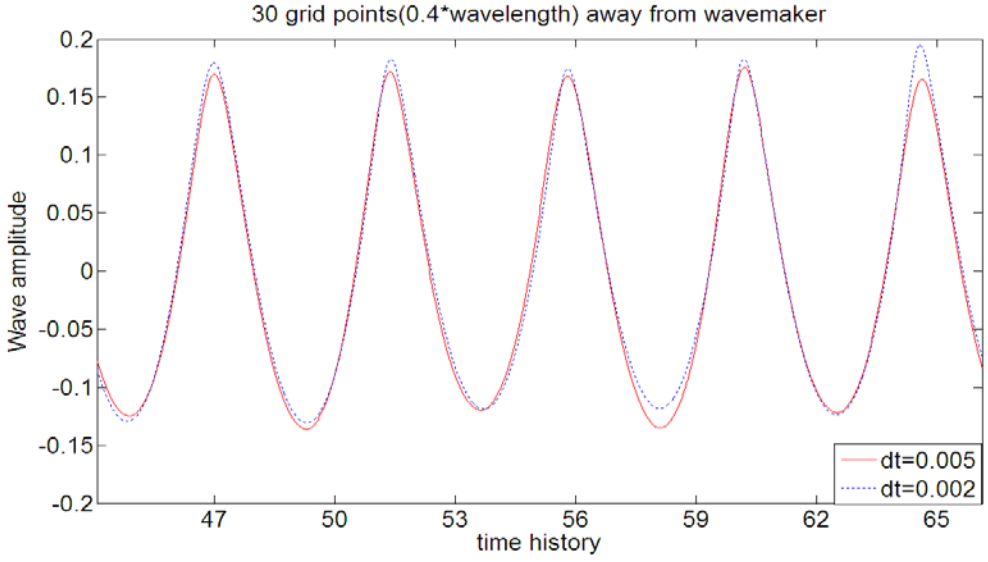

(a) gage located at 0.4λ away from wave maker

Figure 4.8: The comparison of different time increments

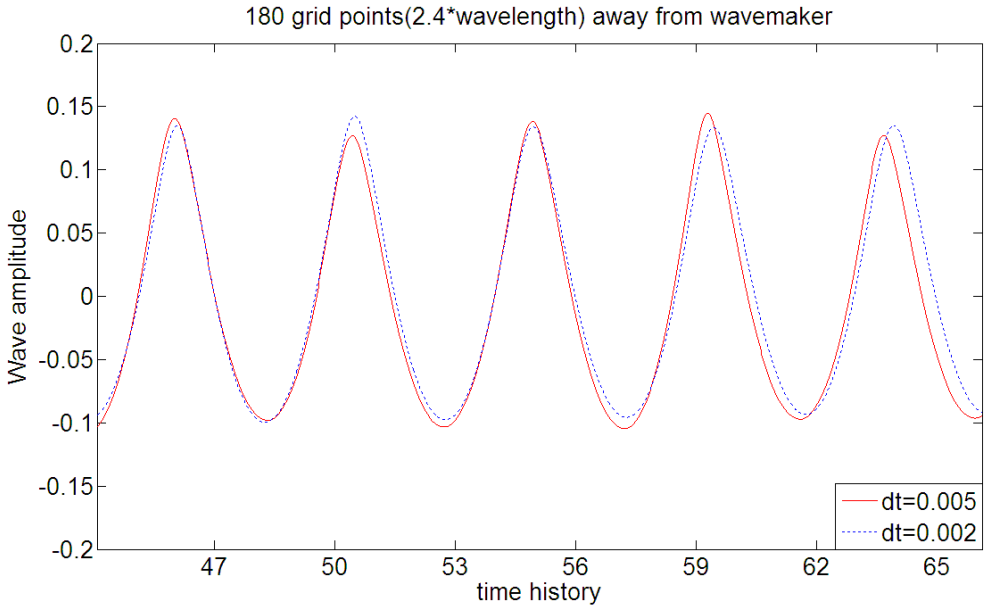

(b) gage located at 2.4λ away from wave maker

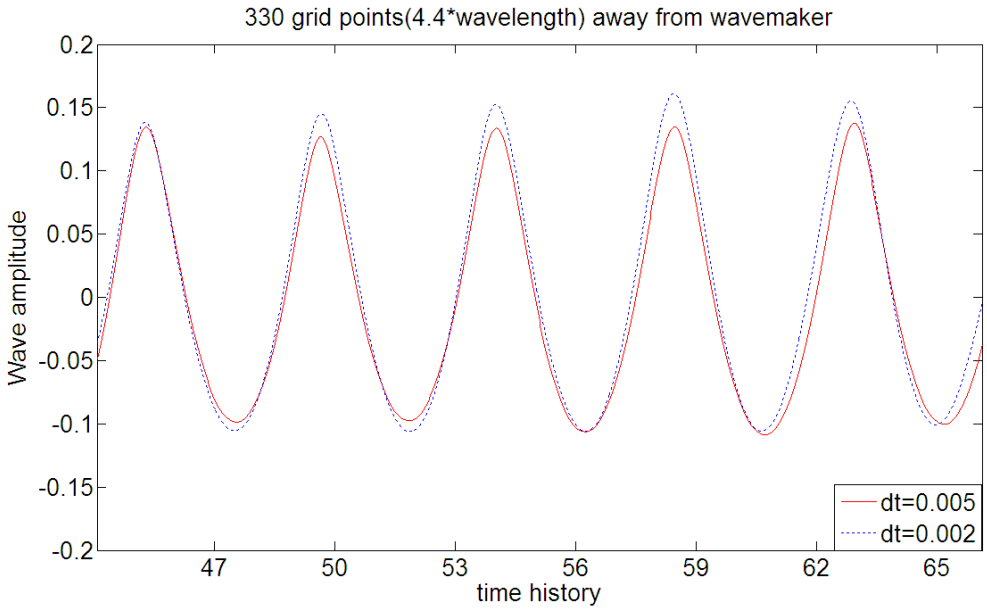

(c) gage located at 4.4λ away from wave maker

Figure 4.8: (Continued)

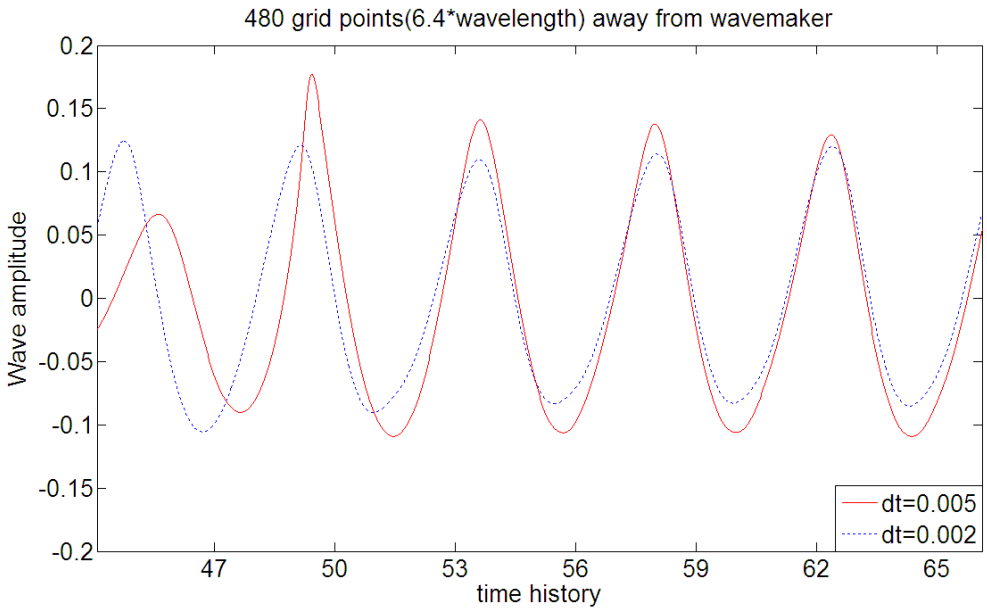

(d) gage located at 6.4λ away from wave maker

Figure 4.8: (Continued)

4.3. Analysis of Velocity-Extrapolation

Velocity-Extrapolation is used to help create some overturning wave phenomena by extrapolating the velocity field above the water region. It is critical to simulate the green water or breaking wave in the region. We study the only first wavelength away from the wave maker. We can find that the wave applied by velocity-extrapolation is relatively lower than that without velocity-extrapolation. The decrease ratio is about 10% at the gage one wavelength downstream from wave maker. Thus, the velocity-extrapolation routine indeed damages the accuracy of solution, but from the figure 4.9 we can see the damage is not so serious. Whether applying the velocity-extrapolation or

not, it is up to the feasibility of this routine. The next section will further explain and prove the ability of velocity-extrapolation in creating overturning waves.

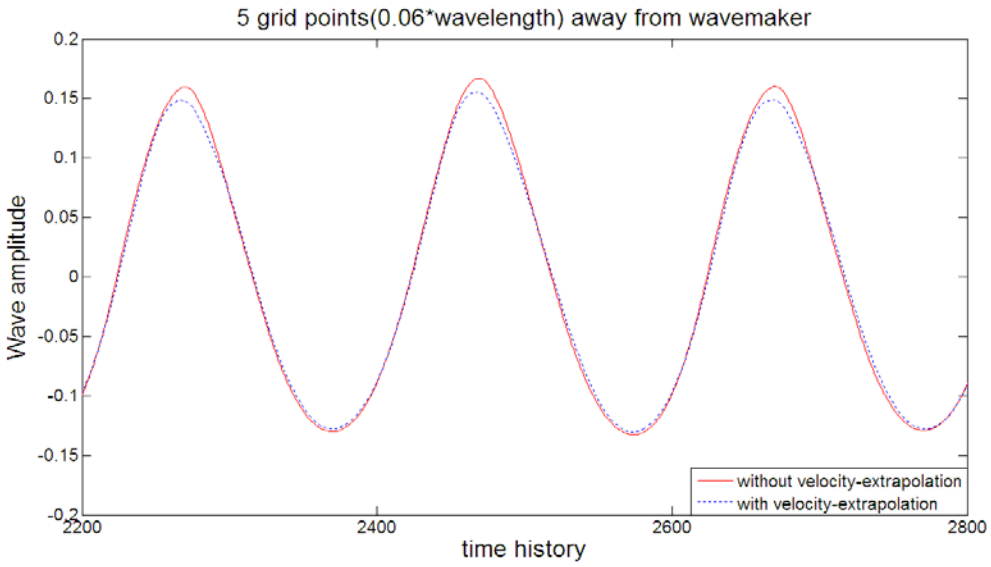

(a) gage located at 0.06λ away from wave maker

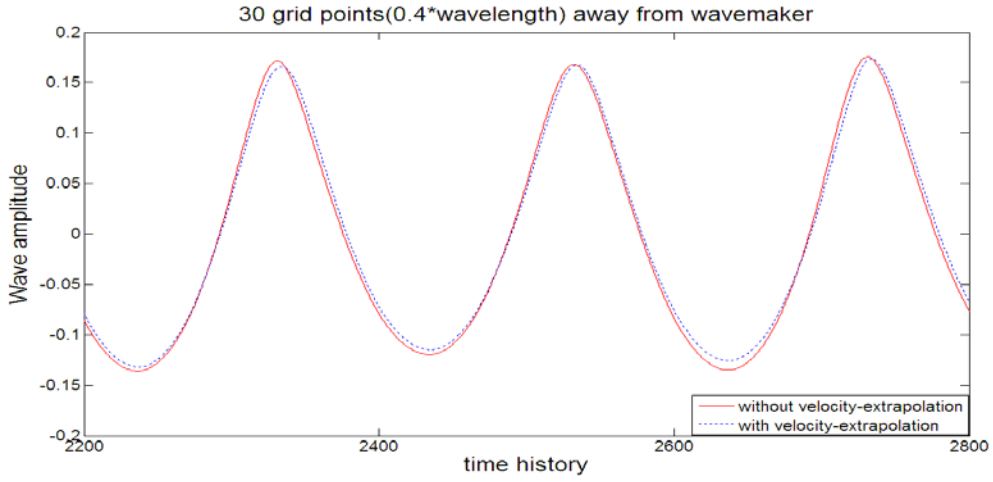

(b) gage located at 0.4λ away from wave maker

Figure 4.9: The comparison of results with and without velocity-extrapolation

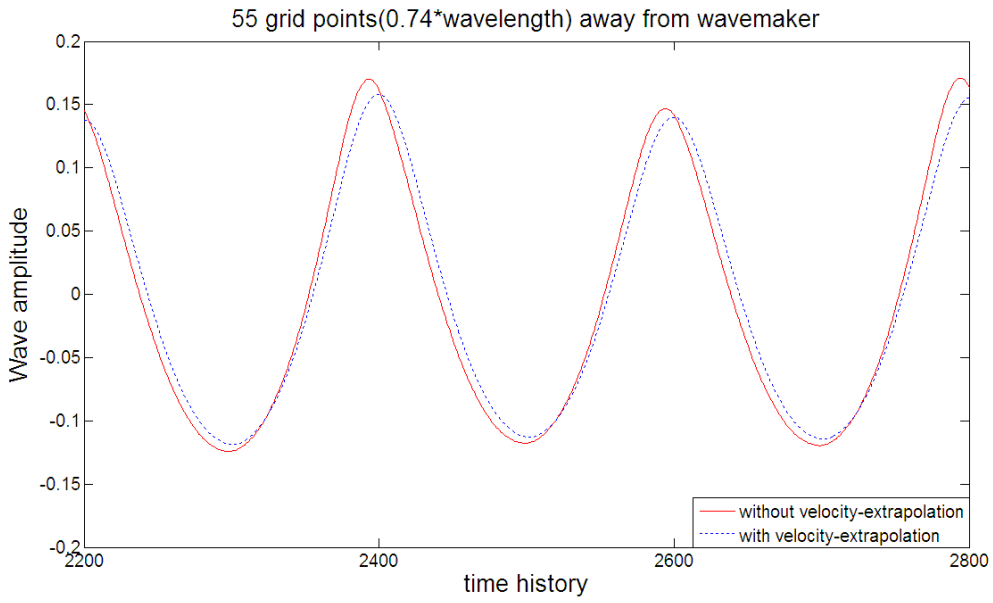

(c) gage located at 0.74λ away from wave maker

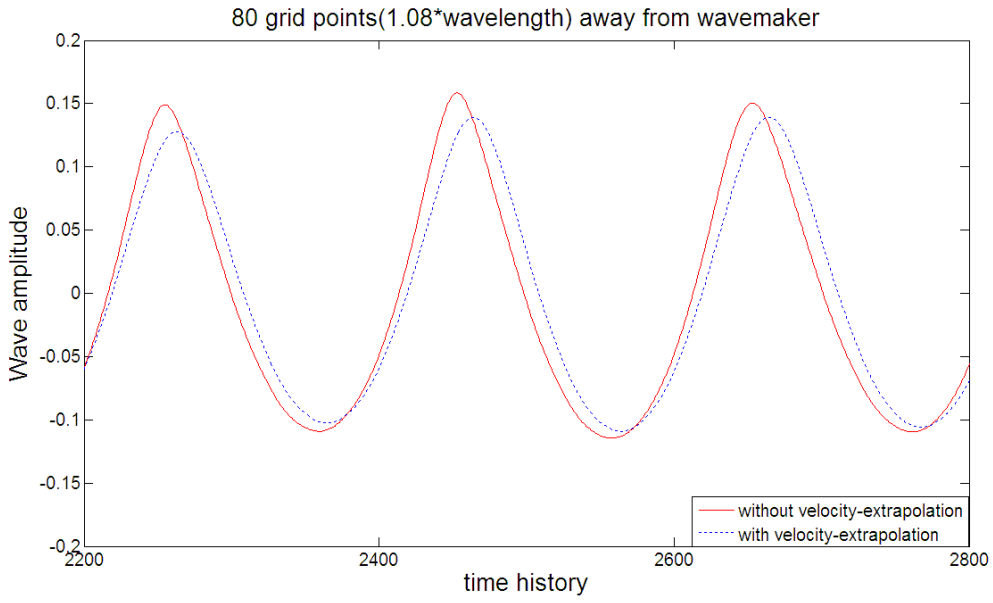

(d) gage located at 1.08λ away from wave maker

Figure 4.9: (Continued)

In conclusion, some parameters indeed sensitively affect the result. Thus, we should treat and set their values cautiously. And according to the numerical sense, it is straightforward to decrease the time increment and grid size in order to obtain the better results. In following tests, I will do it in this way: 1. Give relatively small Reynolds number because there is no obvious difference between high Reynolds number and low Reynolds number; 2. Using second order in time to solve the momentum equation in order to keep the propagation of wave stable; 3. Using more iteration within each time step; 4. Using smaller time increment; 5. Trying to turn on velocity-extrapolation routine in the block where we need to observe the breaking wave or green water. In addition, after maintaining the goal of high accuracy, we also need to take care of code efficiency. As we all know, the cost of decreasing the time increment is to consume more CPU time. If the decay is not too much, we can tolerate a little decay and give up continuing improving the accuracy. Thus, we should keep the balance between the accuracy and efficiency.

4.4. Simulations of Green Water

The final case is to simulate the green water around a two-dimensional platform. In this case, we can simulate the green water around a two-dimensional platform by using level set RANS method [37].

Firstly, we introduce the grid in figure 4.10. There are five blocks in the grid: 1. Wave maker is to generate the linear regular wave with dimension 3*51*121; 2. Tank 1 is the region where the wave propagates to the platform and the level set equation and

RANS equations are solved with the dimension 3*201*121; 3. above deck is the region where can track the green water or breaking wave beyond the platform deck; 4. under deck is the region where can observe the wave properties beneath the deck; Above two blocks' dimension will be adjusted by the goal of test. 5. Tank 2 is to damp the incoming wave in order to decrease the reflecting wave effect with the dimension 3*41*121. All the grid size is as same as the grid used in last case to maintain the good wave propagation. And the wave properties are also adopted as same as those in last case:

Wave height is $A = 0.15$.

Wavelength is $\lambda = 3$.

Water depth is $h = 1$

According to the wavelength and grid size, we can compute the domain length relative to wavelength. For the first tank length, it is about more than two wavelengths. For the deck length, it is about one wavelength. And for the damping beach, it is more than four wavelengths. Referring to figures in last case, we can initially know that the wave decay is quite small.

In present case, the incoming wave properties are constant and the deck will be adjusted to different heights. Under different deck heights, there are some distinct phenomena [38]. The deck height is respectively adjusted to satisfy following conditions:

Position I: The deck is so high that the wave cannot reach the deck bottom. Thus, the wave can freely move under the deck.

Position II: The deck is a little bit higher than mean water level but the wave can impact on the deck bottom while the wave crests.

Position III: The deck is a little bit lower than mean water level and the wave passes through above the deck.

Position VI: The deck continues to decline to the middle of water depth.

Position V: The deck is standing nearby the water bottom.

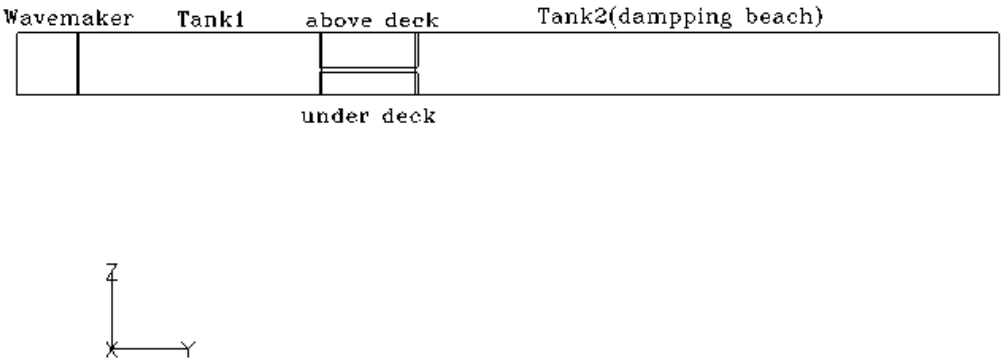

(a) overview of the grid

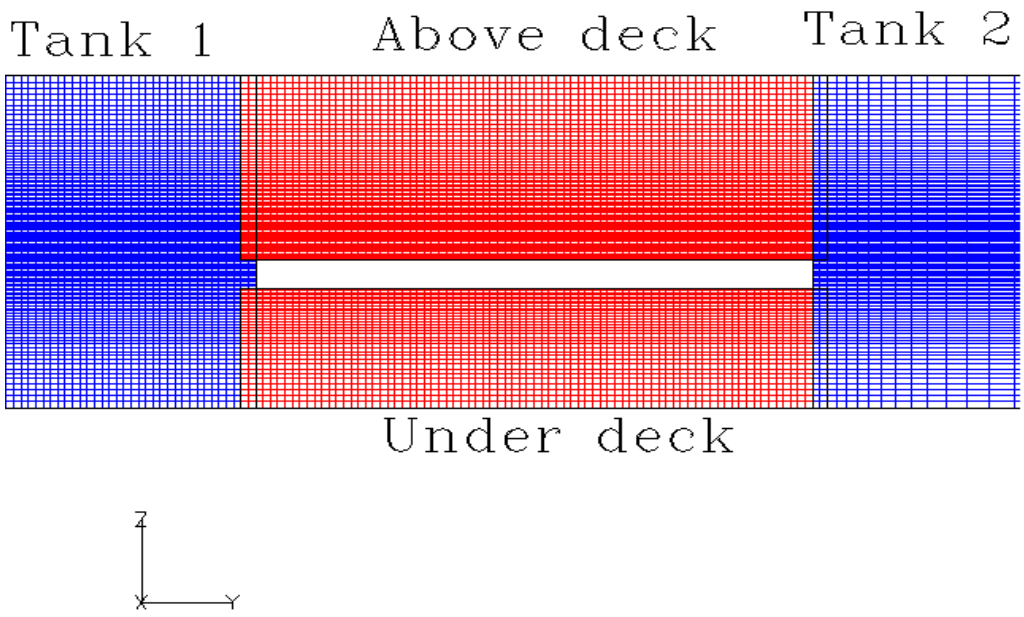

(b) the grid around a two-dimensional platform

Figure 4.10: The grid for simulation of green water around platform

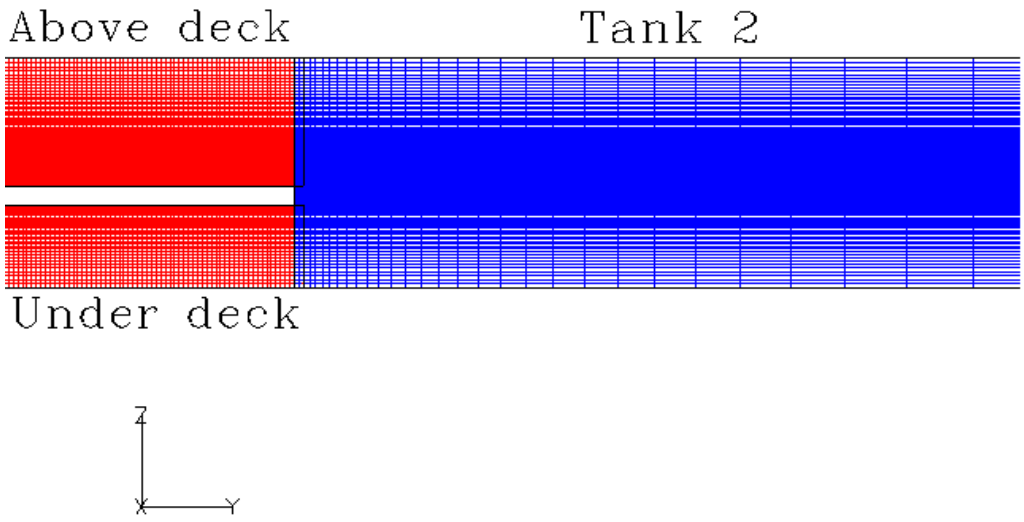

(c) the overlapping between platform and the downstream region

Figure 4.10: (Continued)

4.4.1 Position I

In position I situation, the deck is so high that the wave cannot reach the bottom of deck. Thus, the wave will propagate freely along the domains. It is the similar with previous propagation of regular wave case. In this case, we can test the Chimera technique which is used to interpolate the values in the overlap region. From figure 4.11, we can find that in every overlap region between neighboring blocks, the dynamic pressure contour can smoothly connected, which proves the ability of Chimera technique. Moreover, in first two domains, although the contour pattern seems to be similar, the essence is completely different: in the first domain, the wave amplitude, water velocities and pressure are prescribed in according to the linear wave theory; alternatively, in the second domain, those values are obtained by solving RANS equations which involves

non-linear equations. We can continue to using linear wave properties as known incoming wave because the linear wave properties are coupled with non-linear wave properties consistently.

In addition, it also can test the feasibility of damping beach. In the last domain, we decrease the wave amplitude and pressure artificially due to there is not viscosity effect in our code. The damping function and coarser grid of tank 2 are applied to make sure reflection wave effect as little as possible. From plot (a) to plot (f), we can observe the wave propagating along the tank 1, under deck and then is damped in damping beach.

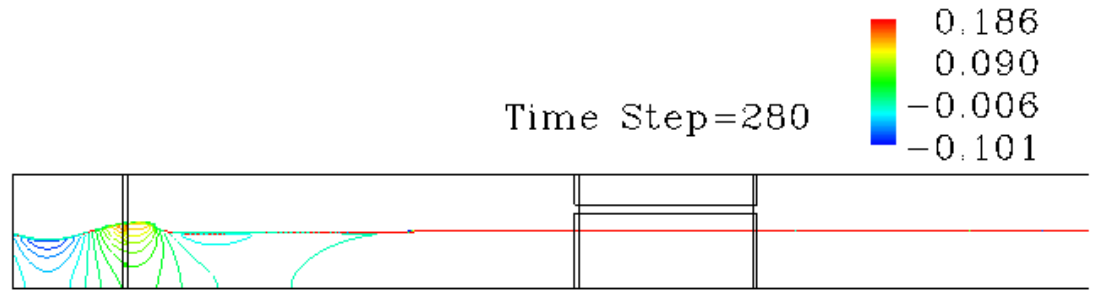

(a)

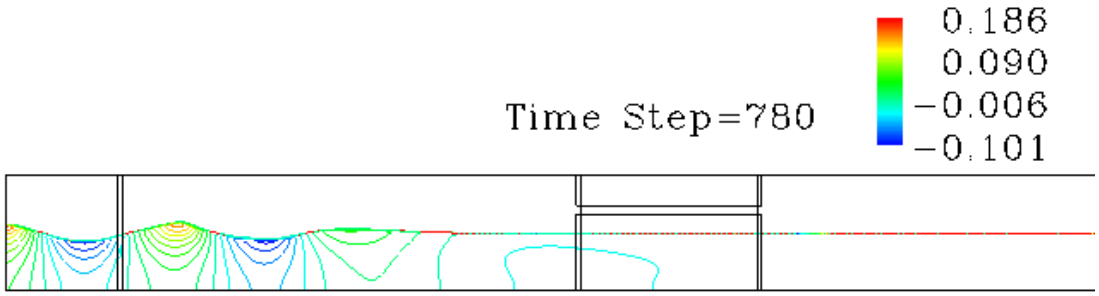

(b)

Figure 4.11: Evolution of wave and dynamics contour in position I

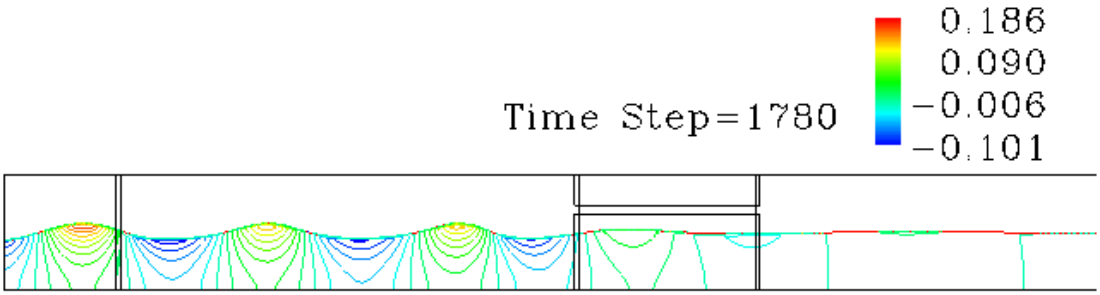

(c)

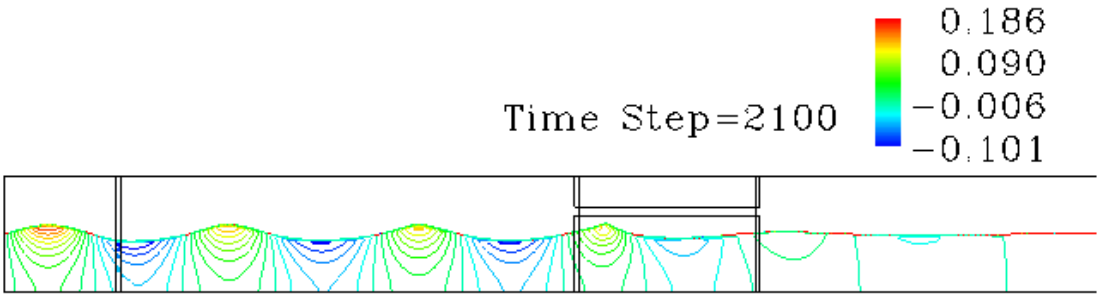

(d)

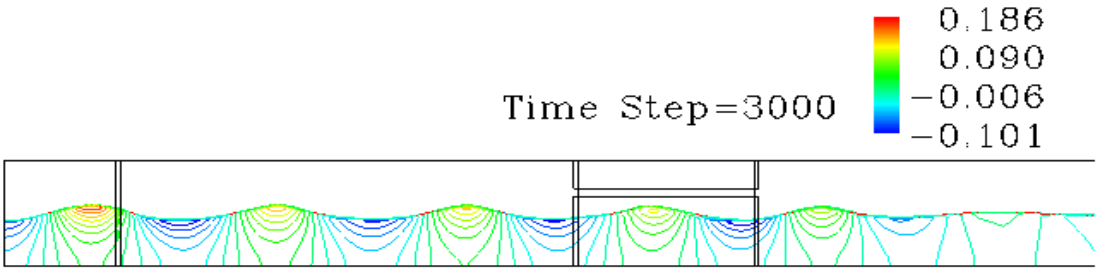

(e)

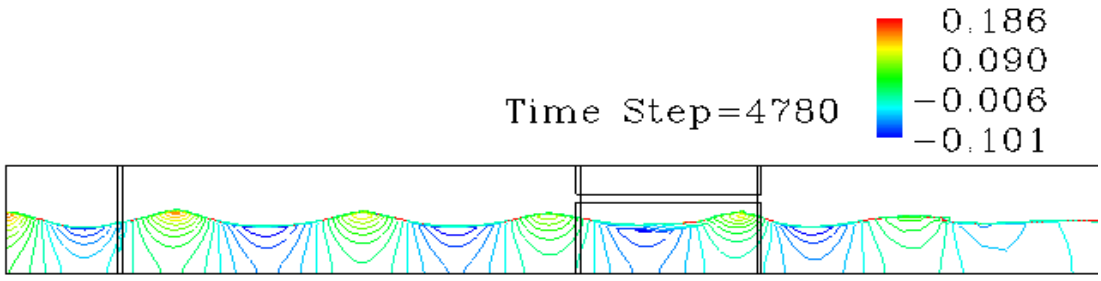

(f)

Figure 4.11: (Continued)

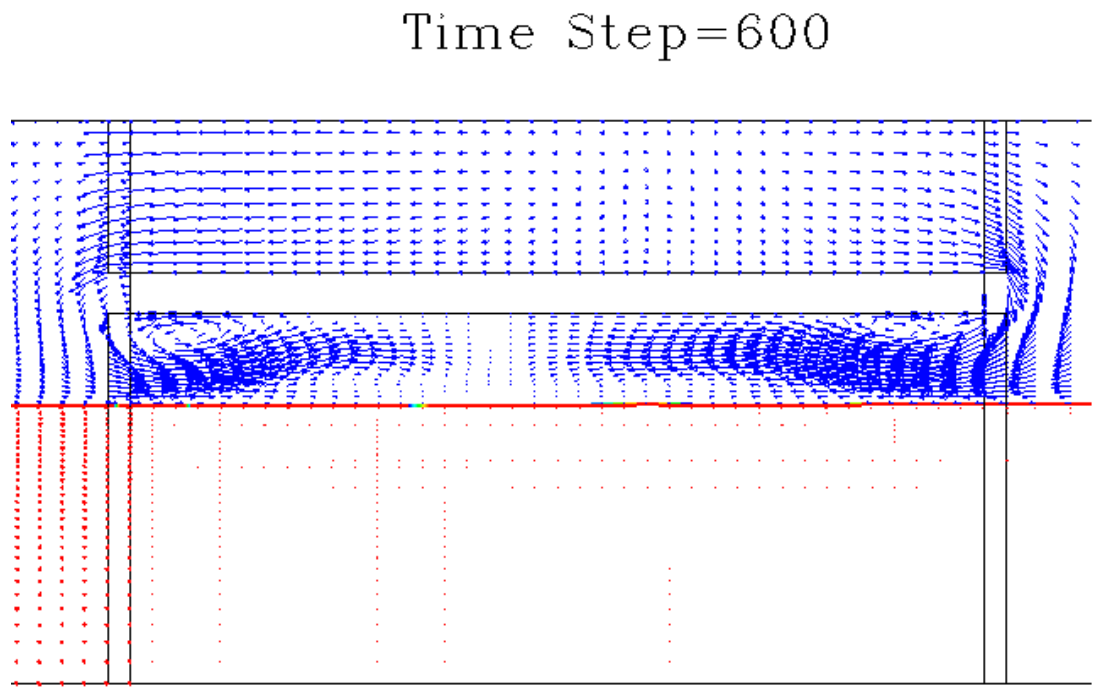

(a)

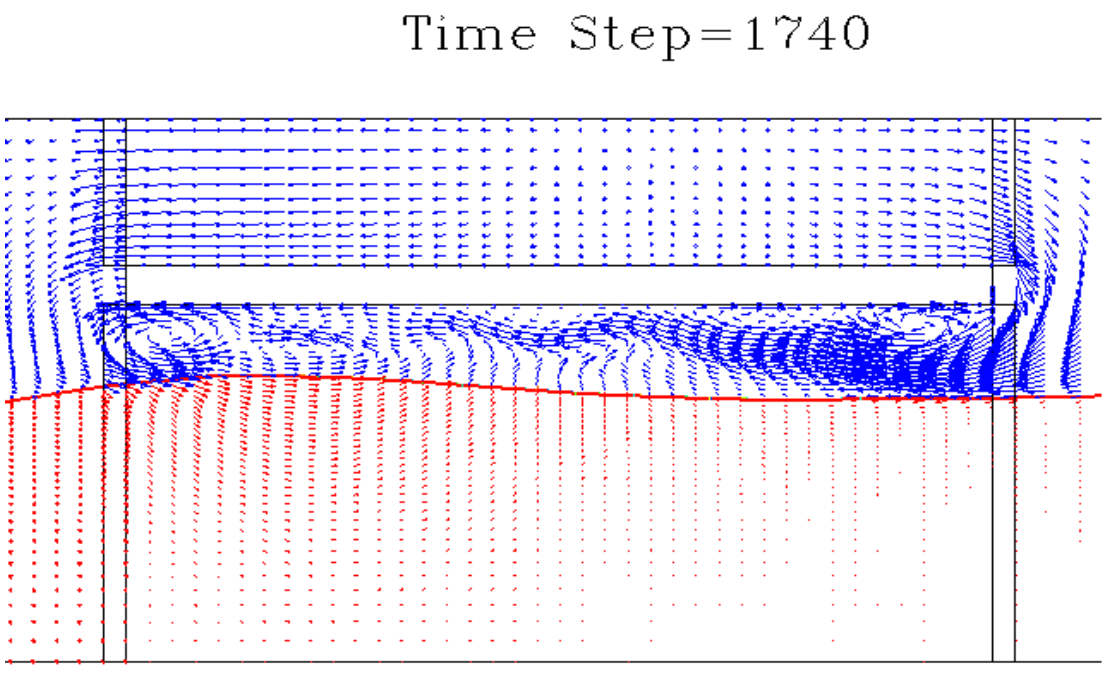

(b)

Figure 4.12 Velocity field induced by the wave in position I

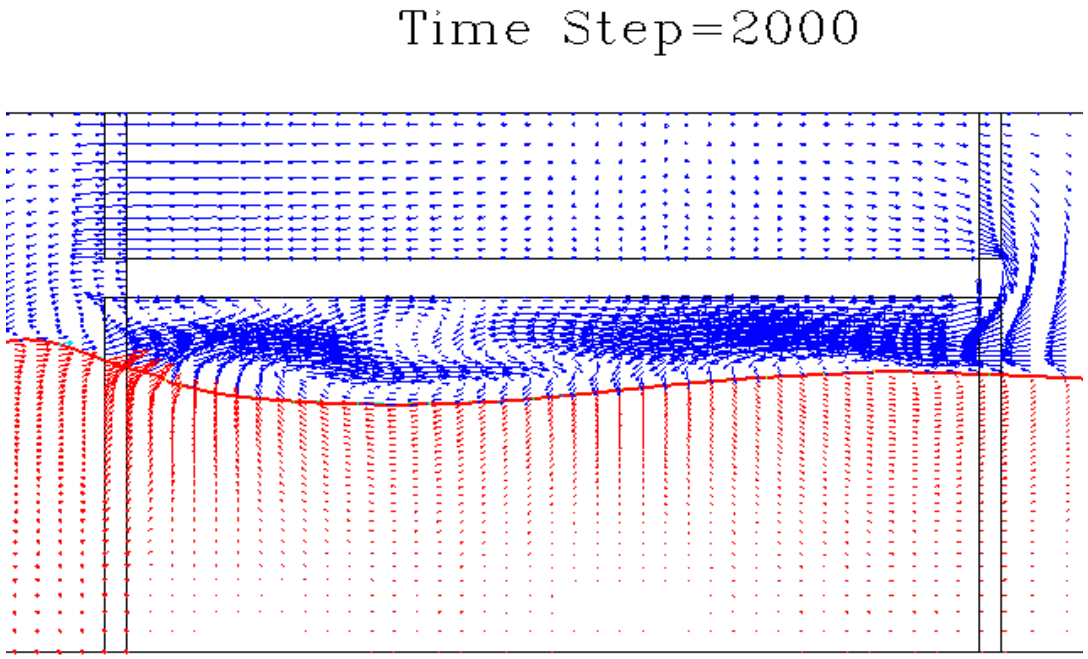

(c)

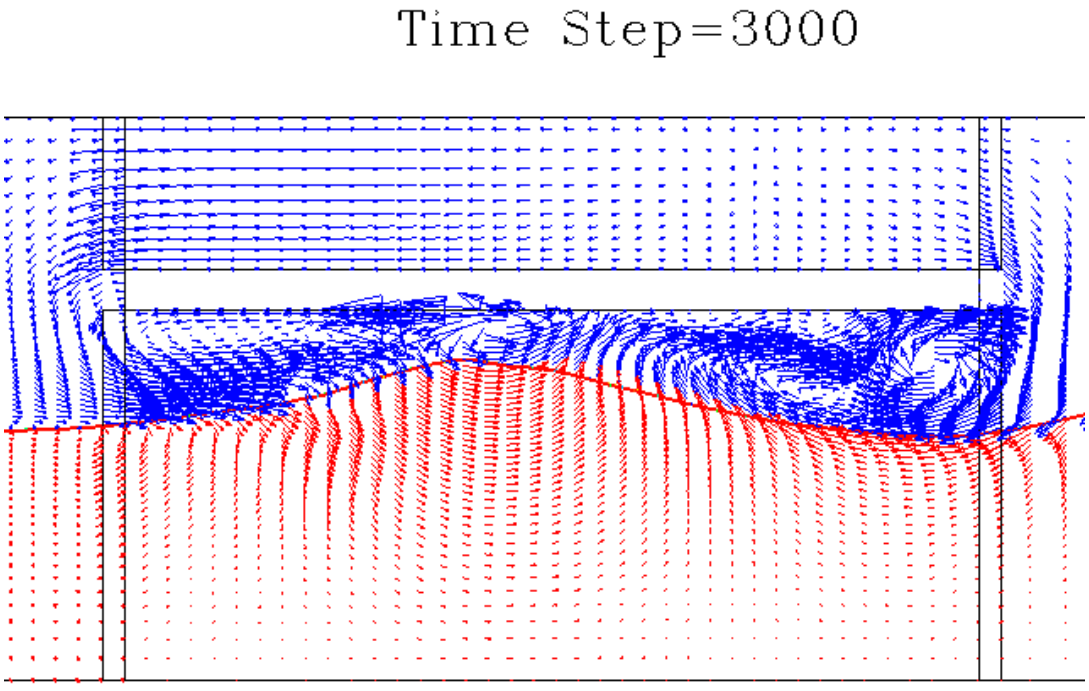

(d)

Figure 4.12: (Continued)

Figure 4.12 shows that the velocity field focused in the platform region. With the time elapsing, the air velocity under the deck is becoming larger and more chaotic. Although the air velocity is substantially changed, the air field is not our concern because the density of air is rather less than that of water. Thus, the air cannot affect the water motion much. From figure 4.5 to figure 4.8, we also can observe the wave profile does not decline or change much. It also keeps the regular wave consistently. Under water free surface, the velocity profile is also similar with the profile in linear wave theory.

4.4.2. Position II

When the wave propagates under the deck and the wave crest will impinge the bottom of deck.

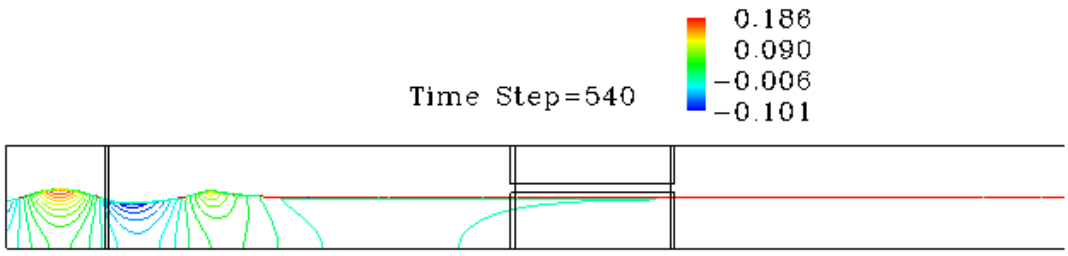

(a)

Figure 4.13: Evolution of wave and dynamics contour in position II

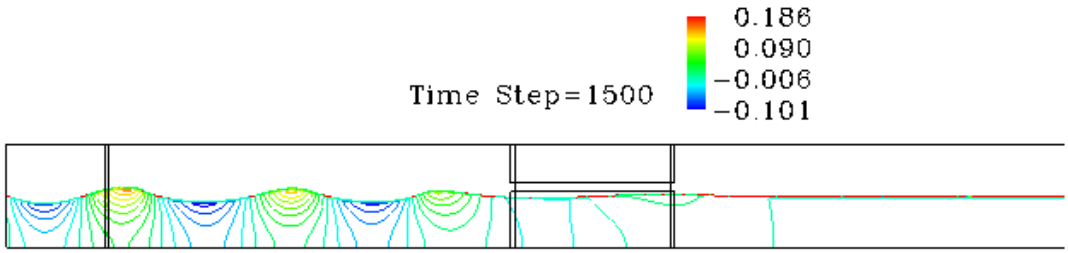

(b)

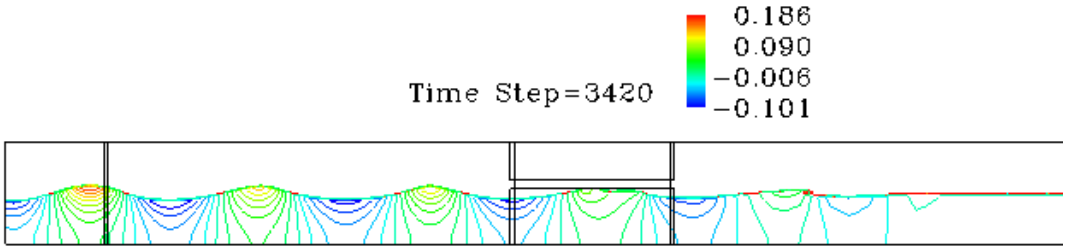

(c)

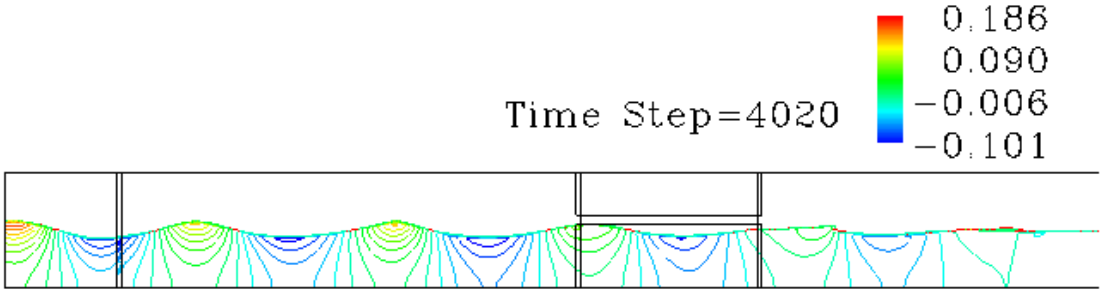

(d)

Figure 4.13: (Continued)

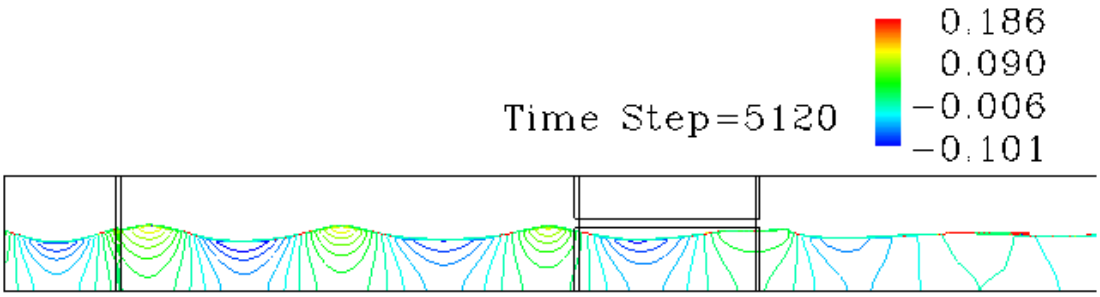

(e)

Figure 4.13: (Continued)

Figure 4.13 presents the difference between dynamics pressure in the tank 1 and dynamic pressure under the deck. When the wave impacts the deck, it obviously decreases the pressure contour pattern due to the standing deck. And the pressure is relatively smaller than the normal pressure value.

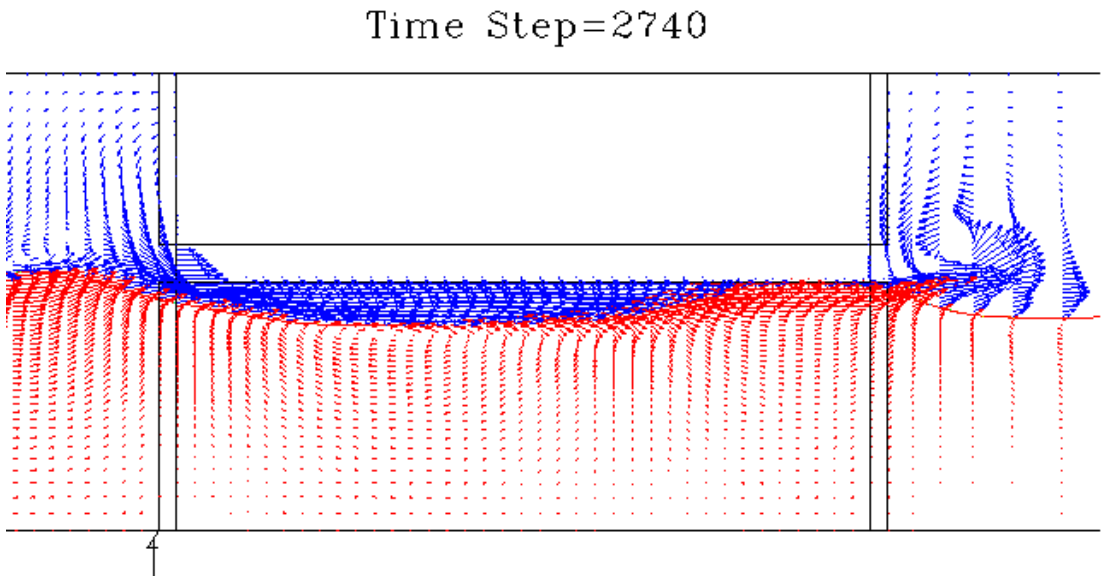

(a)

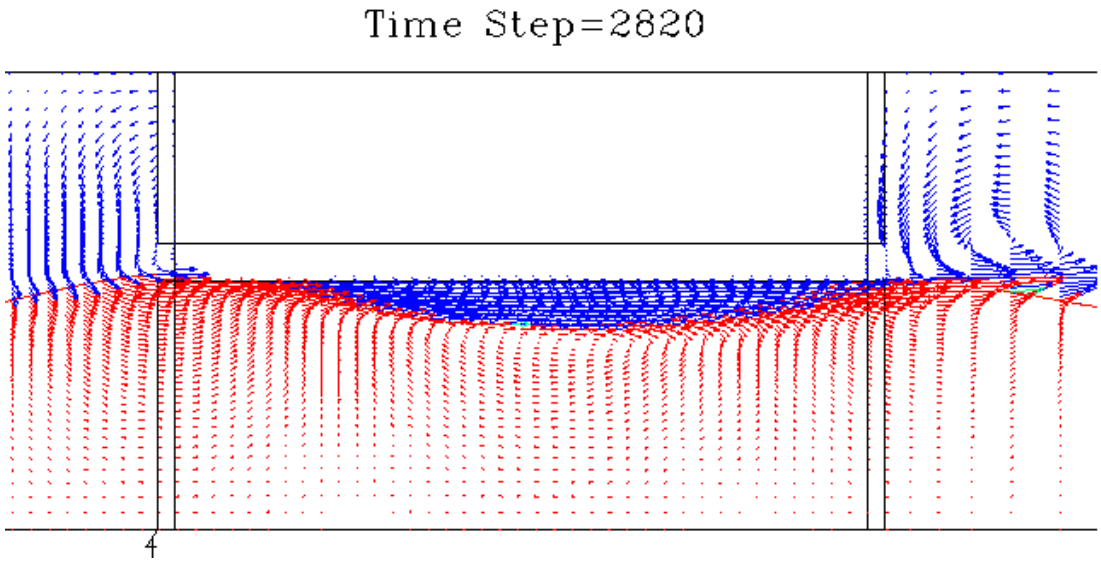

(b)

Figure 4.14: Velocity field induced by the wave in position II

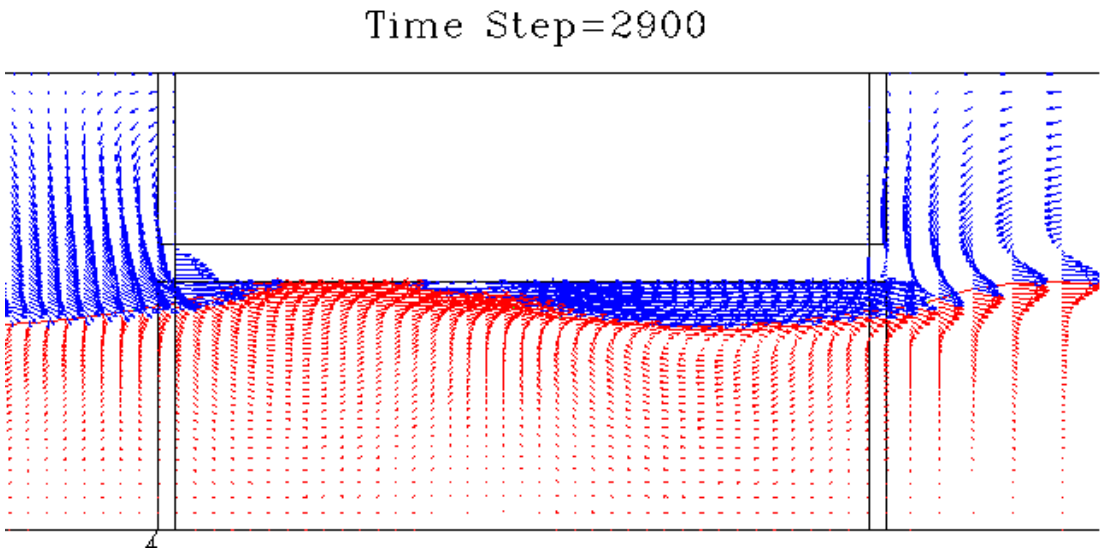

(c)

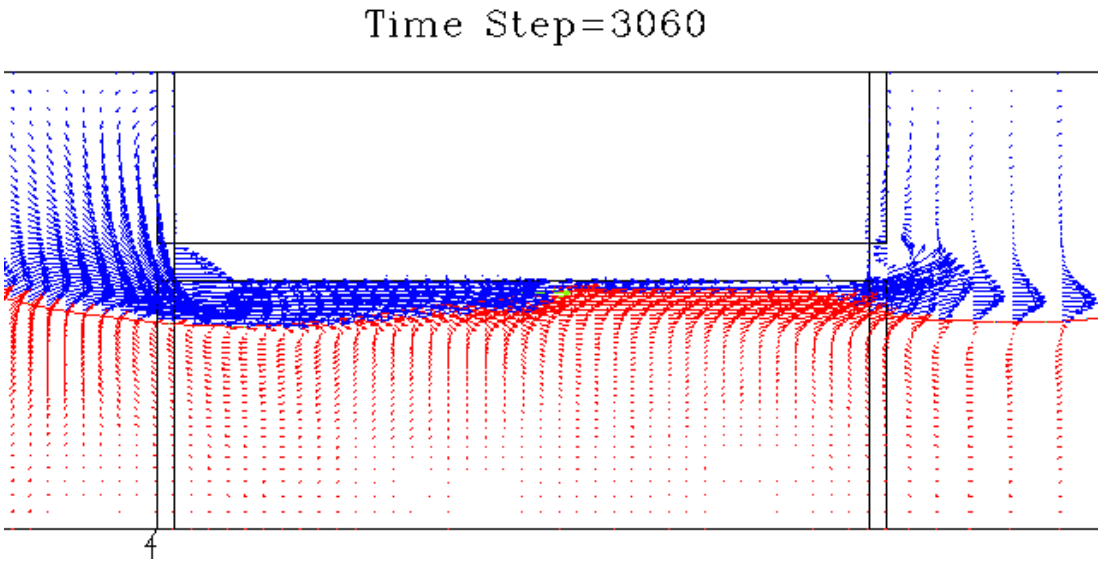

(d)

Figure 4.14: (Continued)

Figure 4.14 can tell us the details under deck about velocity field and interface information. When the water particle is travelling upwards and then the structure will impede the motion of water, thus the water will adhere to the deck bottom and move in the horizontal direction. The change of vertical momentum will be transformed to the force impinging on the deck.

4.4.3. Position III

When the deck is closely under the still water level, the incoming wave will propagate over the deck and is disturbed by the standing structure.

Firstly, let us test the ability of velocity-extrapolation routine by turning it on and off above the deck region. The comparison of the phenomena with and without velocity-extrapolation can show some efficient way to create the green water around the deck [39].

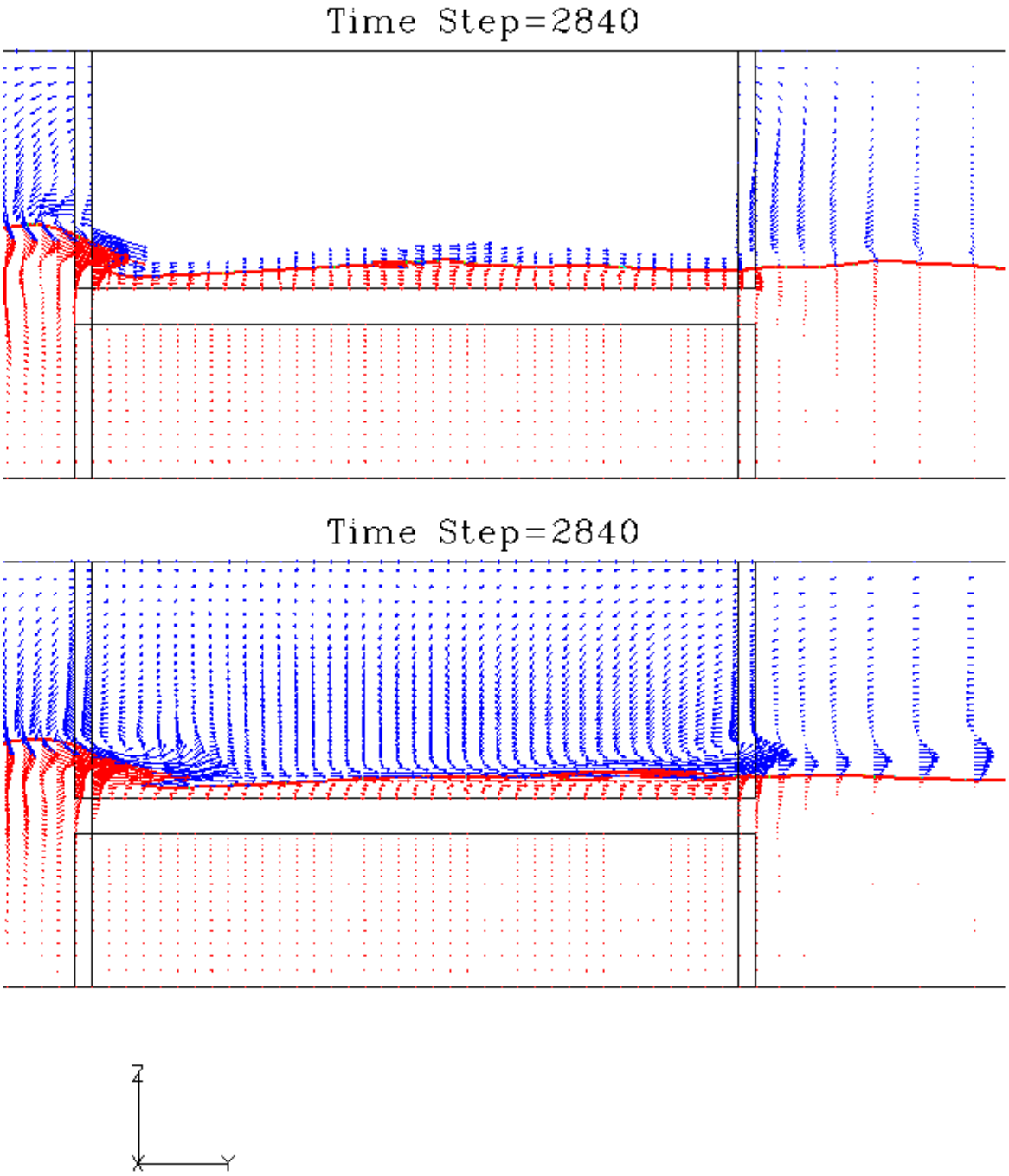

(a)

Figure 4.15: Velocity field induced by the wave with and without velocity-extrapolation routine in position III

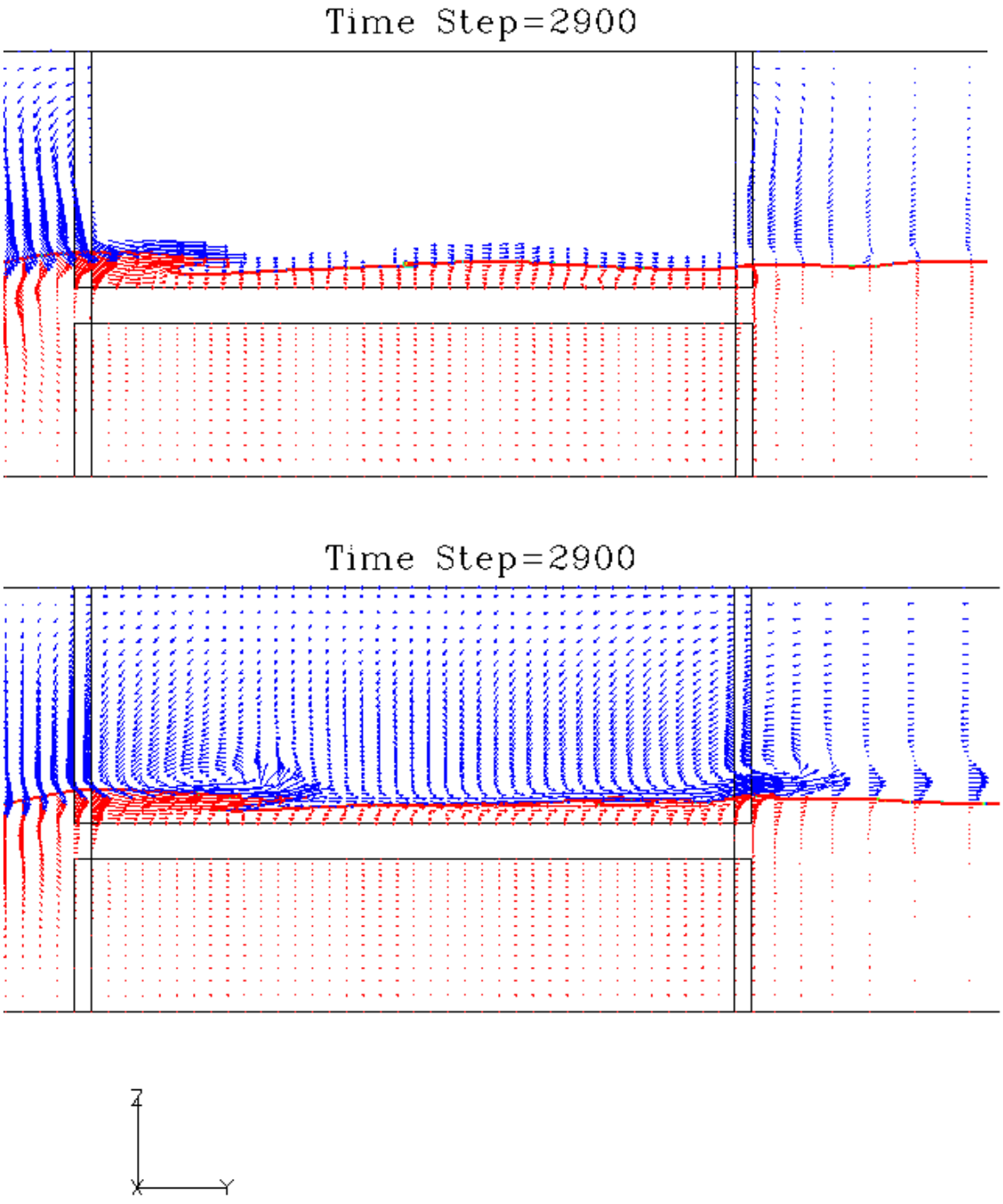

(b)

Figure 4.15: (Continued)

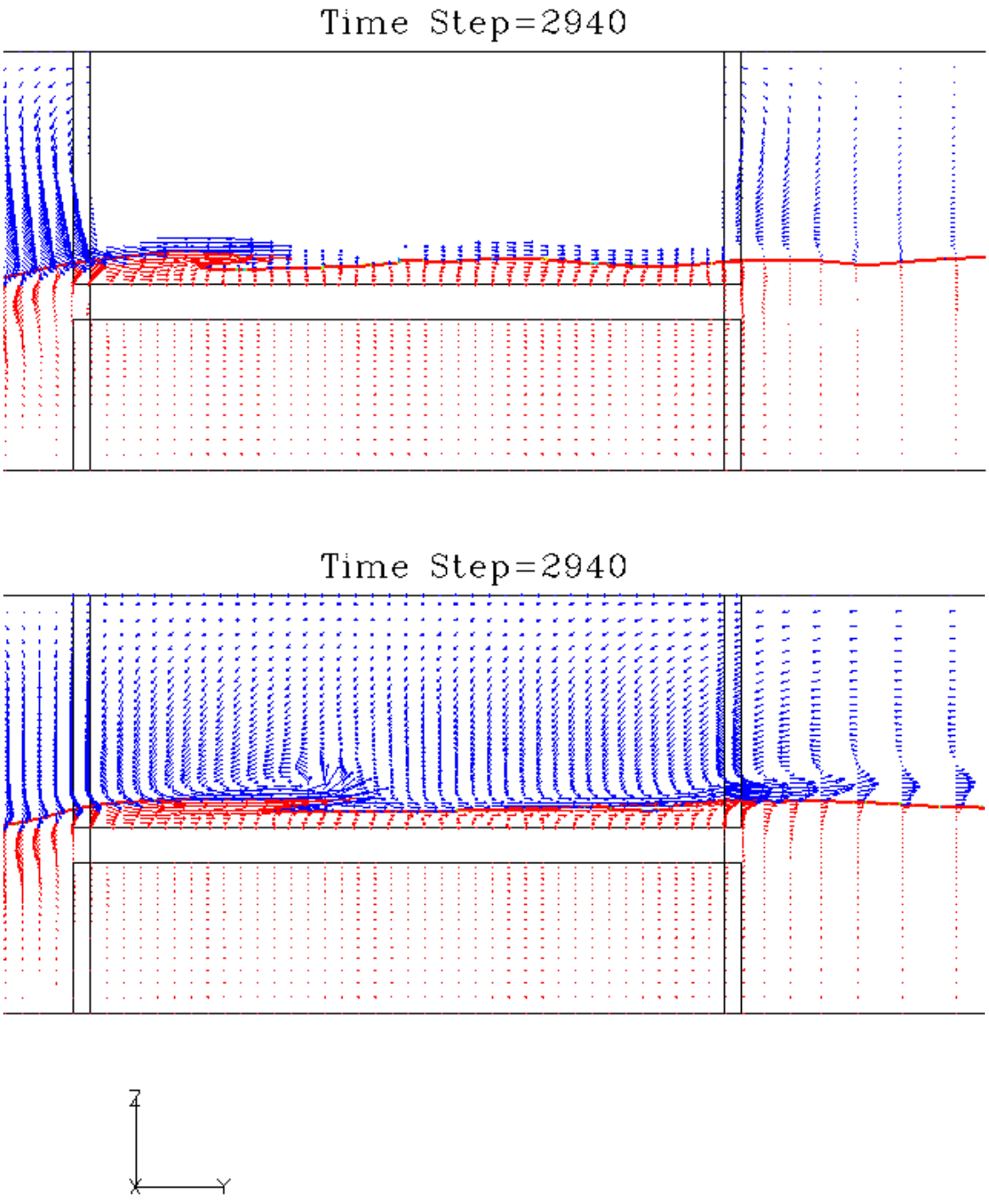

(c)

Figure 4.15: (Continued)

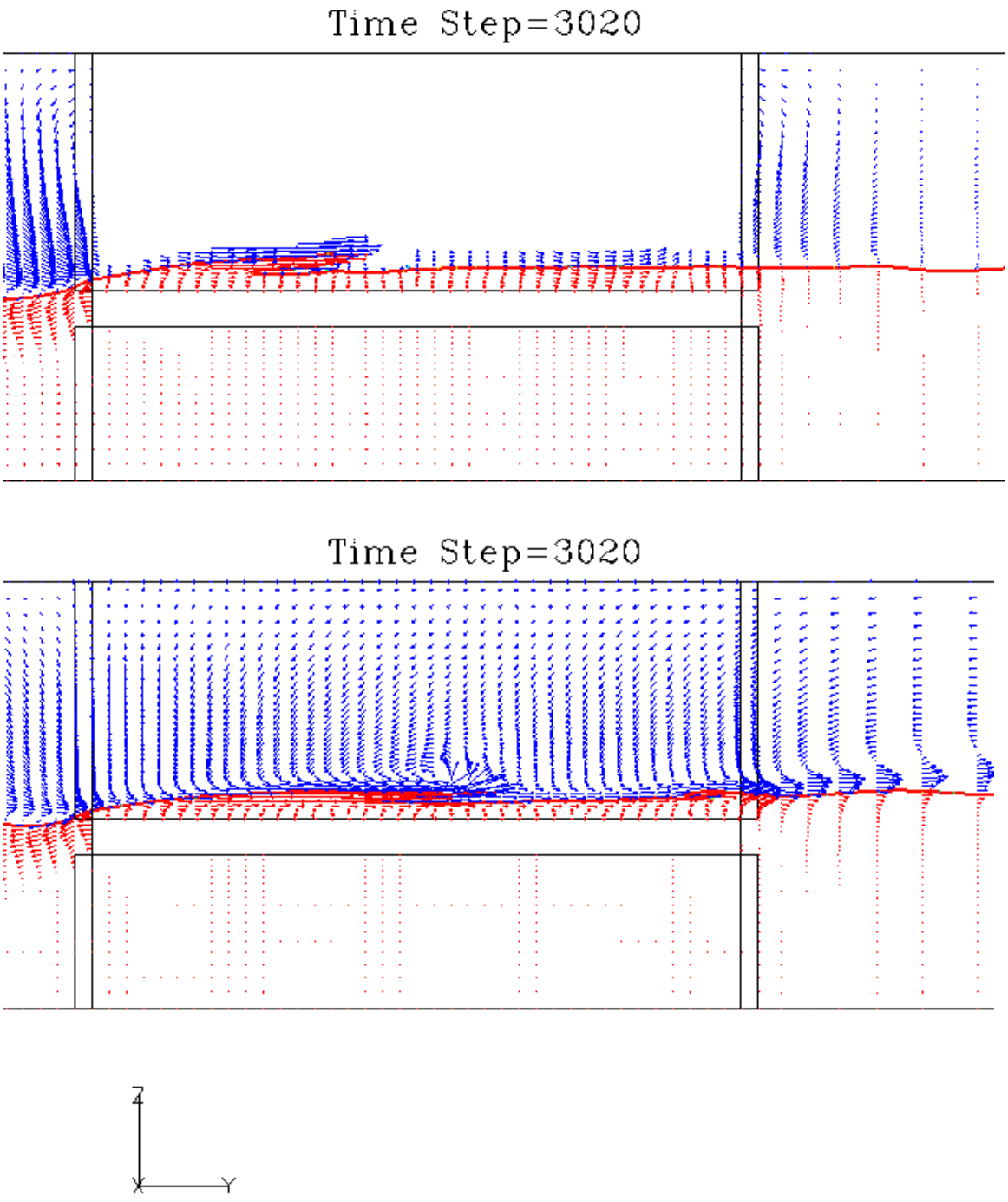

(d)

Figure 4.15: (Continued)

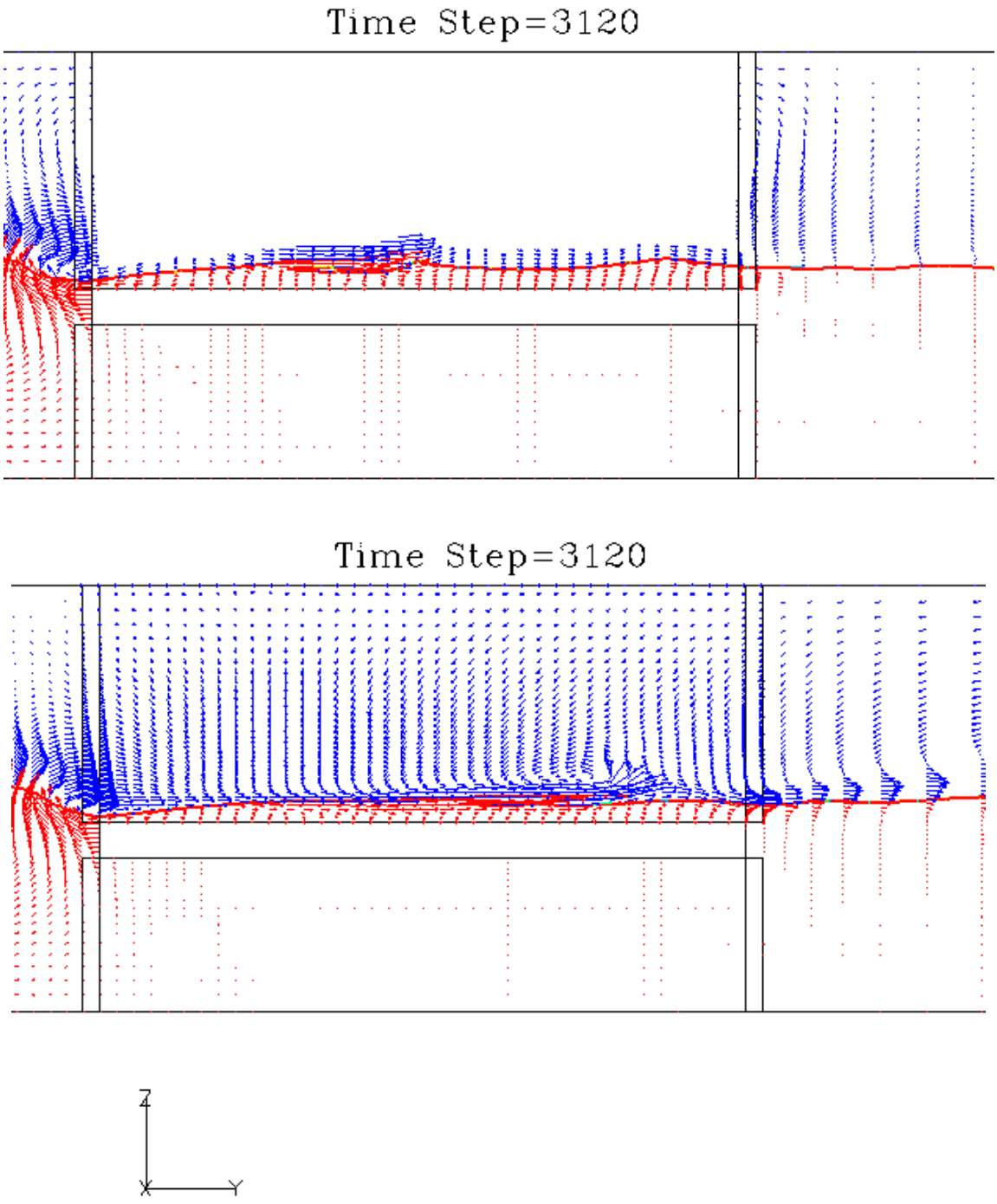

(e)

Figure 4.15: (Continued)

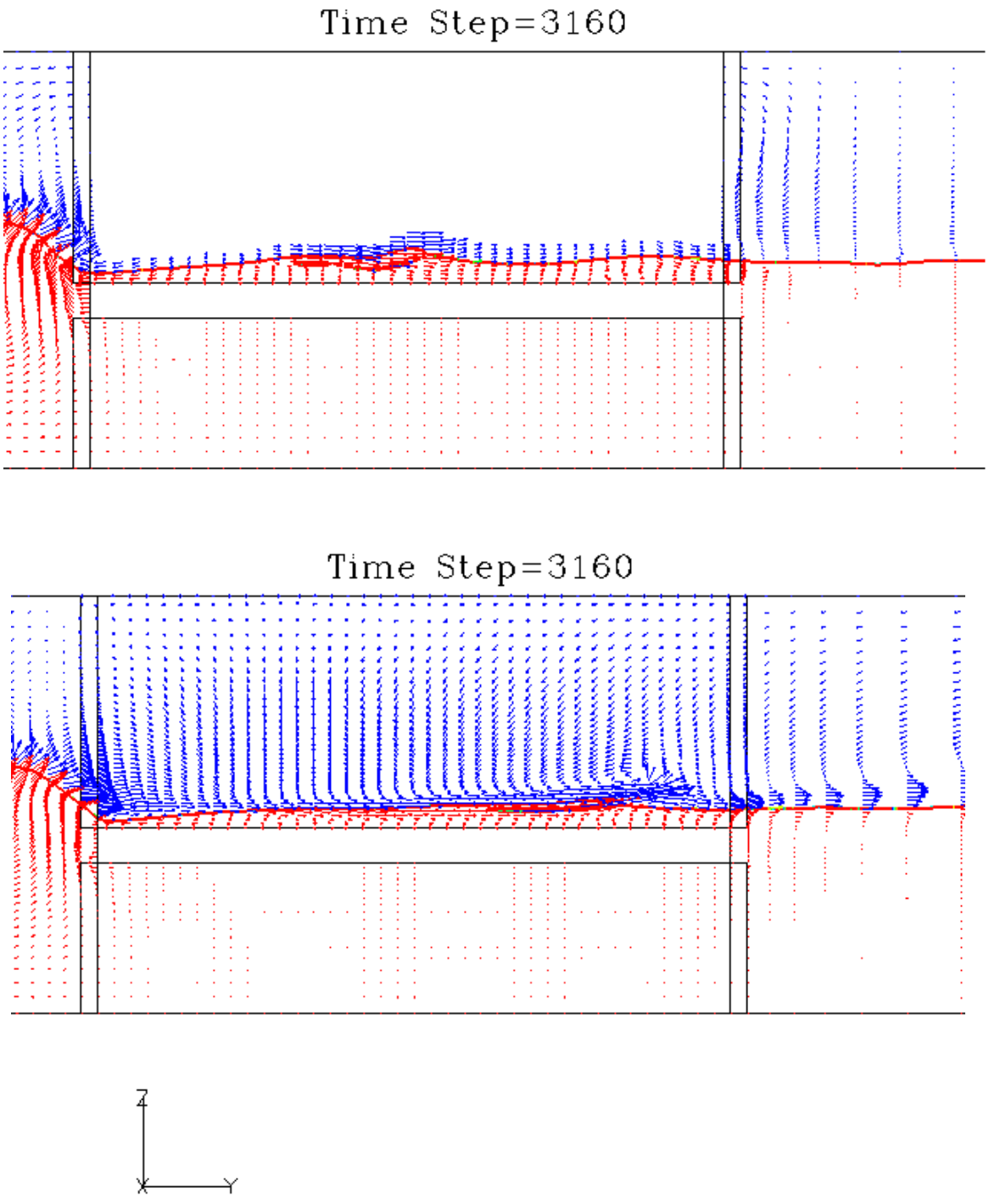

(f)

Figure 4.15: (Continued)

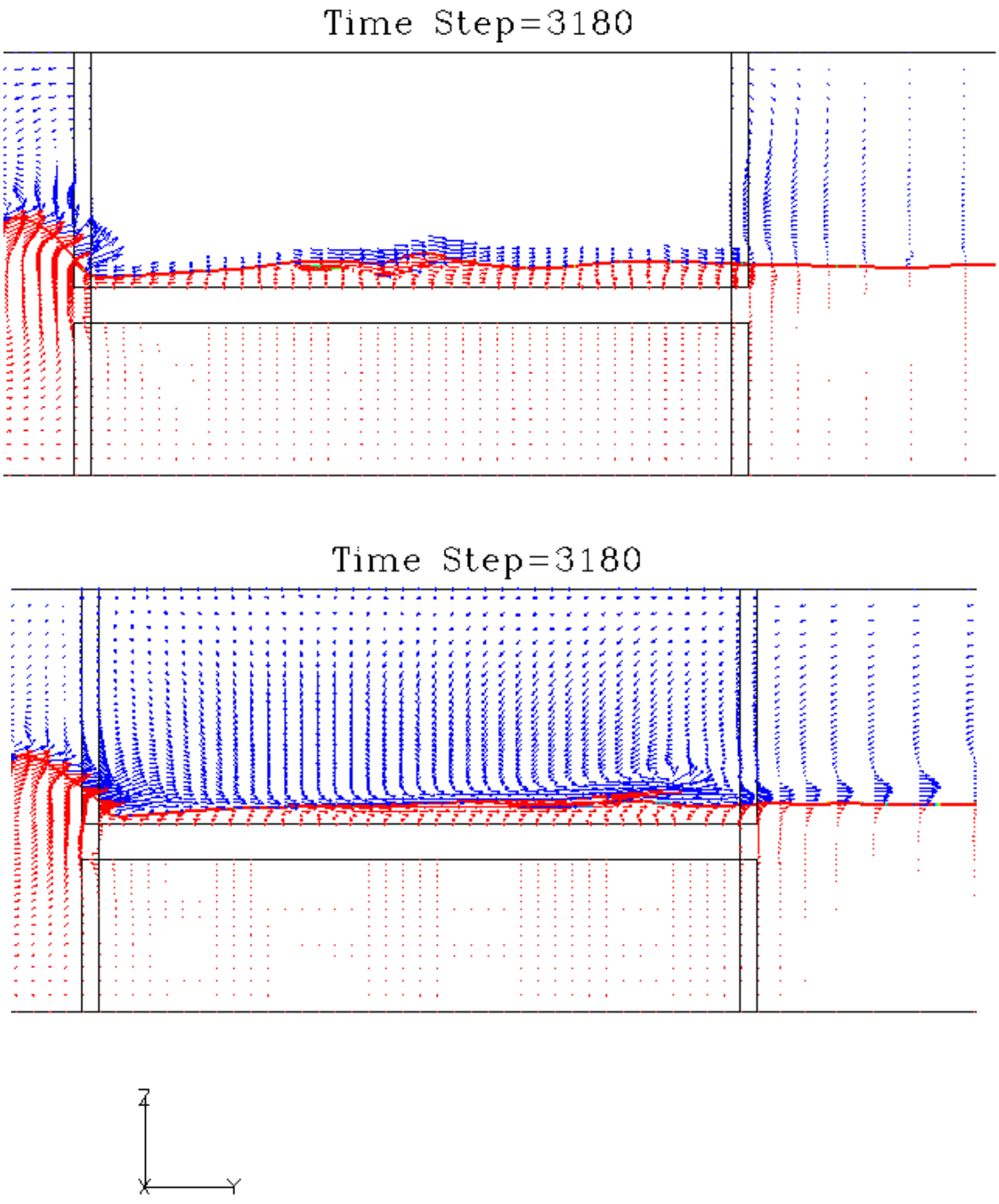

(g)

Figure 4.15: (Continued)

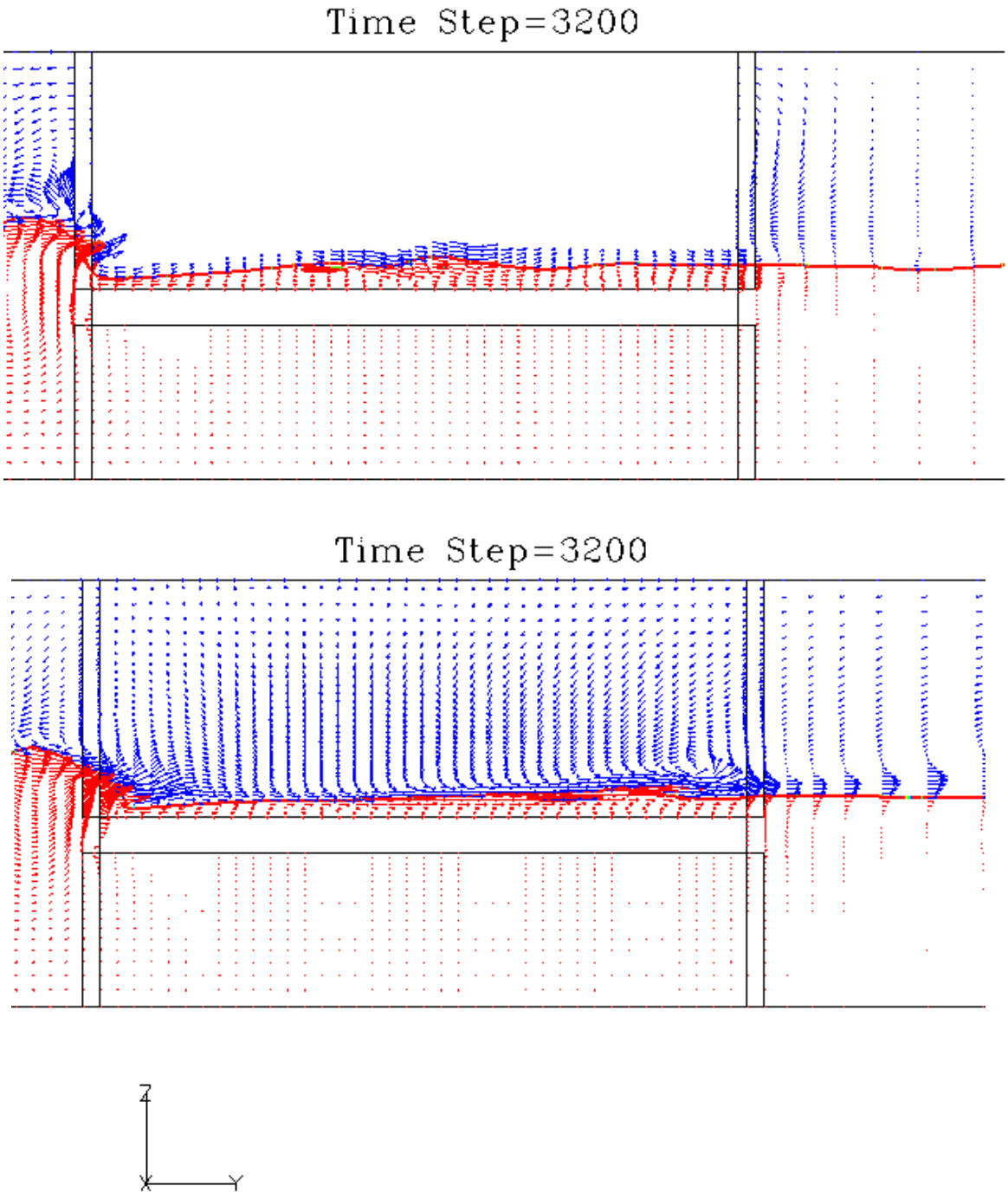

(h)

Figure 4.15: (Continued)

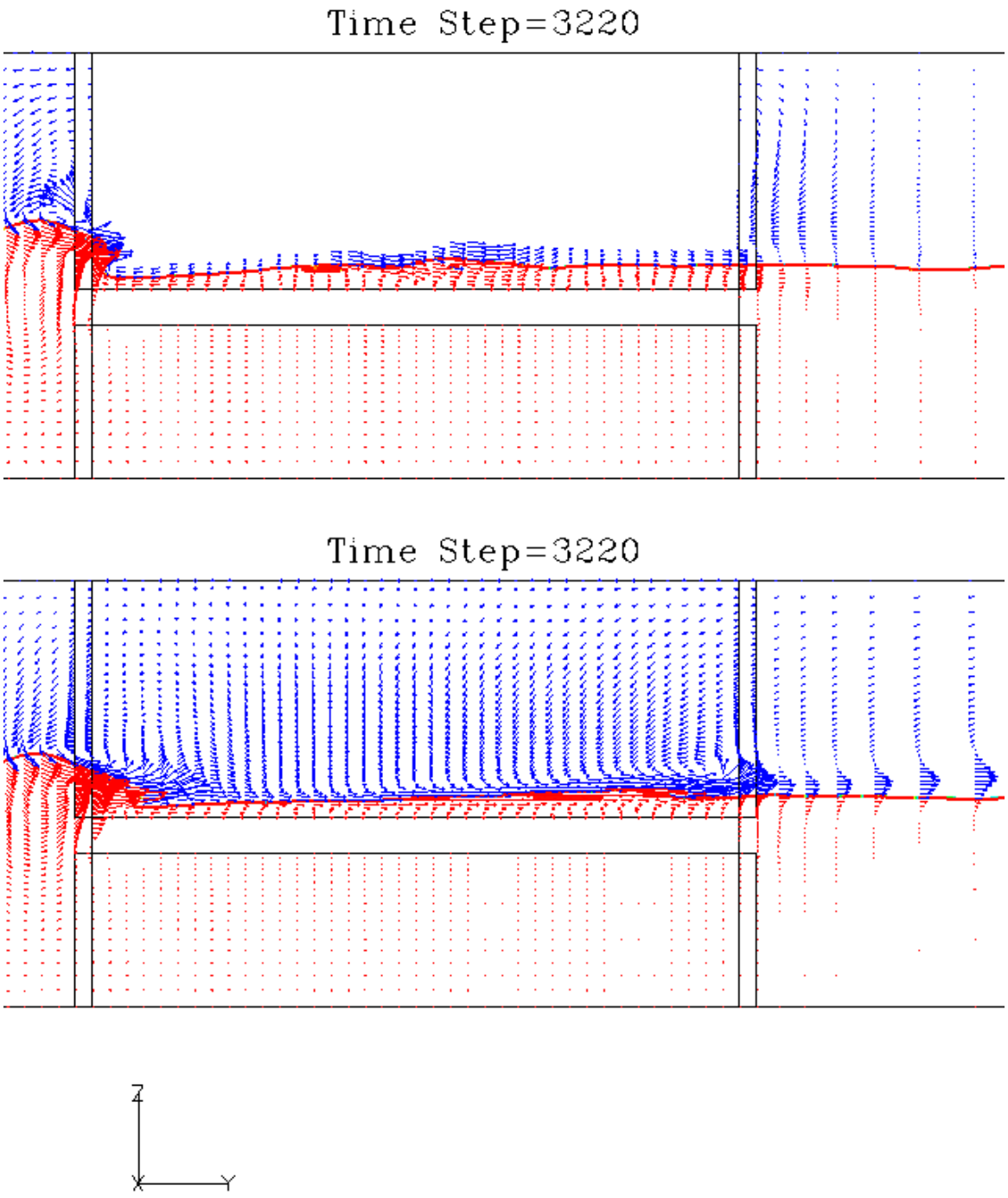

(i)

Figure 4.15: (Continued)

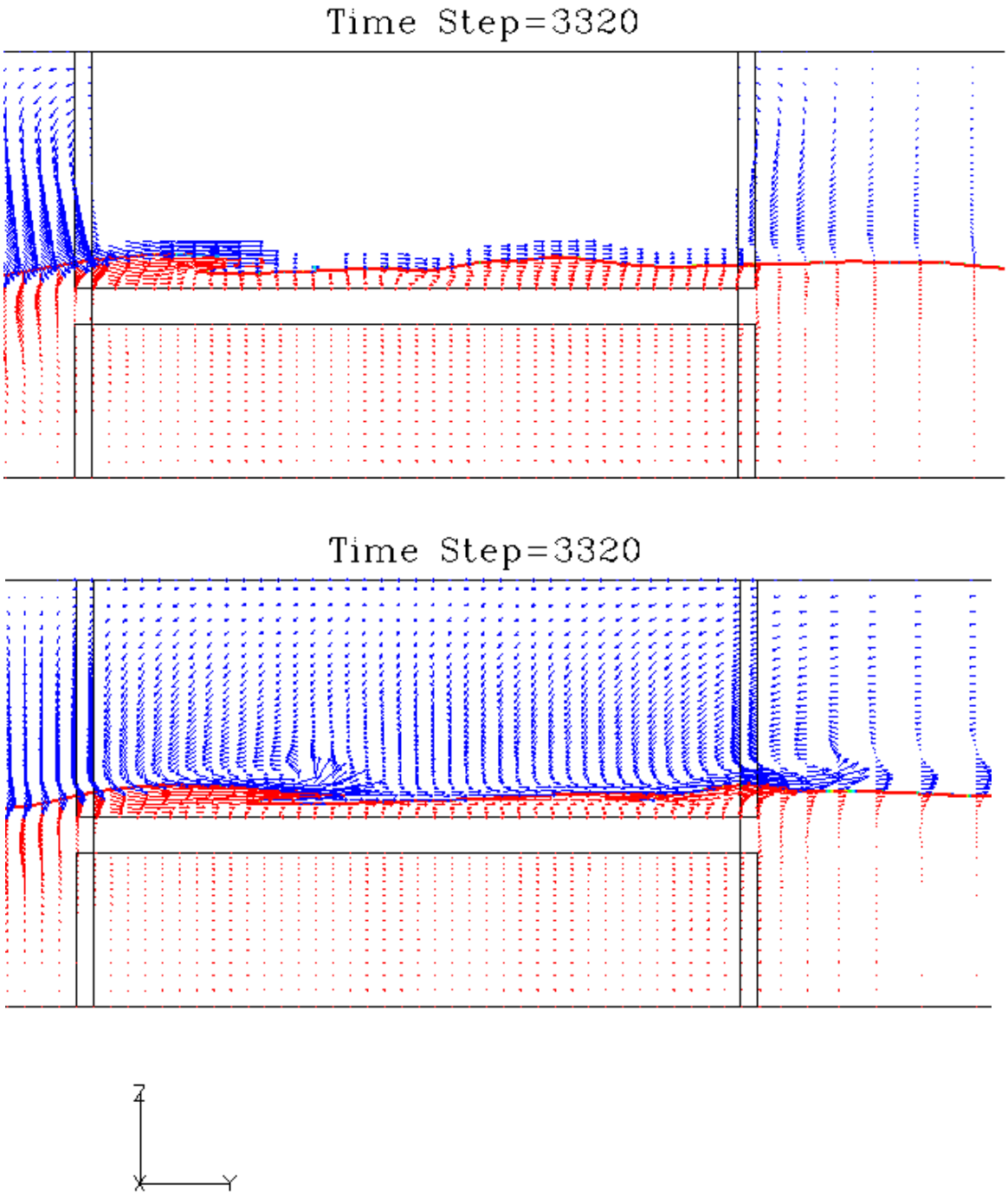

(j)

Figure 4.15: (Continued)

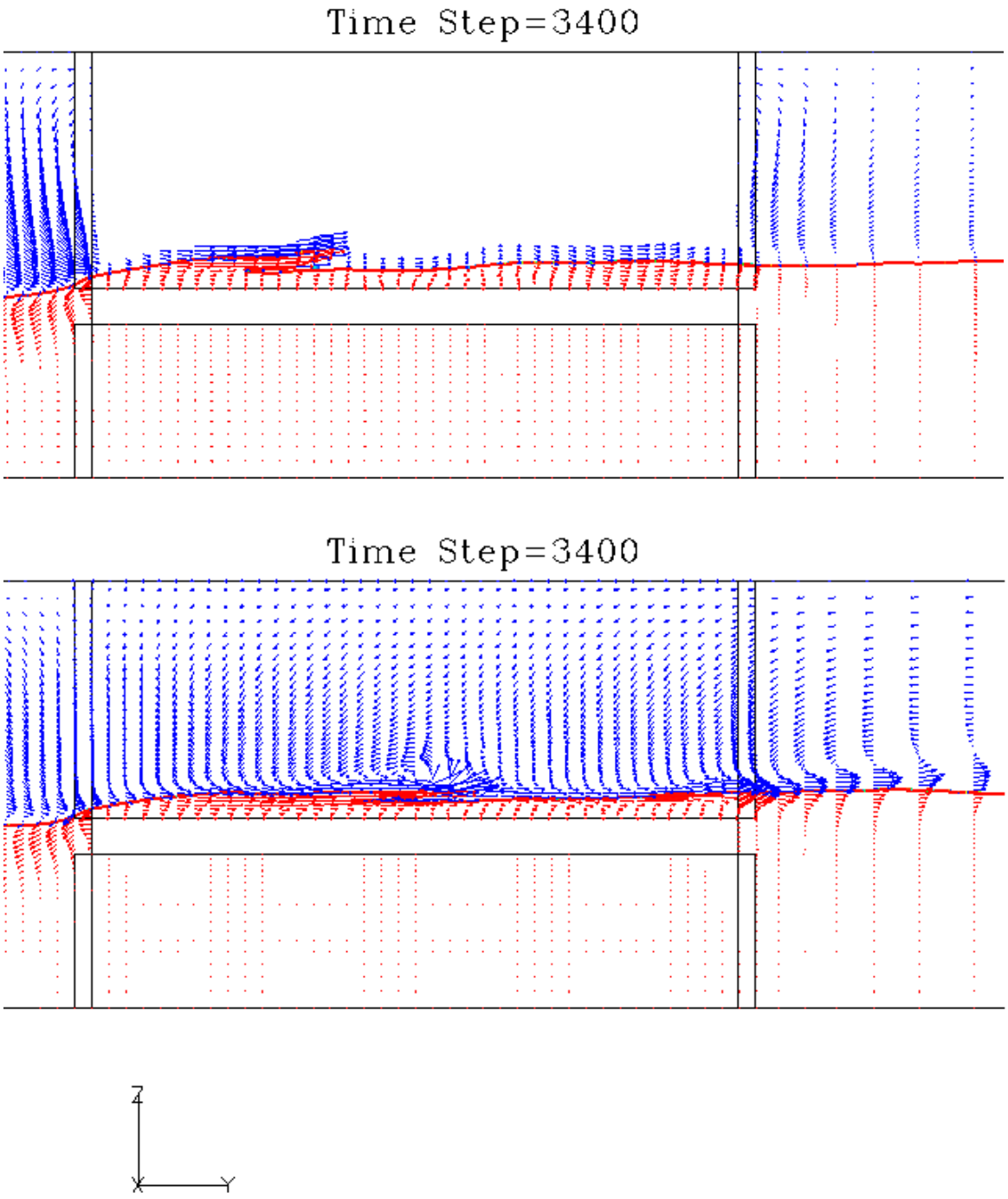

(k)

Figure 4.15: (Continued)

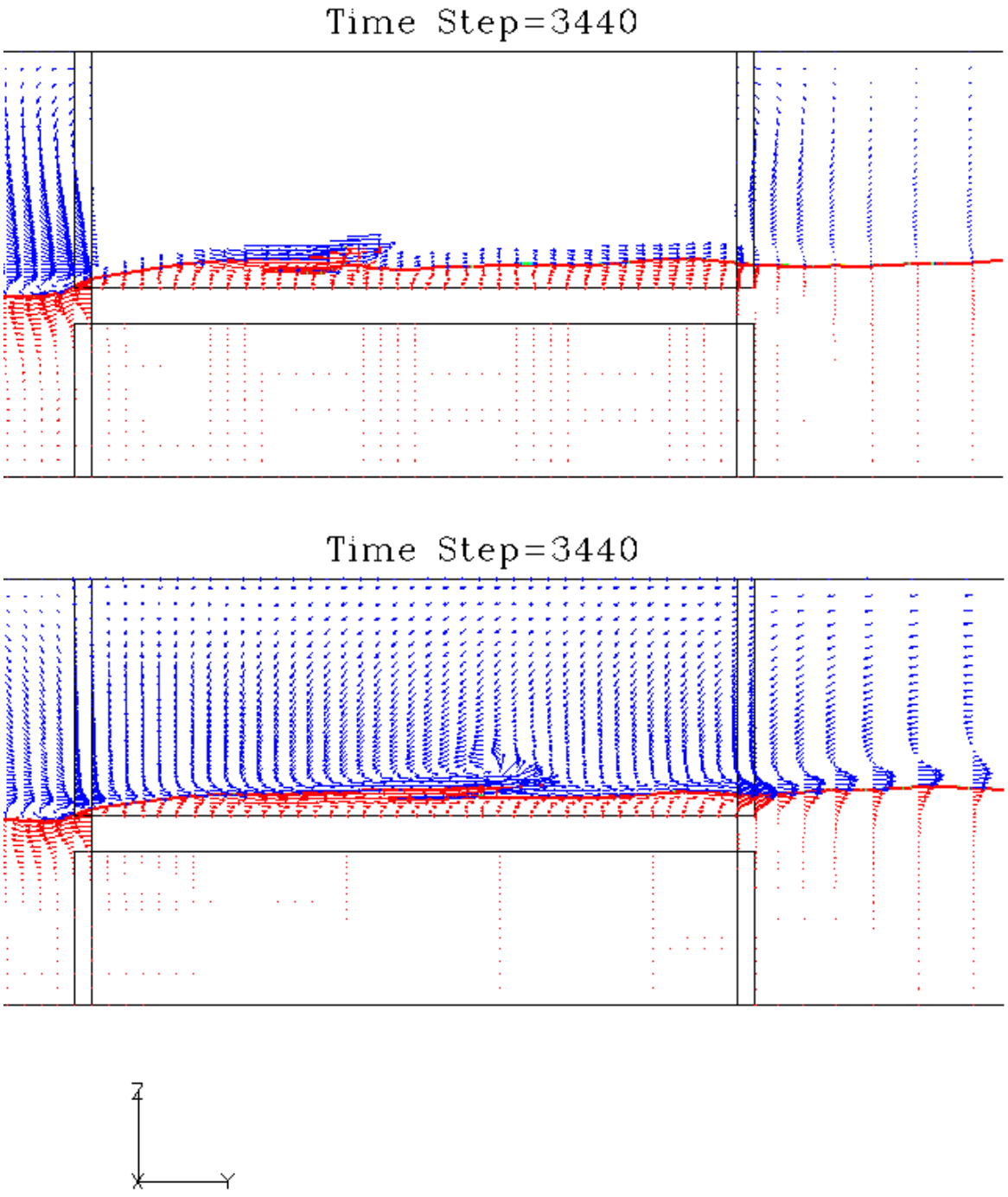

(l)

Figure 4.15: (Continued)

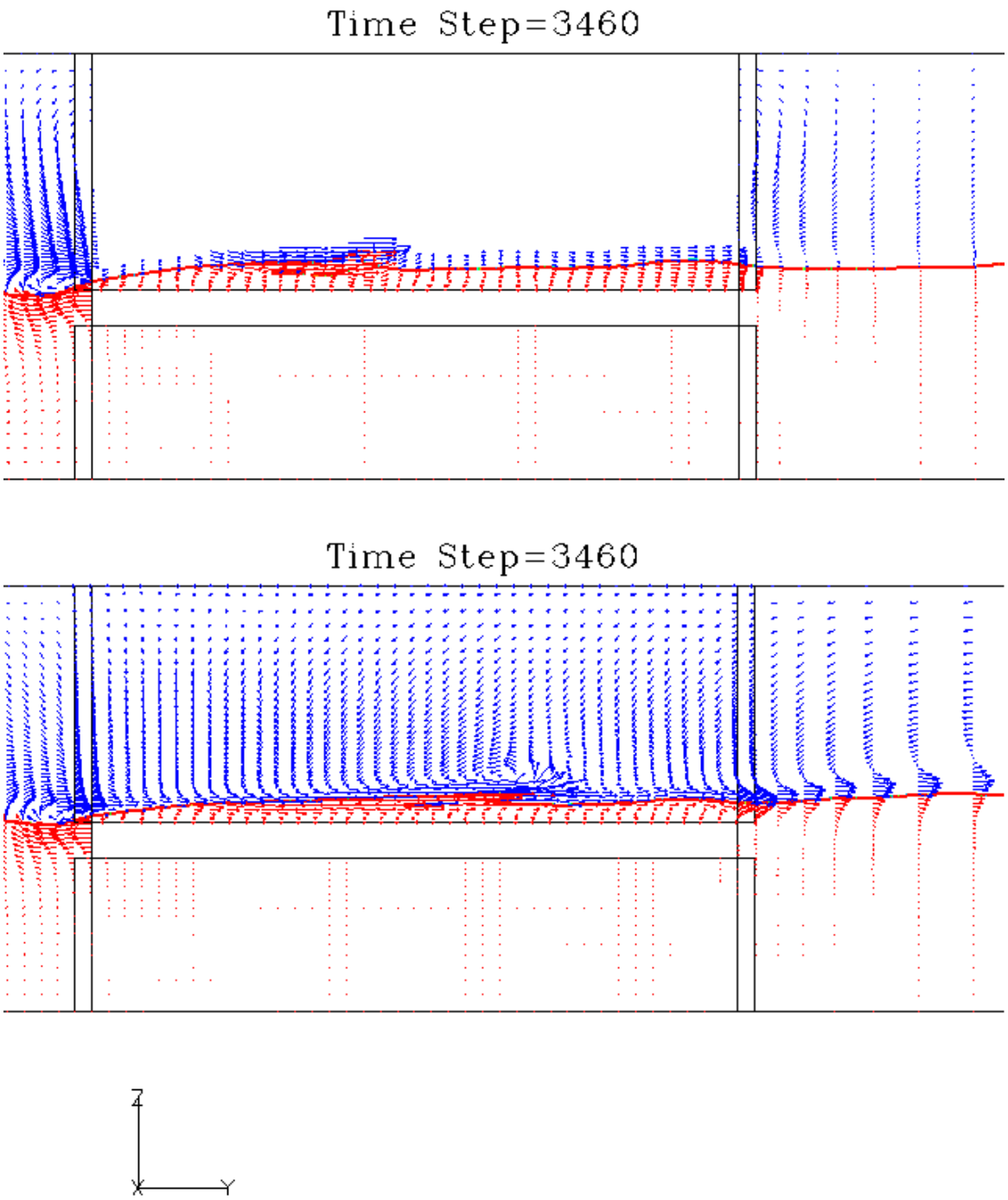

(m)

Figure 4.15: (Continued)

Figure 4.15 shows the comparison of results with and without velocity-extrapolation routine. In every plot, the former one is the result introduced velocity-extrapolation; and the latter one is the result void of velocity-extrapolation. The obvious difference in these two results is: by applying velocity-extrapolation, the air velocity field is narrowed to close the free surface above the platform deck. And due to the first order in the velocity-extrapolation scheme, the lanes of air velocity field at the same horizontal position have the same magnitude and same direction.

The series plots from (a) to (n) present the process of two successive wave passing over the deck and the waves are transformed into breaking waves. The breaking wave process consists of three regions: a pre-breaking region, an outer region (or transition region) and an inner region (or quasi-steady state region).

In the pre-breaking region, the wave becomes asymmetric, the wave top overturns and a forward-directed jet is formed. From the plot (a) to (e), the wave crest reaches the deck and the regular wave shape is distorted. The velocity of crest top is much larger than that under the crest. Thus, the wave top will surpass the wave bottom and forms a water jet with quite large velocity. No matter using the velocity-extrapolation routine or not, the first stage, pre-breaking region, can be simulated throughout.

In addition, at the breakpoint, here defines as the point where the tip of the jet falls at the forward face of the wave, the so-called outer region starts. In this region, with a horizontal extent equal to several water depths at the breakpoint, rapid transformations take place in the part of the wave above the level of the wave trough. From plot (f) and

plot (g), we can find that the velocity-extrapolation can assist constructing this process proven by the results that the front of breaking wave falls to the forward free surface. To the contrary, without the assistance of velocity-extrapolation, the jet formed by overturning wave will continue flying forward. This certainly contradicts with the observation in the laboratory experiment.

Lastly, due to the high rates of shear the rapid transformations diminish in strength and the wave enters the quasi-steady state region where changes in wave motion take place more gradually. The plot (h) and plot (i) can show this process after the wave is overturned. This process finally makes the breaking wave merged into the front free surface and propagating to the downstream.

From plot (j) to plot (n) show another breaking wave transformation process. The three regions can also be distinguished if the velocity-extrapolation is applied. All in all, the velocity-extrapolation routine is crucial to making breaking wave and it is valuable to utilize by sacrificing some wave decay. Back to figure 4.9, we study this comparison again. In this figure from (a) to (d), using the velocity-extrapolation, the further the gage away from the wave maker, the worse the wave decay is. In plot (d), the distance away from the wave maker is about more than one wavelength which is also approximately equal to the deck length in present case. At this point, the decay ratio is about 10%. That means, even we apply the velocity-extrapolation routine, the wave decay is not as serious as we image. In addition, we can do some measures to repair this flaw by generating finer grid or using shorter time increment. Considering the importance of

velocity-extrapolation in make breaking wave and not the big effect for the wave propagation, we continue using it to simulate the breaking wave around the platform.

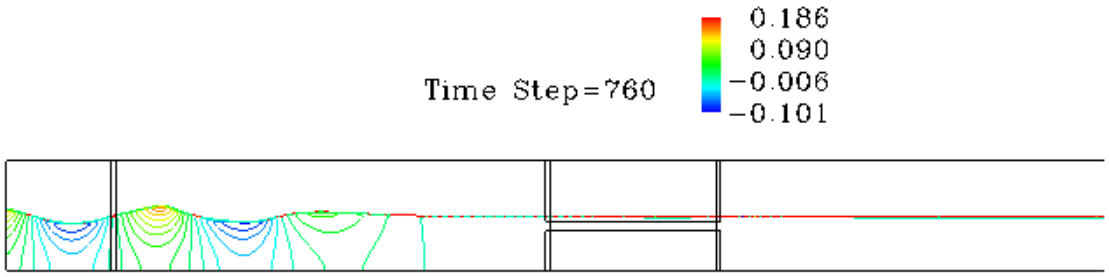

(a)

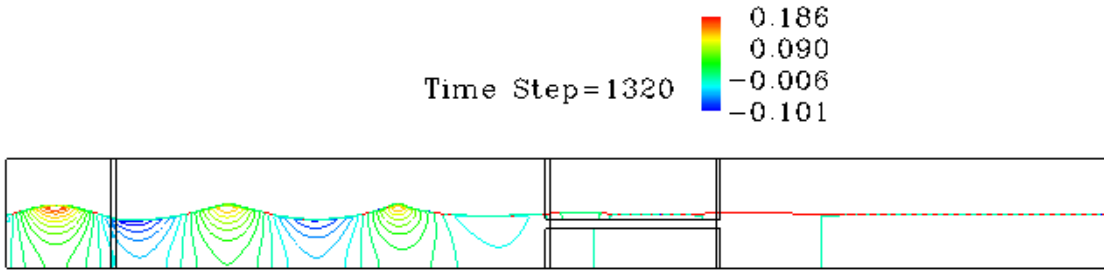

(b)

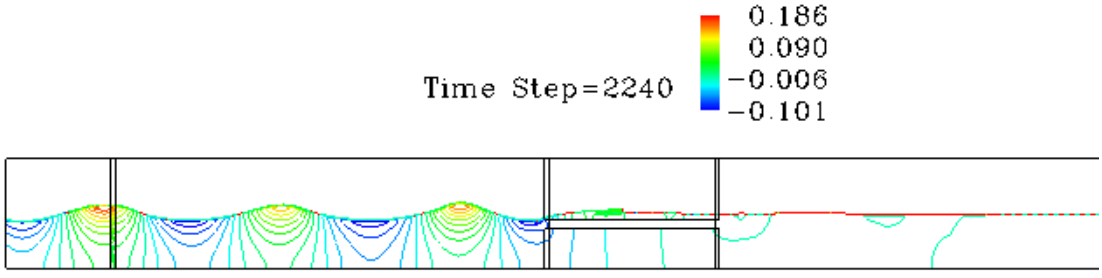

(c)

Figure 4.16: Evolution of wave and dynamics contour in position III

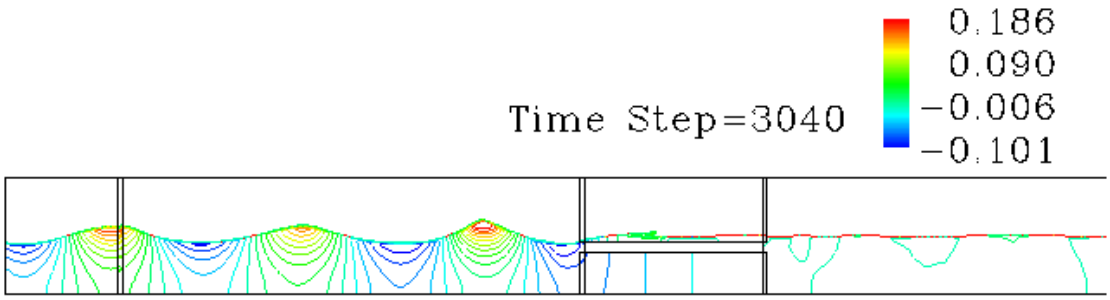

(d)

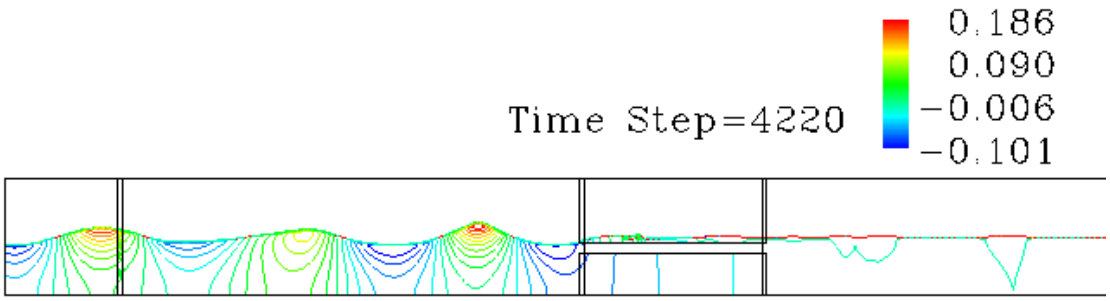

(e)

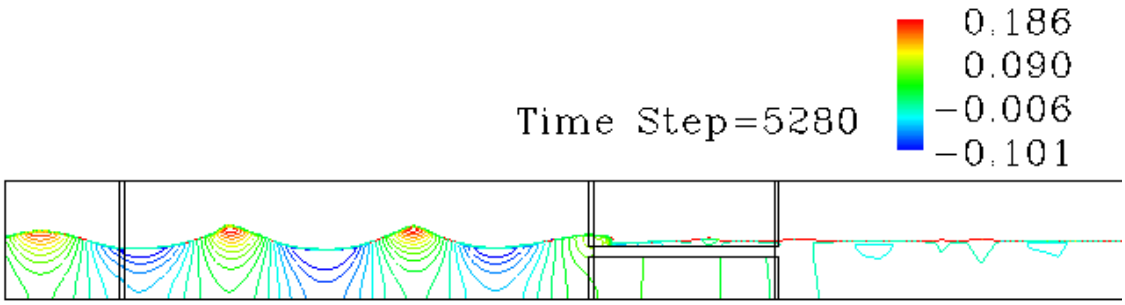

(f)

Figure 4.16: (Continued)

Figure 4.16 is about the evolution of wave and dynamic pressure contour under the platform at different times. First of all, the dynamics contour can be maintained in the similar pattern before reach the deck and this kind of pattern is coincide with that in the linear wave in first block. As the wave reaches the deck, the dynamic pressure contour pattern is disrupted: above the deck, the dynamic the dynamic is distributed over the distorted breaking wave shape, and from the color-map, the value is relatively smaller than that in previous wave crest region; under the deck, the dynamic pressure seems tiny. Back to figure 4.15, let us observe the velocity field over the platform. Above the deck, the velocity values are some larger than that before reaching the deck. And neighboring the free surface, the velocity is greater than that neighboring the deck. That is the reason that the top of wave can catch and surpass the front wave surface. Besides, the velocity field below the deck is also insignificant just like velocity field in the still water.

In conclusion, the platform deck can separate the pressure contour and velocity field distinctly. Above the deck, the wave properties including velocity and dynamic pressure are similar with those in shallow water; below the deck, the field of velocity and dynamic pressure contour are as small as those in still water.

4.4.4. Position IV

When the deck height is continuously decaying to some height, we can find the similar phenomena like that in the Position III, but the breaking wave phenomena will be degraded.

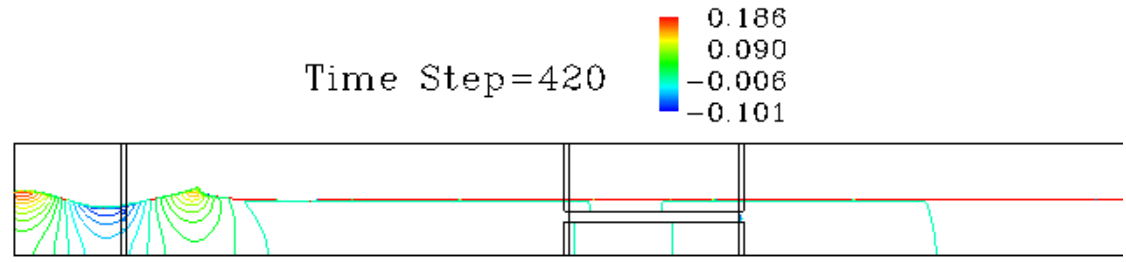

(a)

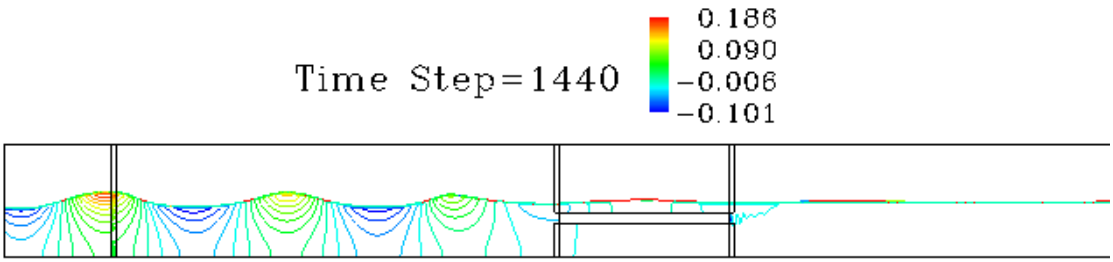

(b)

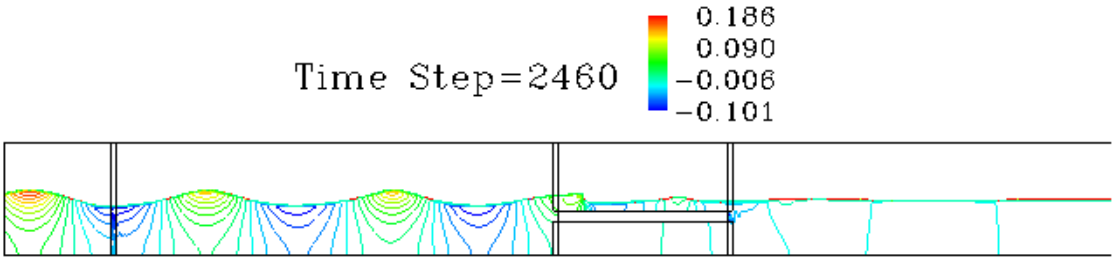

(c)

Figure 4.17: Evolution of wave and dynamics contour in position IV

In figure 4.17, the pressure contour is changed by the standing platform deck as same as shown in figure 4.15. It is needless to repeat explaining the reason.

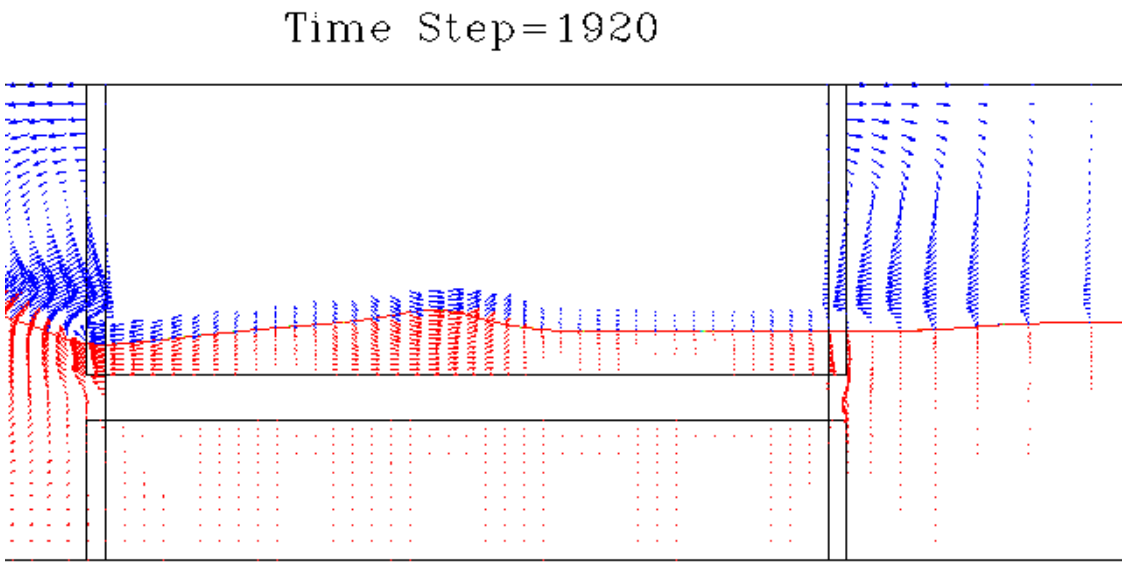

(a)

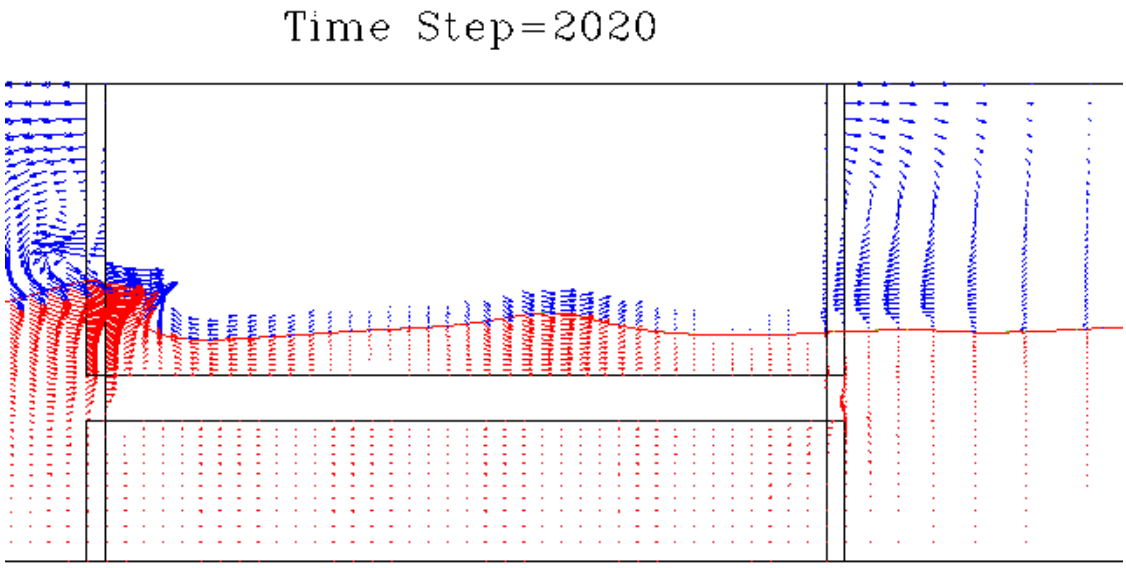

(b)

Figure 4.18: Velocity field induced by the wave in position IV

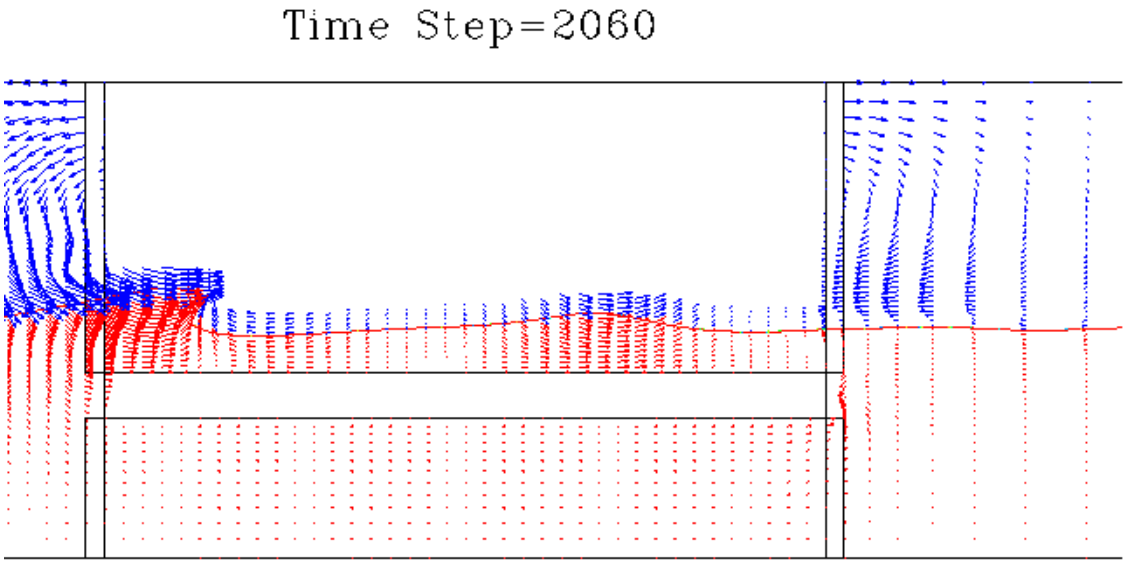

(c)

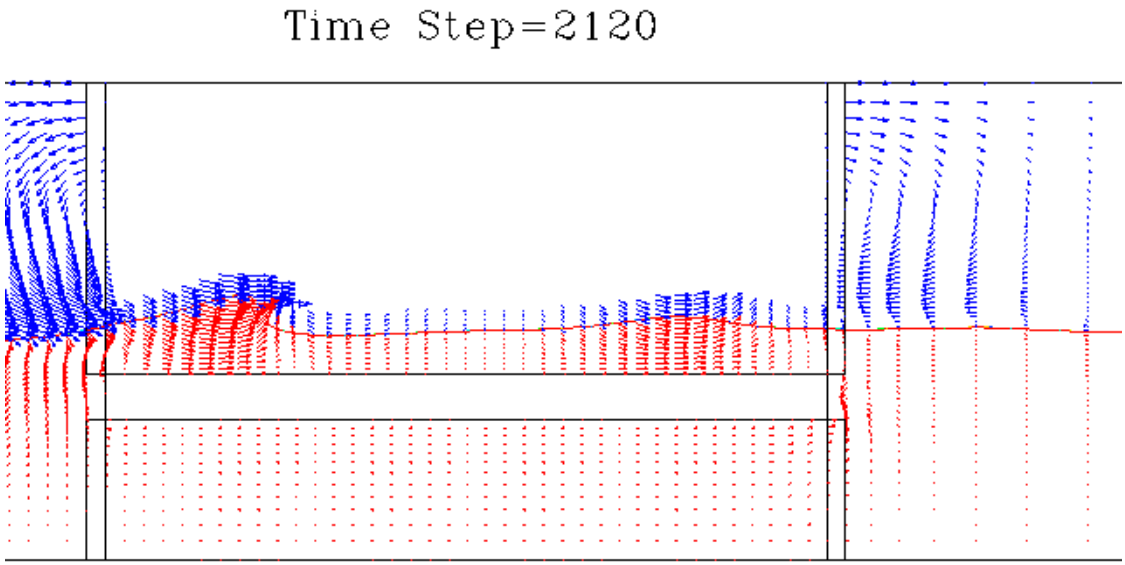

(d)

Figure 4.18: (Continued)

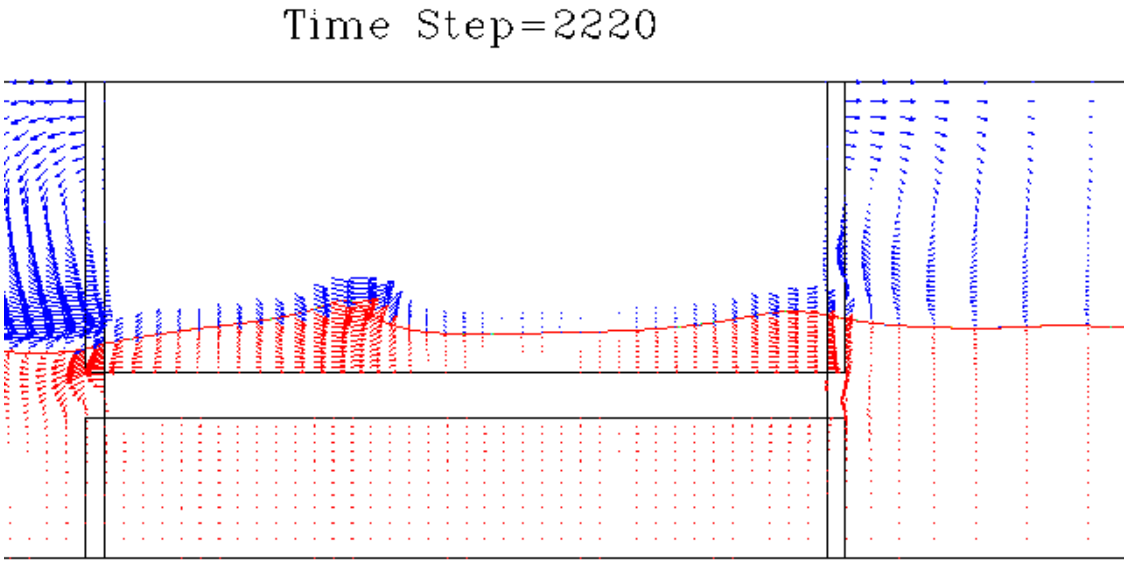

(e)

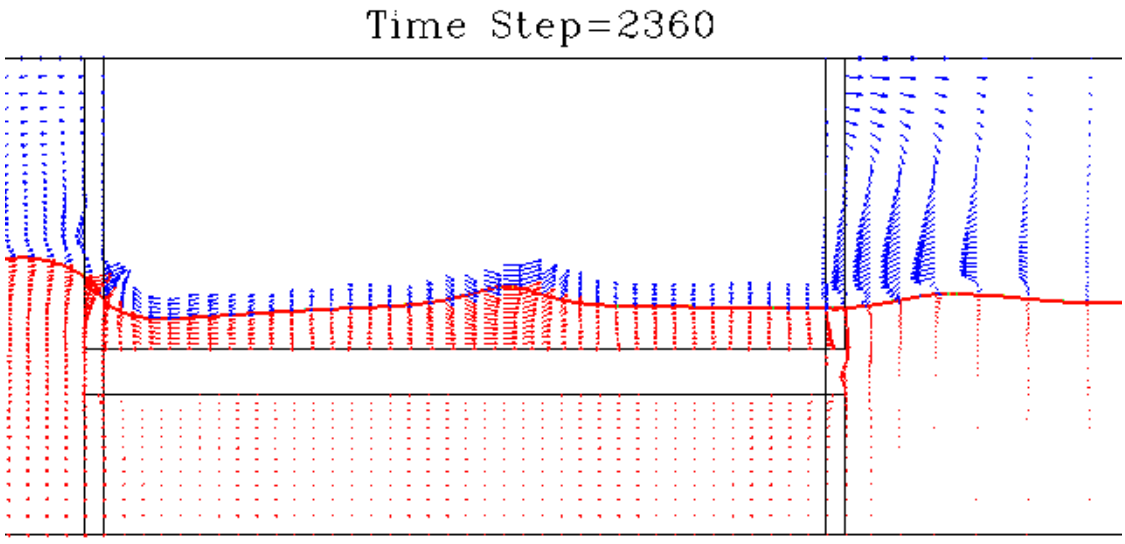

(f)

Figure 4.18: (Continued)

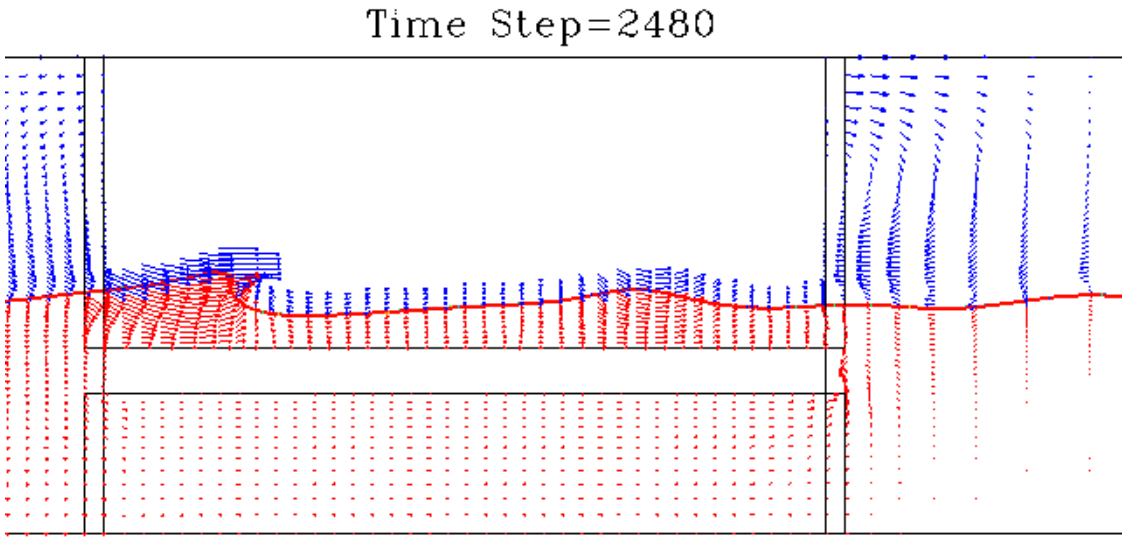

(g)

Figure 4.18: (Continued)

In figure 4.18, we can continue to analyze the breaking wave process step by step. First of all, from plot (a) to plot (d), the pre-breaking region is presented clearly that the top of wave is formed into asymmetric and forward-directed jet. From the trend of water jet, it seems that it will transit into the second stage, an outer region, after the tip of the jet is connected to the front free surface. However, from the plot (e) to (g), we can confirm that the second stage for breaking wave does not exist. The wave is rapidly transformed into the normal wave and continues propagation along the deck.

Observing the velocity field, we can find that at the same lane of horizontal position, the difference of velocity values is not large from the deck to free surface. It can explain that the top of the wave crest hardly surpasses the water particles on bottom and climb to the front water surface. To the contrary, in figure 4.15, the velocity

neighboring the free surface is much greater than that neighboring the deck, which can create the overturning wave phenomenon without effort.

The comparison of Position VI and Position III, we can conclude that the deck position plays the important role in creating the breaking wave. As the deck is closely to the mean water level, the velocity closely to the free surface will become quite larger compared with that close to the deck. And the breaking wave will happen just like shown in figure 4.15. As the deck is at some deep position, the effect of the structure for the wave is decaying and the deck only produces the pre-breaking wave process. In essence, the happening of green water is due to the velocity difference neighboring between interface and the deck. When the deck is close to the mean water level, the water particles, located same height with the deck, will hit the side of deck and move upward to the above deck. Then, those particles merge into the water above deck and make the velocity nearby the surface larger. Lastly, it is easy to create the over-turning wave. To the contrary, if the deck is standing some deeper, the water particles as same high as the deck have not sufficiently velocity and thus they hardly make contribution for the velocity field nearby the surface. That is why in this situation the breaking wave cannot happen.

4.4.5. Position V

In last case, the deck is placed near the water bottom.

(a)

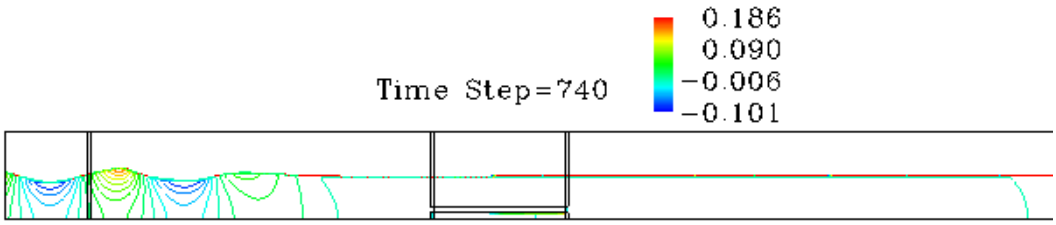

(b)

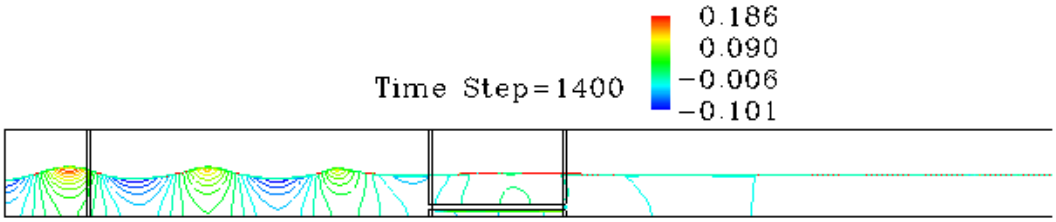

(c)

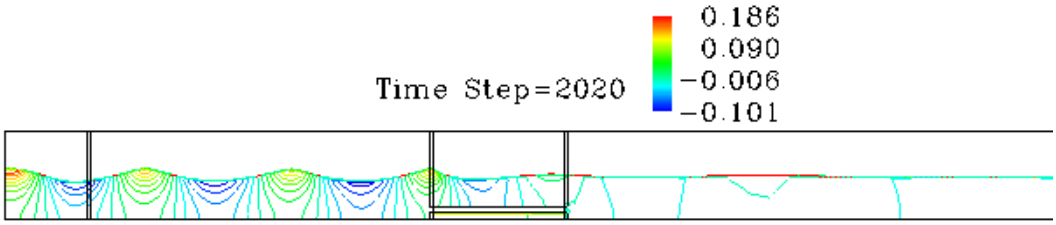

(d)

Figure 4.19: Evolution of wave and dynamics contour in position V

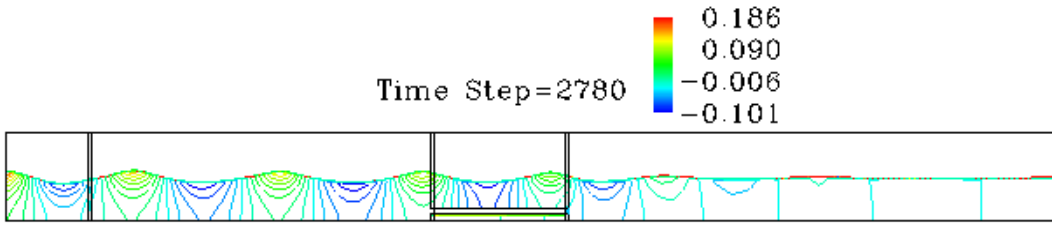

(e)

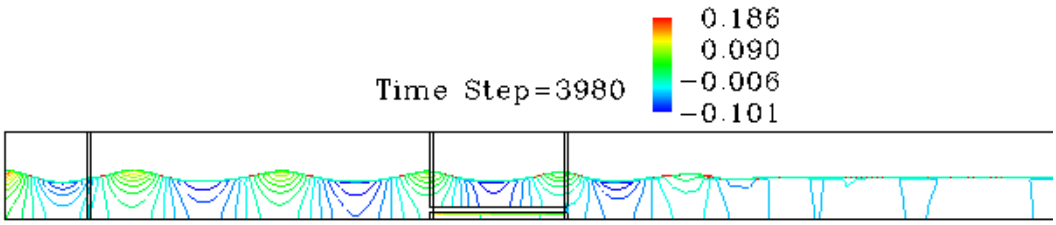

(f)

Figure 4.19: (Continued)

From figure 4.19, we can get the observation that the pressure contour is passing through the deck. Above the deck, the pressure contour can keep the pattern which is coincidence with that in tank 1. The pressure contour pattern is not disrupted by the structure, which is quite different from in previous cases. It further proves that the deeper the deck stands, the less effect the deck produces. In other perspective, due to the small dynamic pressure at the water bottom, thus the structure cannot affect the global dynamic pressure even the structure can influence the pressure contour around it at water bottom.

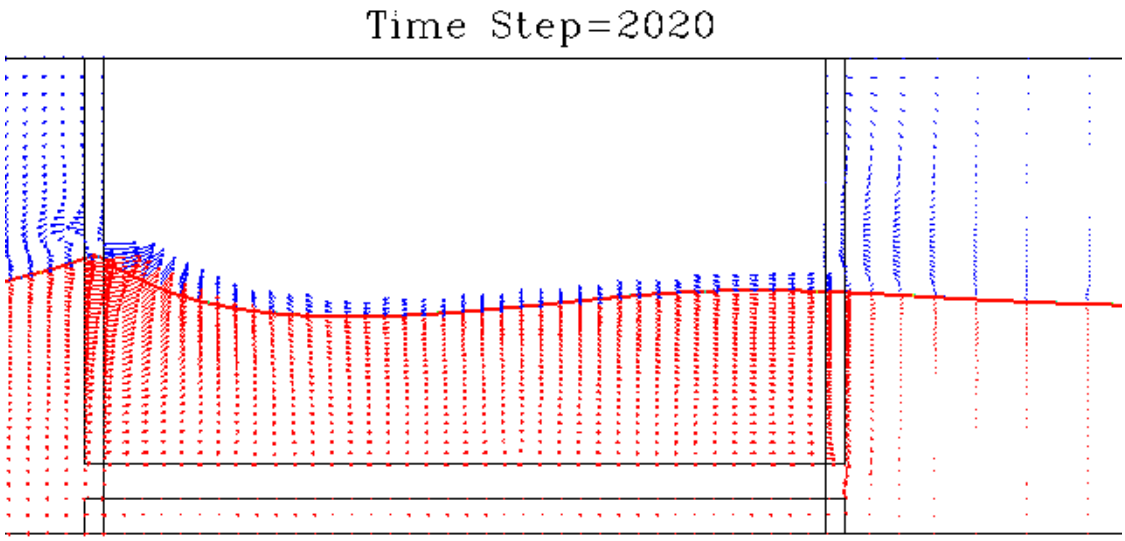

(a)

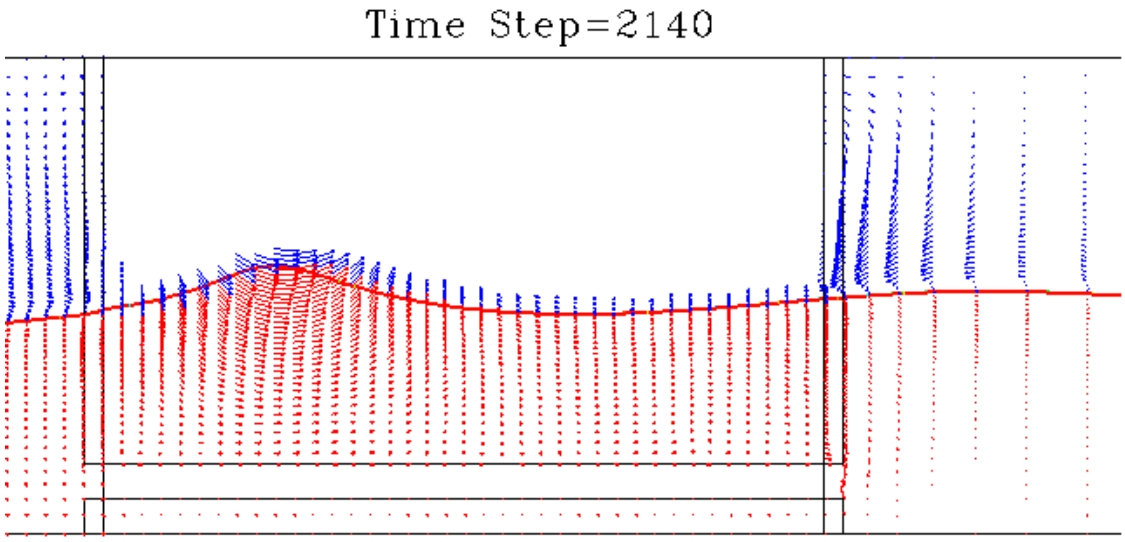

(b)

Figure 4.20: Velocity field induced by the wave in position V

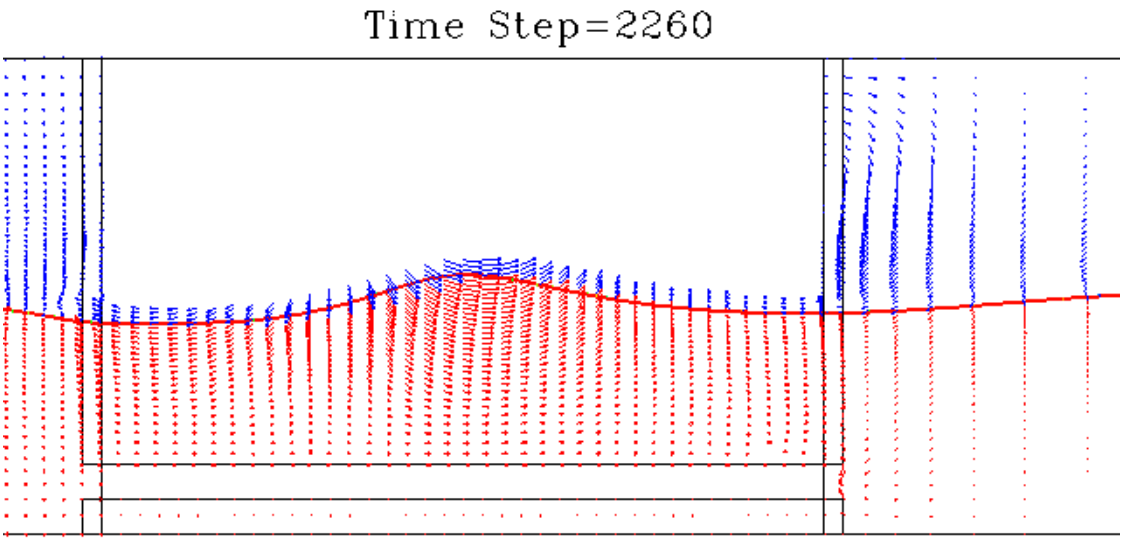

(c)

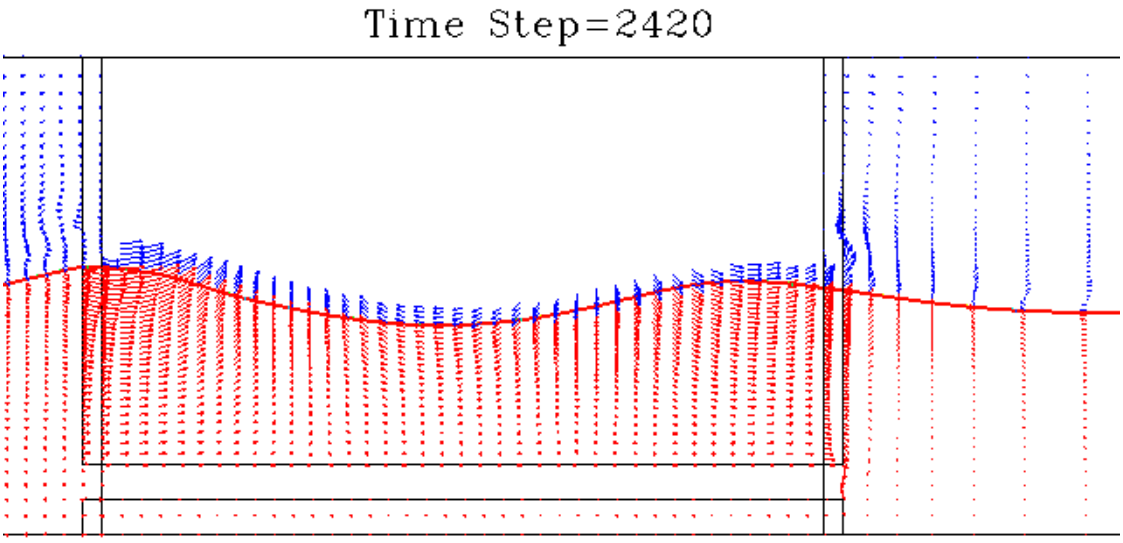

(d)

Figure 4.20: (Continued)

The figure 4.20 can give us a snapshot about the velocity field when the deck is falling close to the water bottom. In this situation, the velocity profile beyond the deck is quite similar with that of linear wave. There is no sensible breaking wave phenomenon due to the insignificant effect to the wave of the deck.

Combing these different deck height situations together, we can conclude that the deck height is playing an important role for the wave propagation over it. When the wave is propagating from the deep water to above the deck, it can be regarded as that the water depth is changed from deep water to the shallow water. Thus, some wave properties such as velocity, dynamic pressure are adjusted due to the adjustment of water depth. When the deck is placed close to the mean water level, the ultimately phenomena is that the breaking wave will happen. The breaking wave will surpass the front surface and then falling down to the surface due to gravity effect.

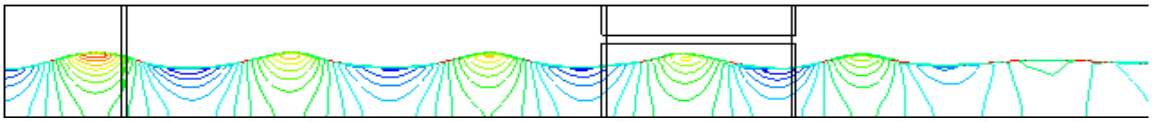

(a) Position I

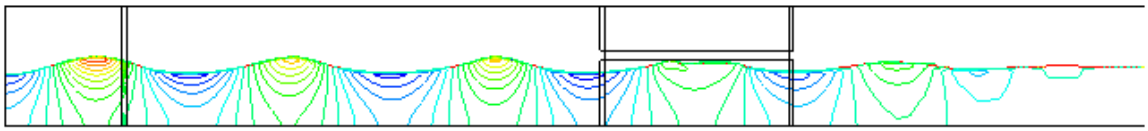

(b) Position II

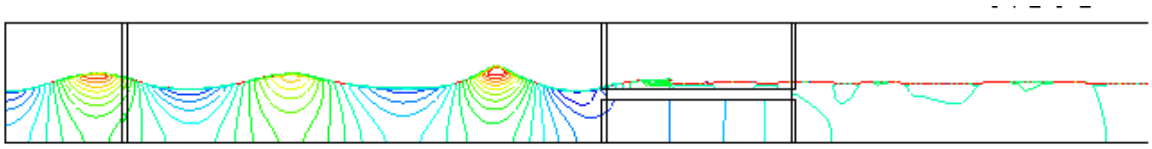

(c) Position III

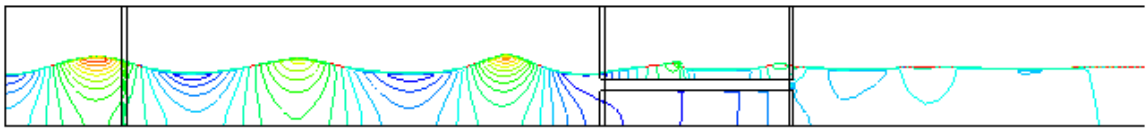

(d) Position IV

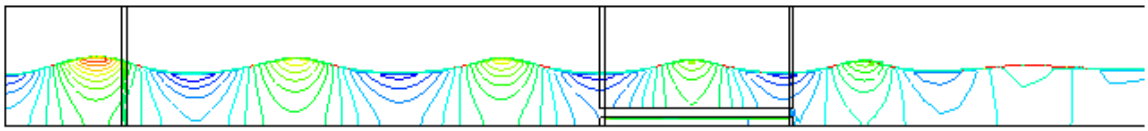

(e) Position V

Figure 4.21: The series of dynamic pressure contour in the five positions at the same time step

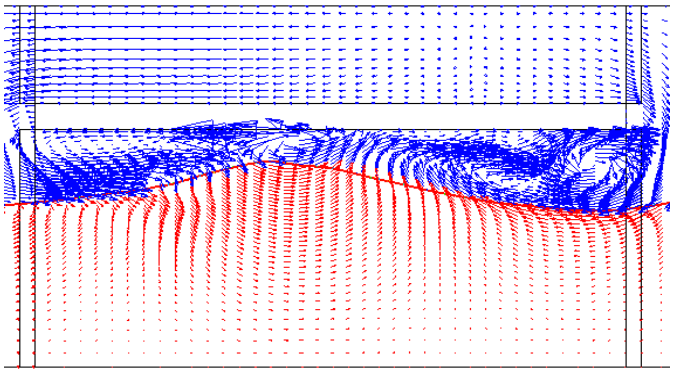

(a) Positon I

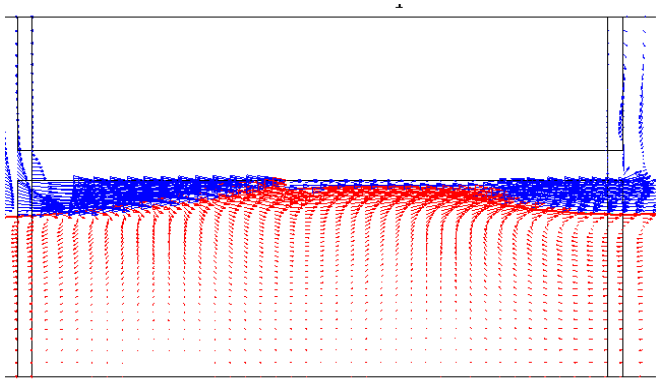

(b) Position II

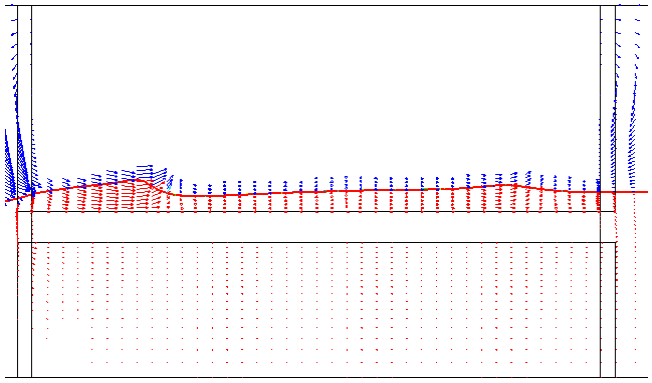

(c) Position III

Figure 4.22: The series of velocity field in the five positions at the same time step

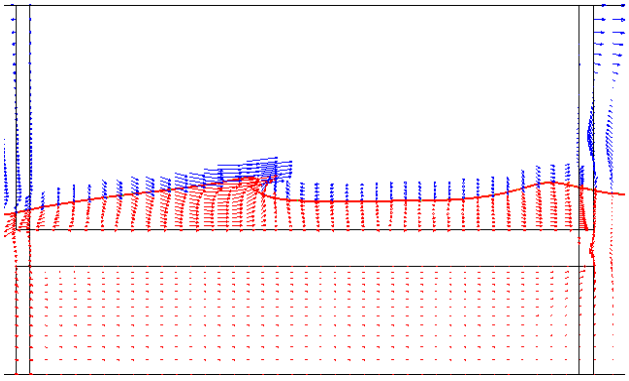

(d) Position IV

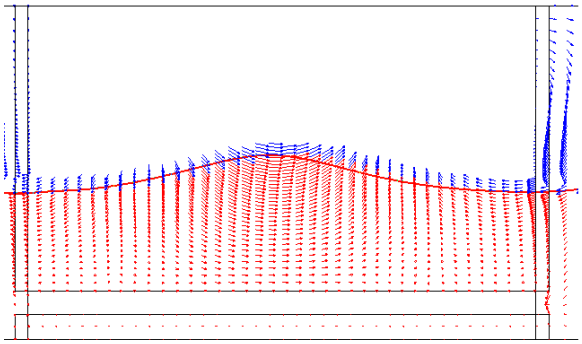

(e) Position V

Figure 4.22: (Continued)

From the figure 4.21 and figure 4.22, we can get the results about dynamic pressure and velocity field in these five positions at the same time step. The comparisons can clearly prove the discussions in each position situation above.

CHAPTER V

CONCLUSIONS

Time-domain simulation of green water around offshore platform was performed using a Reynolds-Averaged Navier-Stokes (RANS) numerical method in conjunction with interface-capturing method based on level set formulation.

In the cases, we can observe the details about the green water by the contribution of Level Set RANS method. The breaking wave phenomena can clearly demonstrate the feasibility and accuracy of level set method to predict violent free surface motion including green water and breaking wave. Furthermore, the high solution numerical method such as WENO scheme can help improve the accuracy of results.

The velocity-extrapolation is crucial to study the breaking wave over the platform by extrapolating the air velocity filed neighboring the free surface. Although this routine just fakes the air velocity filed not based on reality, it can give the good solution in numerical sense. In addition, we can introduce the higher order extrapolation scheme to improve the accuracy in future.

By observing green water, it is straightforward to simulate the green water by using level set method. By the help of this method, wave can be simulated into a variety of transformations, including the anomaly wave shape, the over-tuning wave covering the front surface, the air bubbles trapped in the water. All in all, it can prove that the level set method can make simulation easy to follow shapes with change topology such as when a shape splits in two, develops holes, or the reverse of these operations.

REFERENCES

[1] J.H. Ferziger and M. Peric, *Computational Methods for Fluid Dynamics*, 2nd Edition. Berlin, Germany: Springer-Verlag, 1999.

[2] F.H. Harlow and J.E. Welch, "Numerical study of large-amplitude free surface motions," *Physics of Fluids*, vol. 8, pp. 2182-2189, 1965.

[3] C.W. Hirt and B.D., "Volume of fluid (VOF) method for the dynamics of free boundaries," *Journal of Computational Physics*, vol. 39, pp. 201-225, 1981.

[4] S. Osher and J.A. Sethian, "Fronts propagating with curvature-dependent speed: Algorithms based on Hamilton-Jacobi formulations," *Journal of Computational* Physics, vol. 79, no.1, pp. 12-49, 1988.

[5] H.C. Chen, T. Liu, K.A. Chang, and E.T. Huang, "Time-domain simulation of barge capsizing by a Chimera domain decomposition approach," in *12th International Offshore and Polar Engineering Conference*, vol. III, 2002, pp. 494-501.

[6] H.C. Chen, T. Liu, and E.T. Huang, "Time-domain simulation of large amplitude ship roll motions by a Chimera RANS method," in *Proceedings of the 11th International Offshore and Polar Engineering Conference*, vol. III, 2001, pp. 299-306.

[7] H.C. Chen, and E.T. Huang, "Time-domain simulation of floating pier/ship interaction and harbor resonance," in *Proceedings of the 14th International Offshore and Polar Engineering Conference*, vol. III, 2004, pp. 772-779.

[8] R.K.C. Chan, and R.L. Street, "A computer study of finite-amplitude water waves," *Journal of Computational Physics*, vol. 6, pp. 68-94, 1969.

[9] H. Miyata, "Finite-difference simulation of breaking waves," *Journal of Computational Physics*, vol. 65, pp. 179-214, 1986.

[10] V. Armenio, "An improved MAC method (SIMAC) for unsteady high-Reynolds free surface flows," *International Journal for Numerical Methods in Fluids*, vol. 24, pp. 185-214, 1997.

[11] D.B. Kothe, and W.J. Rider, "Comments on modeling interfacial flows with volume of fluid methods," Los Alamos National Laboratory Reports. 65P05, 76T05. 1995.

[12] R. Scardovelli, and S. Zalesaki, "Direct numerical simulation of free-surface and interfacial flow," *Annual Reviews of Fluid Mechanics*, vol. 31, pp. 567-603, 1999.

[13] C.W. Hirt, and B.D. Nichols, "Volume of fluid (VOF) method for the dynamics of free boundaries," *Journal of Computational Physics*, vol. 39, pp. 201-225, 1981.

[14] M.D. Torrey, "NASA-VOF3D: A three-dimensional computer program for incompressible flows with free surfaces," Los Alamos National Laboratory Reports. NESC9568. 1987.

[15] D.B. Kothe, R.C. Mjolsness, and M.D. Torrey, "RIPPLE: A new model for incompressible flows with free surfaces," *AIAA Journal*, vol. 30, no. 11, pp. 2694-2700, 1998.

[16] C.W. Hirt, and B.D. Nichols, "FLOW-3D users manual," Flow Sciences, Tech. Rep. V9.2. 1988.

[17] B. Biausser, P. Fraunie, S. Grilli, and R. Marcer, "Numerical analysis of the internal kinematics and dynamics of three-dimensional breaking waves on slopes," *International Journal of Offshore and Polar Engineering*, vol. 14, no. 4, 2004.

[18] Chi Yang, and Rainald Lohner, "Computation of 3D flows with violent free surface motion," in *Proceedings of the 15th ISOPE*, vol. 3, pp. 201-220, 2005.

[19] M. Sussman, P. Smereka, and S. Osher, "A level set approach for computing solutions to incompressible two-phase flow," *Journal of Computational Physics*, vol. 114, pp. 146-159, 1994.

[20] J.A. Sethian, and P. Smereka, "Level set methods for fluid interfaces," *Annual Review of Fluid Mechanics*, vol. 35, pp. 120-131, 2003.

[21] S. Osher, and R. Fedkiw, "Level set methods: An overview and some recent results," *Journal of Computational Physics*, vol. 169, pp. 463-502, 2001.

[22] M. Sussman, E. Fatemi, P. Smereka, and S. Osher, "An improved level set method for incompressible two-phase flows," *Computers & Fluids*, vol. 27, pp. 663-680, 1998.

[23] M. Sussman, and E.G. Puckett, "A coupled level set and volume-of-fluid method for computing 3D and Axiymmetric incompressible two-phase flows," *Journal of Computational Physics*, vol. 162, pp. 301-337, 2000.

[24] S.P. Van der pijl, A. Segal, C. Vuik, and P. Wesseling, "A mass-conserving level set method for modeling of multi-phase flows," *International Journal for Numerical Methods in Fluids*, vol. 47, pp. 339-361, 2005.

[25] H. Takahira, T. Horiuchi, and S. Banerjee, "An improved three-dimensional level set method for gas-liquid two-phase flows," *Journal of Fluids Engineeing*, vol. 126, pp. 578-585, 2004.

[26] D. Enright, R. Fedkiw, J. Ferziger, and I. Mitchell, "A hybrid particle level set method for improved interface capturing," *Journal of Computational Physics*, vol. 183, pp. 83-116, 2002.

[27] F. Gibou, R. Fedkiw, R. Cafisch, and S. Osher, "A level set approach for the numerical simulation of dendeitic growth," *Journal of Scientific Computing*, vol. 19, pp. 183-199, 2003.

[28] H. Pitsch, and L. Lageneste, "Large-eddy simulation of premixed turbulent combustion using a level-set approach," in *Proceedings of the Combustion Institute*, vol. 29, 2002, pp. 2001-2008.

[29] J.A. Sethian, and D. Adalsteinsson, "An overview of level set methods for etching, deposition, and lithography development," *IEEE Transaction on Semiconductor Manufacturing*, vol. 10, no. 1, pp. 167-184, 1997.

[30] J.A. Sethian, *Level Set Methods and Fast Marching Methods*. New York: Cambridge Univ. Press, 1996.

[31] H.C. Chen, V.C. Patel, and S. Ju, "Solutions of Reynolds-averaged Naiver-Stokes equations for three-dimensional incompressible flows," *Journal of Computational Physics*, vol. 88, pp. 305-335, 1990.

[32] S. Osher, and R. Fedkiw, *Level Set Methods and Dynamic Implicit Surfaces*. New York: Springer-Verlag, 2003.

[33] C.W. Shu, "Essentially non-oscillatory and weighted essentially non-oscillatory schemes for hyperbolic conservation laws," ICASE Report no. 97-65, NASA/CR-97-206263, 1997.

[34] C.W. Shu, and S. Osher, "Efficient implementation of essentially non-oscillatory shock-capturing schemes," *Journal of Computational Physics*, vol. 77, pp. 439-471, 1988.

[35] C.W. Shu and S. Osher, "Efficient implementation of essentially non-oscillatoryshock-capturing schemes II," *Journal of Computational Physics*, vol. 83, pp. 32-78, 1989.

[36] H.C. Chen, and K. Yu, "CFD simulation wave-current-body interactions including greenwater and wet deck slamming," *Computers & Fluids*, vol. 38, pp. 970-980, 2009.

[37] C.Y. Lin, and C.J. Huang, "Simulation of breaking waves using particle level set method," Ph.D. dissertation, National Cheng Kung University, 2007.

[38] Y. Ryu, K.A. Chang, and R. Mercier, "Application of dam-break flow to green water prediction," *Applied Ocean Research*, vol. 29, pp. 128-136, 2007.

[39] K. Yu, "Level set RANS method for sloshing and green water simulations," Ph.D. dissertation, Texas A&M University, 2007.

VITA

Yucheng Zhao was born in Zhenjiang, Jiangsu, China. He received his B.S. in Naval Architecture and Ocean Engineering from Shanghai Jiao Tong University in 2008. He entered the Ocean Engineering Program, Civil Engineering Department of Texas A&M University in September of 2008 and completed his M.S. in December of 2009.

He can be reached at: HydroLab 203, 3136 TAMU, College Station, TX 77843-3136, U.S.A.